Helsinki University of Technology
Department of Electrical and Telecommunications Engineering

Ilkka Laakso

FDTD METHOD IN ASSESSMENT OF HUMAN EXPOSURE TO BASE STATION RADIATION

Thesis submitted for examination for the degree of Master of Science in Technology

Espoo 4.6.2007

Thesis supervisor:

Prof. Keijo Nikoskinen

Thesis instructor:

D.Sc. (Tech.) Tero Uusitupa

Teknillinen Korkeakoulu

Diplomityon tiivistelmä

Tekijä: Ilkka Laakso

Työn nimi: FDTD-menetelmä tukiasema-antennin säteilylle altistumisen arvioinnissa

Päivämäärä: 4.6.2007 Kieli: Englanti Sivumäärä: 8+92

Osasto: Sähkö- ja tietoliikennetekniikka

Professuuri: Sähkömagnetiikka Koodi: S-96

Valvoja: Prof. Keijo Nikoskinen

Ohjaaja: TkT Tero Uusitupa

FDTD on eksplisiittinen aika-alueen differenssimenetelmä, joka ratkaisee Maxwellin yhtälöt numeerisesti. Tämän diplomityön tarkoituksena on selvittää FDTD-menetelmän soveltamista tukiasema-antennin säteilylle altistumisen arvioimisessa. Radiotaajuuksilla sähkömagneettiselle säteilylle altistumista mitataan niin sanottujen SAR-arvojen (specific absorption rate) kautta, jotka kertovat sähkömagneettisesta häviötehosta kudoksissa ja ovat yhteydessä säteilyn mahdollisiin haitallisiin terveysvaikutuksiin.

Motivaatio tälle tutkimukselle on tukiasema-antenneihin liittyvässä standardoinnissa. Radioaaltoalueen koko kehon tehtävissä FDTD-menetelmä on yleisesti käytetyin menetelmä, ja on tärkeää tietää, kuinka luotettavasti säteilyannoksia saadaan arvioitua, ja mitkä tekijät vaikuttavat tulosten tarkkuuteen.

Työn pääpaino on FDTD SAR-laskennassa tarvittavissa menetelmissä, niiden epävarmuuksissa ja virhetekijöissä. Erityisenä tutkimuskohteena on FDTD:n diskretoinnin resoluution vaikutus SAR-arvoihin. Lisäksi paneudutaan muun muassa materiaalien mallintamiseen FDTD:ssä sekä absorboivien reunaehtojen toimivuuteen SAR-laskennassa. Lopputulosten kannalta on myös tärkeää, miten SAR-arvot on itse asiassa laskettu. Työssä esitelläänkin joitakin vaihtoehtoisia tapoja laskea SAR-arvoja, ja tutkitaan näiden vaikutusta tuloksiin.

Avainsanat: FDTD, SAR, tukiasema-antenni, absorboivat reunaehdot

HELSINKI UNIVERSITY OF TECHNOLOGY

ABSTRACT OF THE MASTER'S THESIS

Author: Ilkka Laakso

Title: FDTD method in assessment of human exposure to base station radiation

Date: 4.6.2007 Language: English Number of pages: 8+92

Department: Electrical and telecommunications engineering

Professorship: Electromagnetics Code: S-96

Supervisor: Prof. Keijo Nikoskinen

Instructor: D.Sc. (Tech.) Tero Uusitupa

FDTD is an explicit finite-difference method that solves the Maxwell's equations numerically in the time domain. The objective of this thesis is to investigate the application of the FDTD method in the assessment of the human exposure to base station radiation. At radio frequencies, the exposure to electromagnetic radiation is given in terms of SAR values (specific absorption rate). SAR describes the power loss inside the tissues, and is linked to the possible adverse health effects of radiation.

The motivation for this study lies in the standardization regarding exposure to base-station antennas. At radio frequencies, FDTD is the most used method in the problems involving full human body models, and it is thus of great importance to study how reliably the SAR values are assessed in FDTD, and which factors affect the accuracy of the results.

The emphasis of this thesis is on the methods which are needed in the FDTD-SAR calculations and their uncertainties. How the resolution of the FDTD discretization affects the SAR values is of particular interest. Among other things, material modeling in FDTD and the applicability of absorbing boundary conditions in SAR calculations are studied in detail. Naturally, the final results are affected by how the SAR values actually are calculated. Several different methods for SAR calculation are presented in this work, and their effects on the results are studied.

Keywords: FDTD, specific absorption rate, base station antenna, absorbing boundary conditions

Preface

This thesis was carried out in the Electromagnetics laboratory at the Helsinki University of Technology, during August 2006–May 2007.

I would like to thank D.Sc. Tero Uusitupa, my instructor, and M.Sc. Sami Ilvonen for their support, guidance and constructive comments. I also wish to express my gratitude to my supervisor, Professor Keijo Nikoskinen, for his support and advice.

Financial support received from TEKES (National Technology Agency of Finland) and Nokia Corporation through the EMSOFT project is acknowledged.

Otaniemi, 4.6.2007

Ilkka Laakso

Contents

Symbols and notational conventions

List of symbols

Electromagnetics

$\mathcal{D}$	the domain of the electromagnetic fields, $\mathcal{D} \subset \mathbb{R}^3$
$\mathbf{B}$	Magnetic flux density [Vs/m^2]
$\mathbf{D}$	Electric flux density [As/m^2]
$\mathbf{E}$	Electric field strength vector [V/m]
$\mathbf{H}$	Magnetic field strength vector [A/m]
$\mathbf{J}$	Current density [A/m^2]
$\mathbf{J}_m$	Magnetic current density [V/m^2]
c_0	Speed of light in vacuum ($\approx 2.9979 \cdot 10^8$ m/s)
f	Frequency [Hz]
s	Power loss density [W/m^3]
S	Power density [W/m^2] (Poynting vector amplitude)
ϵ	Permittivity [As/Vm]
ϵ_r	Relative permittivity
ϵ_0	Permittivity in vacuum ($\approx 8.8542 \cdot 10^{-12}$ As/Vm)
μ	Permeability [Vs/Am]
μ_r	Relative permeability
μ_0	Permeability in vacuum ($= 4\pi \cdot 10^{-7}$ Vs/Am)
ω	(Angular) frequency ($= 2\pi f$) [rad/s]
ρ	Density [kg/m^3]
σ	Electric conductivity [S/m]
σ_m	Magnetic conductivity [Ω/m]

FDTD

$\mathcal{I}$	the index set, $\mathbf{r}(\mathcal{I}) \approx \mathcal{D}$
(i, j, k)	x, y and z indices
$\mathbf{p}$	$\mathbf{p} = (i, j, k) \in \mathcal{I}$, the index vector in the FDTD lattice
$\mathbf{r}(\mathbf{p})$	$\mathbf{r}(\mathbf{p}) = (x(i), y(j), z(k)) \in \mathcal{D}$, the discretized location vector
Δu	Cell width in u direction
Δ	Cell width in a cubical grid ($\Delta \equiv \Delta x \equiv \Delta y \equiv \Delta z$)
n	Time step index
Δt	Time step
$X^n(\cdot)$	$X(\cdot, t = n\Delta t)$, where X is any quantity
$X(\mathbf{p})$	Short for $X(\mathbf{r}(\mathbf{p}))$, where X is any quantity (with domain $\mathcal{D}$)
K_x, K_y, K_z	Sizes of the FDTD lattice in x, y and z directions, respectively

Other symbols and notation

$\mathbf{r}$	$\mathbf{r} = (x, y, z) \in \mathcal{D}$, the location vector
$\mathbf{u}_v$	unit vector in v direction
j	imaginary unit
$\mathcal{F}$	Fourier transform
$\mathcal{F}^{-1}$	inverse Fourier transform
$\cdot * \cdot$	convolution
$\emptyset$	empty set
$\cup$	union
$\cap$	intersection
$\setminus$	set difference
$\#$	number of elements (in a set)
$\times$	Cartesian product (of sets), or cross product (of vectors)
$\lvert \cdot \rvert$	absolute value (scalars) or Euclidian norm (vectors)

Abbreviations

ABC	Absorbing Boundary Condition
BSA	Base station antenna
CFS	Complex-frequency shifted (tensor)
CPML	Convolutional PML
FDTD	Finite-difference time-domain (method)
PEC	Perfect Electric Conductor
PML	Perfectly Matched Layer
rms	root-mean square
SAR	Specific Absorption Rate
UPML	Uniaxial PML or Unsplit PML

1 Introduction

Finite-difference time-domain (FDTD) method is the most popular method for the numerical assessment of human exposure to base station radiation. The exposure to such radio-frequency fields is measured in terms of specific absorption rate (SAR), which is a unit of electromagnetic power loss in tissues. The main objective of this thesis is to investigate and analyze the methods which are needed in FDTD SAR calculations.

This thesis begins with a detailed description of the FDTD method, starting from the very derivation of the finite-difference update equations. A particular focus will be on the modeling of dielectric materials, such as body tissues. Convolutional perfectly matched layer (CPML) absorbing boundary conditions are thoroughly examined, and their performance in SAR calculations is verified.

Modeling human anatomies and base station antennas is described at a general level. Several aspects of antenna modeling in FDTD will be presented, but we will not go into details of modeling specific antennas. Some available human body models are presented and their properties are discussed, but constructing human body models is out of the scope of this work.

A purely electromagnetic perspective is assumed in the exposure analysis. Namely, we are assessing the exposure only in terms of electromagnetic power loss. Whether or not this causes too much heating of tissues, or consequently, adverse health effects, is not in the scope of this thesis. The focus is on the SAR calculation methods. However, some information on the exposure standards and recommendations by international organizations, i.e. the restrictions on SAR to prevent adverse health effects, is presented.

A large number of numerical results is included, most of which will be more or less simplified tests. The objective of the presented results is to illustrate the accuracy and uncertainties of the methods used in FDTD SAR calculation. Finally, some results involving a human body model near a base station antenna are presented.

The structure of this thesis is the following. Sections 2–5 describe the theory of the methods which are needed in the FDTD assessment of exposure to base station radiation. A large number of numerical results, which illustrate the presented methods, is contained in Section 6. Discussion of the results is found in Section 7, and finally, the conclusions are in Section 8.

2 Finite-difference time-domain method

The finite-difference time-domain method (FDTD) is a numerical technique for solving electromagnetic problems. The space is divided into small, rectangular voxels (cells) in which the time-domain fields are solved using an explicit finite-difference update scheme. Explicity means that no linear algebra is needed, which allows electrically large problems.

FDTD is proven to be suitable for a wide range of applications, some examples of which can be found in [1]. Modeling various kinds of heterogenous dielectric materials or antenna structures is not a problem in FDTD. Consequently, FDTD is the method of choice in the assessment of human exposure to radio frequency electromagnetic fields of a base station antenna.

2.1 Yee algorithm

The foundation of the FDTD method is the Yee algorithm, which is a finite-difference update scheme for the electromagnetic fields, named after K. Yee who first introduced it in 1966 [2].

Assume a rectangular volume $\mathcal{D}$, surrounded by PEC, and filled with isotropic material. $\mathcal{D}$ does not include any sources.

$$\mathcal{D} = \{(x, y, z) : x \in [x_{\min}, x_{\max}],\ y \in [y_{\min}, y_{\max}],\ z \in [z_{\min}, z_{\max}]\} \tag{1}$$

The Maxwell's equations in $\mathcal{D}$ are

$$\frac{\partial}{\partial t}\mathbf{B} = -\mathbf{J}_m - \nabla \times \mathbf{E} \tag{2}$$

$$\frac{\partial}{\partial t}\mathbf{D} = -\mathbf{J} + \nabla \times \mathbf{H}. \tag{3}$$

If the material is nondispersive, i.e. material parameters are independent of the frequency[1], the equations can be written in the form

$$\frac{\partial}{\partial t}\mathbf{H} = -\frac{\sigma_m}{\mu}\mathbf{H} - \frac{1}{\mu}\nabla \times \mathbf{E} \tag{4}$$

$$\frac{\partial}{\partial t}\mathbf{E} = -\frac{\sigma}{\epsilon}\mathbf{E} + \frac{1}{\epsilon}\nabla \times \mathbf{H}. \tag{5}$$

Write a central difference approximation (second order) for the time derivate in (5) at $t = t_{n+1/2} = (n + 1/2)\Delta t$:

$$\frac{\mathbf{E}^{n+1} - \mathbf{E}^n}{\Delta t} \approx -\frac{\sigma}{\epsilon}\mathbf{E}^{n+1/2} + \frac{1}{\epsilon}\nabla \times \mathbf{H}^{n+1/2}. \tag{6}$$

On the right side

$$\mathbf{E}^{n+1/2} \approx \frac{\mathbf{E}^{n+1} + \mathbf{E}^n}{2}. \tag{7}$$

[1] This assumption is not realistic, because the material parameters of the human tissues are in fact frequency dependent. However, this assumption is justified in Section 2.3.2.

Inserting (7) into (6) and rearranging terms yields

$$\mathbf{E}^{n+1} \approx \frac{2\epsilon - \sigma\Delta t}{2\epsilon + \sigma\Delta t}\mathbf{E}^n + \frac{2\Delta t}{2\epsilon + \sigma\Delta t}\nabla \times \mathbf{H}^{n+1/2}. \tag{8}$$

Denoting

$$C_a = \frac{2\epsilon - \sigma\Delta t}{2\epsilon + \sigma\Delta t} \quad \text{and} \quad C_b = \frac{2\Delta t}{2\epsilon + \sigma\Delta t}, \tag{9}$$

equation (8) becomes

$$\mathbf{E}^{n+1} \approx C_a\mathbf{E}^n + C_b\nabla \times \mathbf{H}^{n+1/2}. \tag{10}$$

Similarly, for the magnetic field, starting from (4) and writing a central difference approximation at $t = t_n = n\Delta t$, we get:

$$\mathbf{H}^{n+1/2} \approx D_a\mathbf{H}^{n-1/2} - D_b\nabla \times \mathbf{E}^n, \tag{11}$$

where

$$D_a = \frac{2\mu - \sigma_m\Delta t}{2\mu + \sigma_m\Delta t} \quad \text{and} \quad D_b = \frac{2\Delta t}{2\mu + \sigma_m\Delta t}. \tag{12}$$

Equations (10) and (11) are the update equations for the electric and magnetic fields in a continuous space and sampled time. The next step is to apply spatial discretization into the equations.

Divide $[x_{\min}, x_{\max}]$, $[y_{\min}, y_{\max}]$ and $[z_{\min}, z_{\max}]$ into K_x, K_y and K_z parts, respectively, and denote

$$\begin{aligned} x_{\min} = x(0) < x(1) < \ldots < x(K_x - 1) < x(K_x) = x_{\max} \\ y_{\min} = y(0) < y(1) < \ldots < y(K_y - 1) < y(K_y) = y_{\max} \\ z_{\min} = z(0) < z(1) < \ldots < z(K_z - 1) < z(K_z) = z_{\max}. \end{aligned} \tag{13}$$

As a result, $\mathcal{D}$ is divided into $K_xK_yK_z$ rectangles (cells). Define the "half-indices", which mark the center points of the cells, by

$$u(l - \frac{1}{2}) = \frac{u(l-1) + u(l)}{2}, \quad l \in \{1, 2, \ldots, K_u\}, \quad u \in \{x, y, z\}. \tag{14}$$

The cell widths Δx, Δy and Δz are defined

$$\Delta u(l) = u(l + \frac{1}{2}) - u(l - \frac{1}{2}), \quad l \in \{\frac{1}{2}, 1, \ldots, K_u - 1, K_u - \frac{1}{2}\}, \quad u \in \{x, y, z\}. \tag{15}$$

The spatial locations of the discretized field components are chosen in a divergence-free nature, as shown in Figure 1. This choice of the positions of the field components is the main insight of [2]. Every electric field component is surrounded by circulating magnetic field components and vice versa, and no two field components are positioned in the same grid point. Denote the set of indices in which the discretized fields are defined by $\mathcal{I}_{E_x}$ for E_x, $\mathcal{I}_{E_y}$ for E_y and so on. The index sets then become:

$$\begin{aligned} \mathcal{I}_{E_x} &= \left\{(i - \tfrac{1}{2}, j, k) : i = 1, \ldots, K_x;\ j = 0, \ldots, K_y;\ k = 0, \ldots, K_z\right\} \\ \mathcal{I}_{E_y} &= \left\{(i, j - \tfrac{1}{2}, k) : i = 0, \ldots, K_x;\ j = 1, \ldots, K_y;\ k = 0, \ldots, K_z\right\} \\ \mathcal{I}_{E_z} &= \left\{(i, j, k - \tfrac{1}{2}) : i = 0, \ldots, K_x;\ j = 0, \ldots, K_y;\ k = 1, \ldots, K_z\right\} \\ \mathcal{I}_{H_x} &= \left\{(i, j - \tfrac{1}{2}, k - \tfrac{1}{2}) : i = 0, \ldots, K_x;\ j = 1, \ldots, K_y;\ k = 1, \ldots, K_z\right\} \\ \mathcal{I}_{H_y} &= \left\{(i - \tfrac{1}{2}, j, k - \tfrac{1}{2}) : i = 1, \ldots, K_x;\ j = 0, \ldots, K_y;\ k = 1, \ldots, K_z\right\} \\ \mathcal{I}_{H_z} &= \left\{(i - \tfrac{1}{2}, j - \tfrac{1}{2}, k) : i = 1, \ldots, K_x;\ j = 1, \ldots, K_y;\ k = 0, \ldots, K_z\right\} \end{aligned} \tag{16}$$

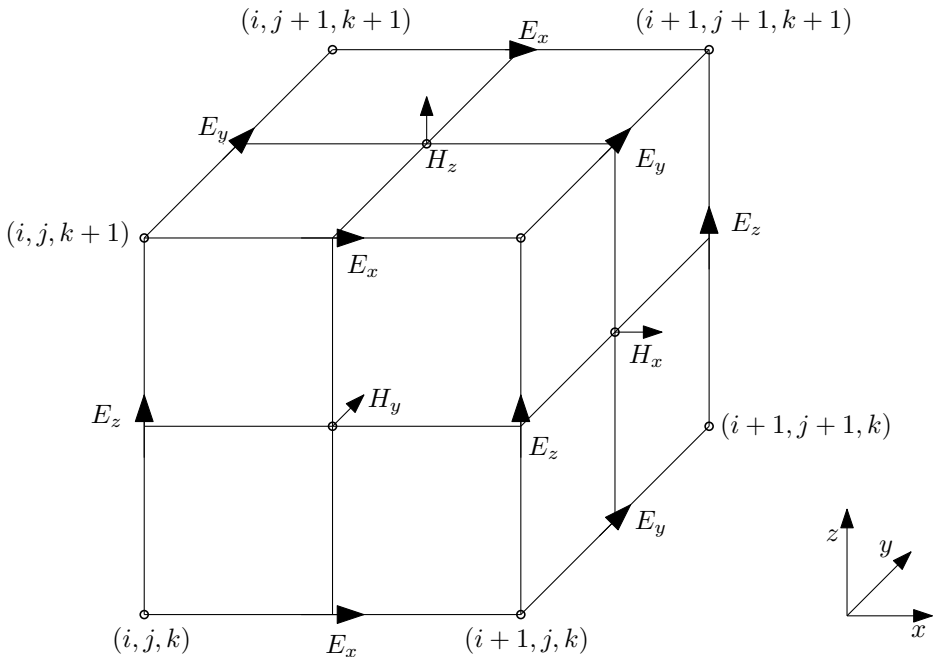

Figure 1: The locations of the field components in a single cell (Yee cell).

Here the indices $\mathbf{p} = (i, j, k)$ correspond to points $\mathbf{r}(\mathbf{p}) = (x(i), y(j), z(k)) \in \mathcal{D}$, where $x(i)$, $y(j)$ and $z(k)$ are defined in (13). Notice that the index sets are disjoint

$$\mathcal{I}_X \cap \mathcal{I}_Y = \begin{cases} \emptyset, & X \neq Y \\ \mathcal{I}_X, & X = Y \end{cases} \quad X, Y \in \{E_x, E_y, E_z, H_x, H_y, H_z\}.$$

We denote

$$\mathcal{I} = \left\{ (i, j, k) : i = 0, \frac{1}{2}, \ldots, K_x;\ j = 0, \frac{1}{2}, \ldots, K_y;\ k = 0, \frac{1}{2}, \ldots, K_z \right\}, \tag{17}$$

which is the set of all possible indices, including the half-indices.

Define

$$\mathcal{I}_0 = \{(i, j, k) \in \mathcal{I} : i \in \{0, K_x\} \vee j \in \{0, K_y\} \vee k \in \{0, K_z\}\}, \tag{18}$$

which means the set of indices which are located on the outer PEC boundaries.

Next, we will discretize the curl operator, which can be rewritten as

$$\nabla\times = \begin{bmatrix} 0 & -\frac{\partial}{\partial z} & \frac{\partial}{\partial y} \\ \frac{\partial}{\partial z} & 0 & -\frac{\partial}{\partial x} \\ -\frac{\partial}{\partial y} & \frac{\partial}{\partial x} & 0 \end{bmatrix}. \tag{19}$$

The spatial derivates in (19) are replaced with their central-difference approximations

$$\frac{\partial}{\partial x} F(i, j, k) \approx \frac{F(i + \frac{1}{2}, j, k) - F(i - \frac{1}{2}, j, k)}{\Delta x(i)} \tag{20}$$

$$\frac{\partial}{\partial y}F(i,j,k) \approx \frac{F(i,j+\frac{1}{2},k) - F(i,j-\frac{1}{2},k)}{\Delta y(j)} \tag{21}$$

$$\frac{\partial}{\partial z}F(i,j,k) \approx \frac{F(i,j,k+\frac{1}{2}) - F(i,j,k-\frac{1}{2})}{\Delta z(k)}. \tag{22}$$

If the grid is uniform ($\Delta x, \Delta y$ and Δz are constant), these approximations are second-order ($O(\Delta^2)$) accurate. With nonuniform grid, they are only first-order accurate at some indices (see next section). Denote the resulting discrete curl-operator by $\nabla\otimes$.

Equation (10) becomes

$$\begin{bmatrix} \tilde{E}_x^{n+1}(\mathbf{p}_x) \\ \tilde{E}_y^{n+1}(\mathbf{p}_y) \\ \tilde{E}_z^{n+1}(\mathbf{p}_z) \end{bmatrix} = \begin{bmatrix} C_a(\mathbf{p}_x)\tilde{E}_x^{n}(\mathbf{p}_x) \\ C_a(\mathbf{p}_y)\tilde{E}_y^{n}(\mathbf{p}_y) \\ C_a(\mathbf{p}_z)\tilde{E}_z^{n}(\mathbf{p}_z) \end{bmatrix} + \begin{bmatrix} C_b(\mathbf{p}_x) & 0 & 0 \\ 0 & C_b(\mathbf{p}_y) & 0 \\ 0 & 0 & C_b(\mathbf{p}_z) \end{bmatrix} \nabla\otimes \begin{bmatrix} \tilde{H}_x^{n+1/2}(\mathbf{p}_x) \\ \tilde{H}_y^{n+1/2}(\mathbf{p}_y) \\ \tilde{H}_z^{n+1/2}(\mathbf{p}_z) \end{bmatrix}, \tag{23}$$

where $\mathbf{p}_x \in \mathcal{I}_{E_x}\backslash\mathcal{I}_0$, $\mathbf{p}_y \in \mathcal{I}_{E_y}\backslash\mathcal{I}_0$ and $\mathbf{p}_z \in \mathcal{I}_{E_z}\backslash\mathcal{I}_0$. For brevity, we have denoted $C_a(\mathbf{p}) = C_a(\mathbf{r}(\mathbf{p}))$ and $C_b(\mathbf{p}) = C_b(\mathbf{r}(\mathbf{p}))$.

Equation (11) becomes

$$\begin{bmatrix} \tilde{H}_x^{n+\frac{1}{2}}(\mathbf{p}_x) \\ \tilde{H}_y^{n+\frac{1}{2}}(\mathbf{p}_y) \\ \tilde{H}_z^{n+\frac{1}{2}}(\mathbf{p}_z) \end{bmatrix} = \begin{bmatrix} D_a(\mathbf{p}_x)\tilde{H}_x^{n-\frac{1}{2}}(\mathbf{p}_x) \\ D_a(\mathbf{p}_y)\tilde{H}_y^{n-\frac{1}{2}}(\mathbf{p}_y) \\ D_a(\mathbf{p}_z)\tilde{H}_z^{n-\frac{1}{2}}(\mathbf{p}_z) \end{bmatrix} - \begin{bmatrix} D_b(\mathbf{p}_x) & 0 & 0 \\ 0 & D_b(\mathbf{p}_y) & 0 \\ 0 & 0 & D_b(\mathbf{p}_z) \end{bmatrix} \nabla\otimes \begin{bmatrix} \tilde{E}_x^{n}(\mathbf{p}_x) \\ \tilde{E}_y^{n}(\mathbf{p}_y) \\ \tilde{E}_z^{n}(\mathbf{p}_z) \end{bmatrix}, \tag{24}$$

where $\mathbf{p}_x \in \mathcal{I}_{H_x}\backslash\mathcal{I}_0$, $\mathbf{p}_y \in \mathcal{I}_{H_y}\backslash\mathcal{I}_0$ and $\mathbf{p}_z \in \mathcal{I}_{H_z}\backslash\mathcal{I}_0$. Again, we have used the shorter notation $D_a(\mathbf{p}) = D_a(\mathbf{r}(\mathbf{p}))$ and $D_b(\mathbf{p}) = D_b(\mathbf{r}(\mathbf{p}))$. Notice that the fields are not updated in $\mathcal{I}_0$, where the fields are zeros.

In the equations, we have not taken into account the possibility of dielectric or magnetic material boundaries. The field components and material parameters at such boundaries need to be given a special treatment, which is described in Section 2.3.3.

Equations (23) and (24) are the update equations for the Yee's algorithm in an isotropic medium. In the equations, we denoted the discretized fields with tildes. In what is to follow, it should be clear from the context whether we mean the accurate fields (solutions of (4), (5)) or the discretized fields, so the tildes are left out. Additionally, we will implicitly assume the notation $X(\mathbf{p}) = X(\mathbf{r}(\mathbf{p}))$ for any nondiscretized quantity $X : \mathcal{D} \to \mathbb{R}$.

The algorithm can be summarized as follows. The E_x component is used as an example, and other field components are treated similarly. The accurate field

$$E_x : \mathcal{D} \times \mathbb{R}^+ \to \mathbb{R},$$

which is the solution for the Maxwell's equations (4) and (5), is approximated by the discretized field

$$\tilde{E}_x : \mathcal{I}_{E_x} \times \{0, 1, \ldots\} \to \mathbb{F}, \tag{25}$$

such that

$$E_x(\mathbf{r}(\mathbf{p}); t_n) \approx \tilde{E}_x^n(\mathbf{p}), \quad \mathbf{p} \in \mathcal{I}_{E_x},$$

where $\tilde{E}_x^n(\mathbf{p})$ is calculated at each time step using (23) and (24). In (25), $\mathbb{F}$ denotes the floating-point numbers. In this work, 4-byte floating-point numbers are used in the numerical calculations. However, in the following theory sections, exact arithmetic is assumed.

If the material is nonpermeable ($\mu_r \equiv 1$, $\sigma_m \equiv 0$), as is usually assumed in human exposure calculations, equation (24) is simplified. In such a case, the coefficients D_a and D_b are constants (specially: $D_a \equiv 1$). From now on, that is assumed in this work.

2.2 Accuracy and stability

In the case of nonuniform grid, the spatial-difference approximations (20)–(22) are locally only first-order accurate at "full" indices (that means the spatial derivates of the magnetic field). E.g. substituting definitions (14) and (15) into (20), when $i \in \{1, 2, \ldots, K_x - 1\}$, gives

$$\frac{F(i+\frac{1}{2}) - F(i-\frac{1}{2})}{\Delta x(i)} = \frac{F(i+1) - F(i-1)}{\Delta x(i+\frac{1}{2}) + \Delta x(i-\frac{1}{2})} = \frac{\partial}{\partial x} F(i) + O(\Delta x(i+\frac{1}{2}) - \Delta x(i-\frac{1}{2})).$$

If $i \in \{\frac{1}{2}, \frac{3}{2}, \ldots, K_x - \frac{1}{2}\}$, this approximation would be second order. However, as proven in [3], the global accuracy is still second order, regardless of the first-order local accuracy (Yee's algorithm is *supra-convergent*). Thus, when the quotient $\Delta t/h$, where $h = \max(\Delta)$ is the greatest spatial step, is kept constant, the discretization error (in a discrete L_2-norm) behaves as:

$$\text{error} \leq C(t_n + 1)h^2, \tag{26}$$

where C is some constant and $t_n = n\Delta t$.

A common rule of thumb for the mesh resolution is the "$\lambda/10$ rule": cell size should not be larger than one tenth of the wavelength. The wavelength is shorter inside dielectric materials, so consequently, the mesh should be finer there.

Yee's algorithm is an explicit finite-difference method, and its stability is conditional. A necessary condition for the stability is that the time step Δt must satisfy the Courant-Friedrichs-Lewy (CFL) condition

$$\Delta t \leq \frac{1}{c_0 \sqrt{\frac{1}{\min(\Delta x^2)} + \frac{1}{\min(\Delta y^2)} + \frac{1}{\min(\Delta z^2)}}} = \text{CFL}. \tag{27}$$

Essentially, equation (27) means that the domain of dependence of the discretized problem must include the domain of dependence of the continuous problem.

Usually, the time step Δt is chosen to be some quotient of the CFL condition. E.g. in this work, unless otherwise stated, the time step will be

$$\Delta t = 0.99 \text{ CFL}.$$

2.3 Materials in FDTD

In Yee algorithm, the space is essentially divided into a finite number of rectangles. It is obvious that modeling curved structures cannot be done accurately using the standard algorithm. The simplest approximation, the staircase approximation, just discretizes material objects so that they fit into the FDTD lattice.

There are numerous methods presented in the literature to improve the approximation of curved boundaries. In this work, however, only the staircase approximation will be focused on. This is mainly the case because most human voxel models for FDTD SAR calculations are staircase models.

2.3.1 PEC and PMC

Structures consisting of perfect electric or magnetic conductors can be easily modeled in FDTD. For example, if we want to model a PEC structure, such as an antenna, find indices $\mathcal{I}_{\text{PEC}} \subset \mathcal{I}$ (17) which belong to tangential electric or normal magnetic fields on the PEC boundaries. Then add these indices into $\mathcal{I}_0$ (18).

After updating the fields with (23) and (24), the field components the indices of which are in $\mathcal{I}_{\text{PEC}}$ will be set to zeros. Alternatively, one could set $\sigma = \infty$ inside the PEC structures as described in Section 2.3.3, but this approach does not allow thin sheets or wires.

2.3.2 Frequency-dependent materials

It was assumed in the derivation of the FDTD update equations that the material parameters were independent of the frequency. Unfortunately, this assumption does not hold with the material parameters of human tissues, which are frequency dependent (see Section 2.3.6).

In this section, we will briefly describe how dispersive materials could be included in FDTD simulations. It will also be shown that modeling the dispersion is not usually needed. A time dependence $e^{j\omega t}$ is assumed in the following.

For linear-dispersive media, the (complex) permittivity ($\hat{\epsilon}$) can be written in the frequency domain as

$$\hat{\epsilon} = \hat{\epsilon}(\omega) = \epsilon_0(\epsilon_\infty + \chi_e(\omega)) = \epsilon'(\omega) - j\epsilon''(\omega), \tag{28}$$

where χ_e is the (complex-valued) electric susceptibility function, and ϵ_∞ is the permittivity when $\omega \to \infty$.

The electric flux in the frequency domain is thus

$$\mathbf{D}(\omega) = \epsilon_0(\epsilon_\infty + \chi_e(\omega))\mathbf{E}(\omega). \tag{29}$$

In time domain this becomes

$$\mathbf{D}(t) = \epsilon_0[\epsilon_\infty \mathbf{E}(t) + (\chi_e * \mathbf{E})(t)], \tag{30}$$

where $*$ denotes convolution.

The special case of nondispersive materials, as assumed in Section 2.1, is

$$\epsilon_\infty = \epsilon_r$$

$$\chi_e(\omega) = \frac{\sigma}{j\omega\epsilon_0}.$$

In this case, the calculation of the convolution is avoided, as $1/j\omega$ means integration in the time domain.

Including the convolution in (30) in the FDTD update equations can be done using the recursive-convolution (RC) technique (see e.g. [1]). Section 3.5 contains an example of the usage of the RC technique (for absorbing boundary conditions).

Basically, using the RC method would result in inserting recursive accumulator terms $\{\Psi_u E^n\}$ into each of the update equations (23). Each of these terms would have their own update equations which would depend on the dispersion models of the materials. This would essentially double the memory requirements of storing the electric fields $\{E_u\}$, as each component would require their own $\{\Psi_u E^n\}$, respectively.

Fortunately, the above approach is not needed if we are only interested in the fields at a certain fixed frequency ω_0. If the materials are assumed to be linear[2], the solutions of the Maxwell's equations at the fixed frequency ω_0 do not depend on the solutions of the other frequencies.

Setting the material parameters to nondispersive

$$\epsilon \equiv \epsilon'(\omega_0) = \mathrm{Re}\{\hat{\epsilon}(\omega_0)\}, \tag{31}$$

and

$$\sigma \equiv \omega_0\epsilon''(\omega_0) = -\omega_0\mathrm{Im}\{\hat{\epsilon}(\omega_0)\}, \tag{32}$$

will give the correct solution at $\omega = \omega_0$. The solutions at other frequencies will most likely be incorrect. Thus, unless the time dependence of the fields is strictly sinusoidal (frequency ω_0), the time-domain fields will also be unrealistic.

This somewhat justifies the initial assumption of nondispersive materials. Namely, the solutions at fixed frequencies are the main interest in this work.

2.3.3 Modeling material objects

One of the most important features of FDTD is the ease with which heterogeneous dielectric and/or conducting objects can be included in calculations. Basically, there are two ways how dielectric materials can be included: the material may be positioned either in E cells (an example of an E cell is shown in Figure 1) or in H cells. The cells are indexed by their center points, resulting in index sets

$$\mathcal{I}_E = \left\{(i-\frac{1}{2}, j-\frac{1}{2}, k-\frac{1}{2}) : i = 1,\ldots,K_x;\ j = 1,\ldots,K_y;\ k = 1,\ldots,K_z\right\} \tag{33}$$

[2]Permittivity and conductivity do not depend on the field strengths. This assumption does not necessarily hold in reality.

for the E cells, and

$$\mathcal{I}_H = \{(i,j,k) : i = 0,\ldots,K_x;\ j = 0,\ldots,K_y;\ k = 0,\ldots,K_z\} \tag{34}$$

for the H cells.

Each cell $\mathbf{p} \in \mathcal{I}_E$ or $\mathbf{p} \in \mathcal{I}_H$ is given material parameters $\epsilon(\mathbf{p})$ and $\sigma(\mathbf{p})$. The material parameters are assumed to be constant inside a single cell.

When using the E cells, the electric field (E) components are located on the cell edges, and are thus tangential to material boundaries. When the H cells are used, the magnetic field (H) components are positioned on the cell edges, which results in the electric field components being located on the cell faces, normal to material boundaries. On the boundaries of dissimilar materials, effective material parameters need to be used when calculating the coefficients (9). Also, the field components on the boundaries must be interpreted differently.

In the following, the fields are assumed complex and time harmonic as in Section 2.3.2. Similarly to that section, the complex permittivities (28) are denoted with hats ($\hat{\epsilon}$), and the nondispersive permittivity (31) and conductivity (32) are denoted without hats.

The boundary conditions for the electric field and the electric flux density on material boundaries are

$$\mathbf{n} \times \mathbf{E}_1 = \mathbf{n} \times \mathbf{E}_2 \tag{35}$$

$$\mathbf{n} \cdot \mathbf{D}_1 = \mathbf{n} \cdot \mathbf{D}_2 \tag{36}$$

where $\mathbf{n}$ is the normal vector of the boundary. These conditions result in electric flux density tangential component being discontinuous on a boundary. And similarly, electric field normal component is discontinuous.

The electric field tangential component and the electric flux density normal component are well defined in a physical sense. The other components, i.e. the electric field normal component or the electric flux density tangential component, are "effective" in nature. On a boundary, they are defined as a linear average of the (physical) fields on the two sides of the boundary.

The effective material parameter $\hat{\epsilon}_{\text{eff}}$ is defined

$$\mathbf{D} = \hat{\epsilon}_{\text{eff}}\mathbf{E}, \quad \text{in } \mathcal{I}_{E_x} \cup \mathcal{I}_{E_y} \cup \mathcal{I}_{E_z}, \tag{37}$$

such that it links the effective and the physical field.

The effective parameters at an arbitrary location $\mathbf{p} \in (\mathcal{I}_{E_x} \cup \mathcal{I}_{E_y} \cup \mathcal{I}_{E_z})$ can be defined as follows.

Figure 2 shows the location of an electric field component when the materials are positioned in E cells. The electric field is tangential to the material boundaries. Thus the electric field is the actual physical field, and the electric flux density is an effective field.

In the figure, the (complex) permittivities of the four cells are $\hat{\epsilon}_1$, $\hat{\epsilon}_2$, $\hat{\epsilon}_3$, and $\hat{\epsilon}_4$. The electric field E is tangential to the interface of the materials, and by continuity, it is the same in all four cells. The physical electric flux density tangential component

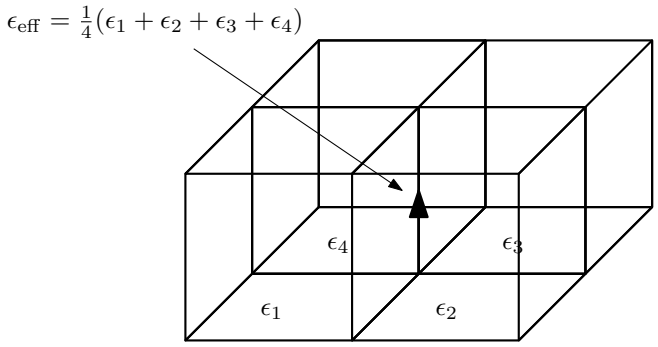

Figure 2: The location of an electric field component and the effective permittivity in the E-cell case.

D_l in each cell l is then $D_l = \hat{\epsilon}_l E$, and the effective electric flux D at the marked edge is the average of these. The effective permittivity at the edge can be calculated

$$\hat{\epsilon}_{\text{eff}} E = D = \frac{1}{4}\left(D_1 + D_2 + D_3 + D_4\right) = \frac{1}{4}\left(\hat{\epsilon}_1 E + \hat{\epsilon}_2 E + \hat{\epsilon}_3 E + \hat{\epsilon}_4 E\right)$$

$$\Rightarrow \hat{\epsilon}_{\text{eff}} = \frac{1}{4}\left(\hat{\epsilon}_1 + \hat{\epsilon}_2 + \hat{\epsilon}_3 + \hat{\epsilon}_4\right). \tag{38}$$

In the case of nondispersive media as in (31), (32), the material parameters on the edge are thus

$$\epsilon_{\text{eff}} = \frac{1}{4}\left(\epsilon_1 + \epsilon_2 + \epsilon_3 + \epsilon_4\right)$$

and

$$\sigma_{\text{eff}} = \frac{1}{4}\left(\sigma_1 + \sigma_2 + \sigma_3 + \sigma_4\right),$$

where $\{\epsilon_u\}$ and $\{\sigma_u\}$ are the respective nondispersive material parameters of the four cells.

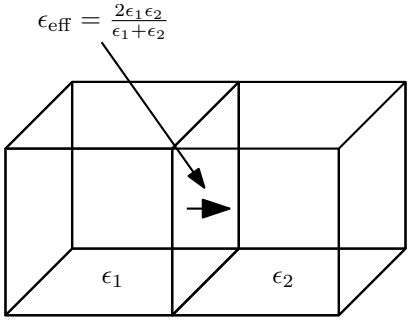

Figure 3: The location of an electric field component and the effective permittivity in the H-cell case.

The situation in which the materials are in H cells is illustrated in Figure 3. The electric field component is normal, so the electric flux density is the actual physical field, and the electric field is an effective field.

The effective electric field E on the side is the linear average of the physical electric fields E_1 and E_2 of the two neighboring cells. By continuity, the electric flux density normal component D is the same in both cells, so $\hat{\epsilon}_1 E_1 = \hat{\epsilon}_2 E_2 = D$. The effective permittivity can then be calculated

$$D = \hat{\epsilon}_{\text{eff}} E = \hat{\epsilon}_{\text{eff}} \frac{1}{2}(E_1 + E_2) = \hat{\epsilon}_{\text{eff}} \frac{1}{2}\left(\frac{D}{\hat{\epsilon}_1} + \frac{D}{\hat{\epsilon}_2}\right)$$

$$\Rightarrow \hat{\epsilon}_{\text{eff}} = \frac{2\hat{\epsilon}_1 \hat{\epsilon}_2}{\hat{\epsilon}_1 + \hat{\epsilon}_2}. \tag{39}$$

The case of nondispersive media, as in (31), (32), is a little more complicated than in the E-cell case. Generally, the effective permittivity on the boundary will become dispersive, even if the two materials are nondispersive. The nondispersive material parameters are thus

$$\epsilon_{\text{eff}} = \text{Re}\{\hat{\epsilon}_{\text{eff}}\} \approx \frac{2\epsilon_1 \epsilon_2}{\epsilon_1 + \epsilon_2},$$

and

$$\sigma_{\text{eff}} = -\omega_0 \text{Im}\{\hat{\epsilon}_{\text{eff}}\} \approx \frac{2\sigma_1 \sigma_2}{\sigma_1 + \sigma_2}.$$

The approximations usually seem to give values very close to the accurate values, and they are used in this work instead of the accurate values.

In the H-cell case, the electric field of the FDTD algorithm is an effective field. Postprocessing the results, such as calculating power loss, requires the physical electric field, which can be calculated as follows (in both time and frequency domain). Assume we know the (effective) electric field normal component $\mathbf{E} = \epsilon_{\text{eff}}^{-1}\mathbf{D}$ on the side in Figure 3. Then the actual physical electric field normal components $\mathbf{E}_1$ and $\mathbf{E}_2$ in the respective cells are obtained by

$$\mathbf{E}_1 = \frac{1}{\epsilon_1}\mathbf{D} = \frac{\epsilon_{\text{eff}}}{\epsilon_1}\mathbf{E}$$

$$\mathbf{E}_2 = \frac{1}{\epsilon_2}\mathbf{D} = \frac{\epsilon_{\text{eff}}}{\epsilon_2}\mathbf{E}. \tag{40}$$

If there were permeable materials, the effective permeability μ_{eff} would have to be used. By analogy, it would be calculated similarly to the effective permittivity above by swapping $E \leftrightarrow H$, $D \leftrightarrow B$, and $\epsilon \leftrightarrow \mu$. In the E-cell case, the magnetic field of the FDTD simulation would be an effective field, and in the case of H cells, the magnetic field would be the actual physical field.

In summary, in the H-cell case, the actual physical unknowns are the magnetic field and the effective electric field which is closely related to the physical electric flux density by (37).

The E-cell case, which is the "usual" approach used in literature, is treated analogously. In this case, the physical unknowns are the electric field and the magnetic flux density. If the materials are nonpermeable, then the magnetic flux density $\mathbf{B}$

is essentially the same as the magnetic field $\mathbf{H}$ (specifically: $\mathbf{B} = \mu_0\mathbf{H}$), and both the electric and magnetic fields of the FDTD simulation are the actual physical quantities.

The E-cell and H-cell approaches generally give slightly different results, and their effect on the SAR values will be studied in the latter sections. The H-cell approach may seem awkward compared to the usual E-cell approach, but one cannot say the E-cell approach is strictly better. In fact, as will be shown in Section 6.2, both approaches may give good or bad results depending on the situation. Also, when magnetic materials are included in the simulation, both approaches are equally "good".

2.3.4 Staircase approximation

Staircase approximation is the simplest way to approximate curved material boundaries. In this work, the staircase approximation is done in the following way.

Assume an object $\mathcal{A} \subset \mathcal{D}$ consisting of some material in the calculation region. The discrete location vector is defined by

$$\mathbf{r} : (i, j, k) \mapsto (x(i), y(j), z(k)), \quad (i, j, k) \in \mathcal{I}, \tag{41}$$

where x, y and z are as defined in (13) and (14). Assuming that the material cells are X cells, where $X \in \{E, H\}$, we get the staircase approximation $\mathcal{I}_A \subset \mathcal{I}_X$ of the object $\mathcal{A}$ by

$$\mathcal{I}_A = \{\mathbf{p} \in \mathcal{I}_X : \mathbf{r}(\mathbf{p}) \in \mathcal{A}\}. \tag{42}$$

This means that the cell belongs to the object, if the location of the center point of the cell is within the object. We can now set the material parameters of the cells accordingly.

For example, the staircase approximation of a sphere centered in $\mathbf{r}_0 \in \mathcal{D}$ with radius a is done in the following way. For a cell $\mathbf{p} \in \mathcal{I}_X$, $X \in \{E, H\}$ (center point $\mathbf{r}(\mathbf{p})$): If the inequality

$$|\mathbf{r}(\mathbf{p}) - \mathbf{r}_0| < a \tag{43}$$

holds, then the cell belongs to the sphere. This is illustrated in Figure 4, which shows the staircase approximation of two equicentric spheres with different radii. The grid in the figure may be either E or H grid.

2.3.5 Packed coefficients

In many applications, there are only a relatively small number of distinct materials in the computational domain, e.g. this is the case with most human voxel models. In such a case, the memory requirements of storing the coefficients C_a and C_b can be reduced.

Assume there is N number of different media in the calculation domain (N includes the number of effective materials at voxel edges and sides). Then the coefficients C_a and C_b will only have N distinct values.

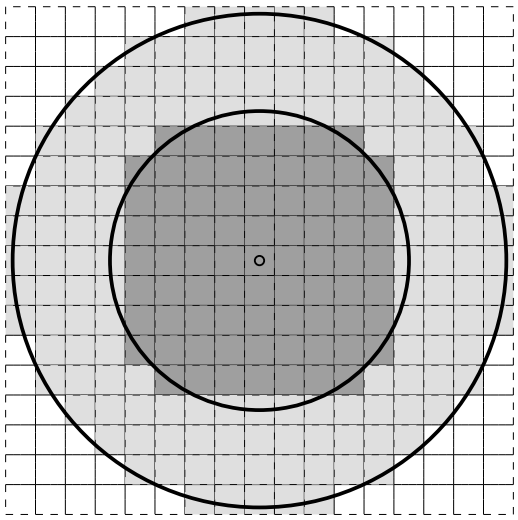

Figure 4: Staircase approximation of two equicentric spheres with different radii.

Defining a mapping

$$M_u : \mathcal{I}_{E_u} \to \{1, \ldots, N\}, \quad u \in \{x, y, z\} \tag{44}$$

and $\tilde{C}_a$ and $\tilde{C}_b$ so that

$$\begin{array}{l} C_a(\mathbf{p}) = \tilde{C}_a(M_u(\mathbf{p})) \\ C_b(\mathbf{p}) = \tilde{C}_b(M_u(\mathbf{p})) \end{array} \quad \mathbf{p} \in \mathcal{I}_{E_u},\ u \in \{x, y, z\} \tag{45}$$

we only need to store vectors $\tilde{C}_a$ and $\tilde{C}_b$, and the three material tables M_u. The memory requirements are thus two vectors of length N and three integer tables, with a total number of elements

$$\#(\mathcal{I}_{E_x}) + \#(\mathcal{I}_{E_y}) + \#(\mathcal{I}_{E_z}) \approx 3K_xK_yK_z.$$

Without the above approach, we would have to store floating-point tables C_a and C_b, totaling

$$2\#(\mathcal{I}_{E_x} \cup\ \mathcal{I}_{E_y} \cup\ \mathcal{I}_{E_z}) \approx 6K_xK_yK_z$$

elements.

For example, assuming 4 byte floating point numbers and 2 byte integer numbers, the packed-coefficients approach would cut the memory requirements of storing the material information to one fourth.

With packed coefficients, the H-cell approach presented in the previous section is a little better than the traditional E-cell approach. The total number of different effective material parameters N will be smaller, because the effective parameters of the H-cell case are combinations of the parameters of two neighboring cells, and with the E cells, they are combinations of four.

2.3.6 Human body models in FDTD

Usually human body models for FDTD consist of a three-dimensional table, which tells the tissue type in each cell. There are usually only a few dozen tissue types, each of which has a (frequency dependent) permittivity and conductivity, and density. This kind of structure is ideal for the packed-coefficients approach, as described in Section 2.3.5. For example, if we want the material parameters for a different frequency, we only need to change the vectors $\tilde{C}_a$ and $\tilde{C}_b$ accordingly. Everything else stays the same.

In this work, the material parameters of tissues at different frequencies are determined as presented in [4], [5], [6], and calculated using a web resource [7].

Resolutions of available human voxel models typically range from 0.5 mm to 10 mm. In the frequency range used by mobile communications (900 MHz–2140 MHz), the resolutions need to be finer than 4 mm–1.8 mm in order to satisfy the $\lambda/10$ rule inside the body.

In addition to producing a larger discretization error (26), too coarse resolutions may fail to model the important anatomical details of the body. One of the most significant of these is the skin. An adult has usually a skin thickness of 2–3 mm. If the resolution is coarser than this, the skin will be thicker (1 cell), or there will be areas without skin. This may have a large impact on the energy absorption inside the body at least at higher frequencies, when the penetration depth is smaller.

Various human body models of different sizes and shapes have been developed. Visible man [8] (based on data from the Visible Human Project [9]), Norman [10] and Zubal [11] voxel models will be used in this work. Their measures are presented in Table 1. The masses of the models depend on the choice of the density of the tissues. The densities used in this work are presented in Table 2. They are similar to the densities used in [8].

The resolutions of the models range from 1 mm (Visible man) to 3.6 mm (Zubal), and are also presented in Table 1. Anatomical resolution means the resolution with which the models are constructed from anatomical data (by whatever means). The resolution can be increased to get a smaller discretization error e.g. by the method presented in Section 6.5.1.

The physiques and postures of the three models are illustrated in Figure 5. The figure is only suggestive: The models in the figure might be slightly out of scale in relation to each other, and the coloring of one model does not necessarily match the coloring of the other models. Zubal and Visible man have their arms angled in front of the body, and Norman's arms are positioned along the body sides.

The International Commission on Radiological Protection (ICRP) reference man [12] has weight and height 73 kg and 176 cm, respectively. Of the three models used, Norman is the closest to the reference, and can be made to match the measures of the reference man almost exactly with a slight scaling. Norman is the only model which has normal weight, while Zubal is overweight, and Visible man is obese[3].

[3]By the Body-mass index (BMI)

Table 1: Heights and weights of human body models used in this work. The densities of the tissues are presented in Table 2. The resolution of the Norman model is scaled slightly to produce the height and weight of the ICRP reference man.

Model	(Anatomical) resolution	Height	Weight
Visible man	3 mm	186 cm	105.4 kg
Visible man	1 mm	186 cm	105.3 kg
Norman	2.022 mm	176 cm	73.0 kg
Zubal	3.6 mm	176 cm	81.9 kg

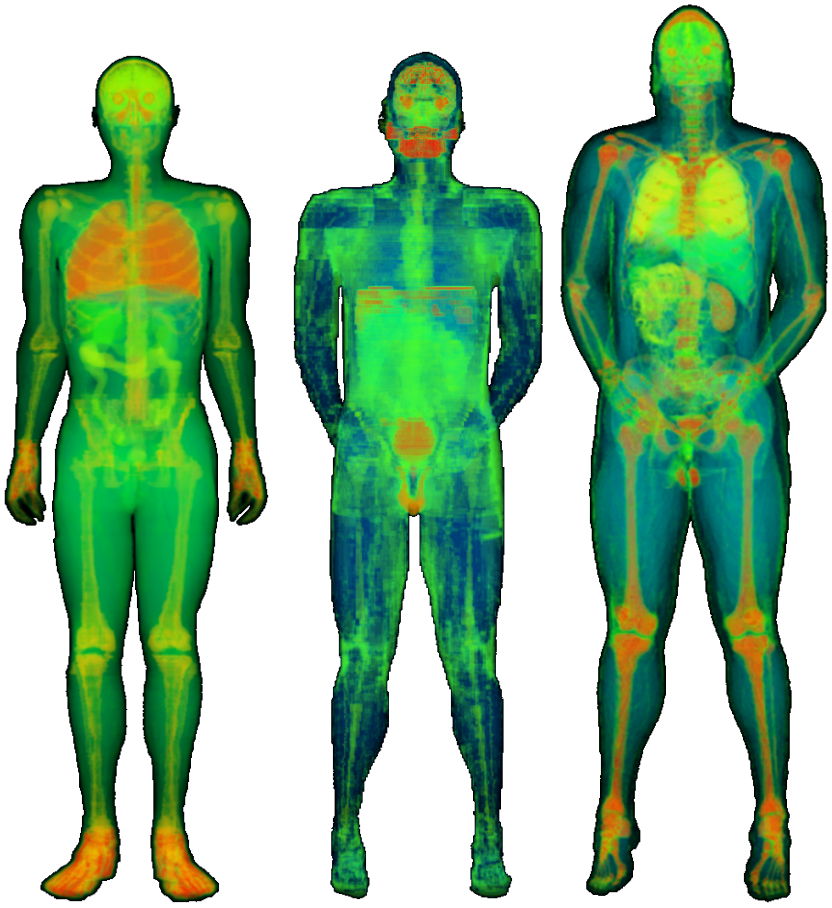

Figure 5: Norman (left), Zubal and Visible man

Table 2: Tissue densities used in this work.

Tissue	Density [g/cm^3]
Bile	1.0100
Bladder	1.0300
Blood	1.0580
Blood vessel	1.0400
Body fluid	1.0100
Bone (cancellous)	1.9200
Bone (cortical)	1.9900
Bone marrow	1.0400
Cartilage	1.0970
Cerebellum	1.0380
Cerebral spinal fluid	1.0072
Eye (cornea)	1.0760
Eye (lens)	1.0530
Eye (sclera/wall)	1.0260
Fat	0.9160
Gall bladder	1.0300
Glands	1.0500
Gray matter	1.0380
Heart	1.0298
Intestine	1.0425
Ligaments	1.2200
Liver	1.0300
Lung (inner)	0.2600
Lung (outer)	1.0500
Lymph	1.0400
Muscle	1.0469
Muscous membrane	1.0400
Nails (toe and finger)	1.0300
Nerve (spine)	1.0380
Pancreas	1.0450
Skin/dermis	1.1250
Spleen	1.0541
Stomach	1.0500
Testicles	1.0440
Tooth	2.1600
White matter	1.0380

3 Absorbing boundary conditions

As available memory for computation is finite, modeling of unbounded domains must be done by using special absorbing boundary conditions (ABCs) to terminate the FDTD lattice. These boundary conditions simulate an infinite region by making the reflection from the boundary as small as possible.

A number of analytical ABCs have been used (see e.g. [1]). Today, the most commonly used absorbing boundary conditions are the perfectly matched layer (PML) absorbing boundary conditions, first introduced by Bérenger in 1994 [13]. These include Bérenger's original split-field PML, uniaxial (or unsplit) PML (UPML) [14] and convolutional PML (CPML) [15]. Only the CPML absorbing boundary conditions are studied in this work. The advantages of PML over analytical ABCs include: the studied structures can be very close to the ABC, and PML is better suited for parallel computing [16].

The basic idea of PML is impedance matching between the PML region and free space, which makes the reflection from the PML boundary as small as possible (zero in the continuous situation) for all incident angles and frequencies. Additionally, the PML material is a "lossy" material, so the traveling waves are attenuated inside the PML, and the FDTD lattice can be terminated with PEC when the wave has decayed enough. These properties allow the PML to absorb incoming waves nearly "perfectly".

3.1 PML equations

Here we will derive some properties of PML materials, using the "coordinate stretching" approach, which was first introduced by Chew and Weedon in 1994 [16].

Introduce a change of variables

$$\tilde{x}(\omega) = \int_0^x s_x(\omega, x')dx'; \quad \tilde{y}(\omega) = \int_0^y s_y(\omega, y')dy'; \quad \tilde{z}(\omega) = \int_0^z s_z(\omega, z')dz', \tag{46}$$

where $\{s_u\}$ are the *coordinate stretching variables*, which may be complex. The ∇ operator in these coordinates[4] can be written

$$\hat{\nabla}_s = \mathbf{u}_x \frac{\partial}{\partial \tilde{x}} + \mathbf{u}_y \frac{\partial}{\partial \tilde{y}} + \mathbf{u}_z \frac{\partial}{\partial \tilde{z}} = \mathbf{u}_x \frac{1}{s_x}\frac{\partial}{\partial x} + \mathbf{u}_y \frac{1}{s_y}\frac{\partial}{\partial y} + \mathbf{u}_z \frac{1}{s_z}\frac{\partial}{\partial z}. \tag{47}$$

Next, we write the Maxwell's equations in frequency domain in the coordinates $(\tilde{x}, \tilde{y}, \tilde{z})$. A time-dependence $e^{j\omega t}$ is assumed.

$$j\omega\epsilon\mathbf{E} = \hat{\nabla}_s \times \mathbf{H} \tag{48}$$

$$-j\omega\mu\mathbf{H} = \hat{\nabla}_s \times \mathbf{E} \tag{49}$$

In a homogeneous and isotropic medium with material parameters ϵ and μ, a general, homogeneous plane wave has the form

$$\mathbf{E} = \mathbf{E}_0 e^{-j\mathbf{k}\cdot\mathbf{r}}, \quad \mathbf{H} = \mathbf{H}_0 e^{-j\mathbf{k}\cdot\mathbf{r}}, \tag{50}$$

[4]Here the hatted nabla ($\hat{\nabla}$) means that the operator is in frequency domain.

where

$$\mathbf{k} = \mathbf{u}_x k_x + \mathbf{u}_y k_y + \mathbf{u}_z k_z. \tag{51}$$

Substituting (50) into the modified Maxwell's equations (48) and (49) yields

$$\mathbf{k}_s \times \mathbf{E} = \omega\mu\mathbf{H} \tag{52}$$

$$\mathbf{k}_s \times \mathbf{H} = -\omega\epsilon\mathbf{E}, \tag{53}$$

where

$$\mathbf{k}_s = \mathbf{u}_x \frac{k_x}{s_x} + \mathbf{u}_y \frac{k_y}{s_y} + \mathbf{u}_z \frac{k_z}{s_z}. \tag{54}$$

Substituting (53) into (52) gives

$$\omega^2\mu\epsilon\mathbf{H} = -\mathbf{k}_s \times \mathbf{k}_s \times \mathbf{H} = -\mathbf{k}_s(\mathbf{k}_s \cdot \mathbf{H}) + \mathbf{H}(\mathbf{k}_s \cdot \mathbf{k}_s). \tag{55}$$

As $\mathbf{k}_s \cdot \mathbf{H} = 0$ due to (52), this gives the dispersion relation in PML:

$$\omega^2\mu\epsilon = \mathbf{k}_s \cdot \mathbf{k}_s = \frac{k_x^2}{s_x^2} + \frac{k_y^2}{s_y^2} + \frac{k_z^2}{s_z^2}. \tag{56}$$

3.2 Reflection from PML interfaces

Assume a plane wave incident on the boundary of two homogeneous and isotropic materials. The angle of incidence and the polarization of the wave are arbitrary. The situation is shown in Figure 6.

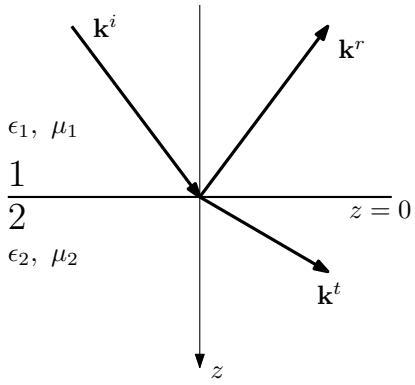

Figure 6: The wave numbers $\mathbf{k}$ when an incident plane wave reflects from the interface of materials 1 and 2.

Region 1 ($z < 0$) has material parameters ϵ_1 and μ_1, and coordinate stretching variables $\{s_{1u}\}$. Incident plane wave is notated with superscript 'i', and the reflected wave with 'r'.

Region 2 ($z > 0$) has material parameters ϵ_2 and μ_2, and coordinate stretching variables $\{s_{2u}\}$. Transmitted wave is notated with a superscript 't'.

In half space 1 ($z < 0$), the total electric field is of the form

$$\mathbf{E}_1(\mathbf{r}) = \mathbf{E}^i e^{-j\mathbf{k}^i \cdot \mathbf{r}} + \mathbf{E}^r e^{-j\mathbf{k}^r \cdot \mathbf{r}} \tag{57}$$

and in half space 2 ($z > 0$)

$$\mathbf{E}_2(\mathbf{r}) = \mathbf{E}^t e^{-j\mathbf{k}^t \cdot \mathbf{r}}. \tag{58}$$

Magnetic fields in both regions can be acquired using plane wave condition (52):

$$\mathbf{H}_1 = \frac{\mathbf{k}_s^i}{\omega\mu_1} \times \mathbf{E}^i e^{-j\mathbf{k}^i \cdot \mathbf{r}} + \frac{\mathbf{k}_s^r}{\omega\mu_1} \times \mathbf{E}^r e^{-j\mathbf{k}^r \cdot \mathbf{r}} \tag{59}$$

and

$$\mathbf{H}_2 = \frac{\mathbf{k}_s^t}{\omega\mu_2} \times \mathbf{E}^t e^{-j\mathbf{k}^t \cdot \mathbf{r}}. \tag{60}$$

On the interface $z = 0$, denote the coordinate vector $\rho = x\mathbf{u}_x + y\mathbf{u}_y$. It follows from (48) (similarly to standard Maxwell equations; $\{s_u\}$ are assumed to behave "well enough") that the electric and magnetic field tangential components are continuous across interfaces. Here we denote the tangential components of the fields on the interface by subscript 'tan'. Thus, on the interface, for all ρ

$$\begin{array}{rcl} \mathbf{E}_{1\tan} & = & \mathbf{E}_{2\tan} \\ & \Leftrightarrow & \\ \mathbf{E}^i_{\tan} e^{-j\mathbf{k}^i \cdot \rho} + \mathbf{E}^r_{\tan} e^{-j\mathbf{k}^r \cdot \rho} & = & \mathbf{E}^t_{\tan} e^{-j\mathbf{k}^t \cdot \rho}. \end{array} \tag{61}$$

As the above must hold for all ρ, that implies

$$\mathbf{k}^i_{\tan} = \mathbf{k}^r_{\tan} = \mathbf{k}^t_{\tan}, \tag{62}$$

which is the Snell's Law (unchanged from the standard Maxwell's equations), and

$$\mathbf{E}^i_{\tan} + \mathbf{E}^r_{\tan} = \mathbf{E}^t_{\tan}. \tag{63}$$

From the dispersion relation (56) in region 1 and Snell's Law (62) follows $(k_z^r)^2 = (k_z^i)^2$. Choose $k_z^r = -k_z^i$ and define

$$\begin{array}{c} k_{1z} = k_z^r = -k_z^i \\ k_{2z} = k_z^t. \end{array} \tag{64}$$

The continuity of the magnetic field tangential component gives, using (59) and (60),

$$\left(\frac{\mathbf{k}_s^i}{\mu_1} \times \mathbf{E}^i + \frac{\mathbf{k}_s^r}{\mu_1} \times \mathbf{E}^r \right)_{\tan} = \left(\frac{\mathbf{k}_s^t}{\mu_2} \times \mathbf{E}^t \right)_{\tan}, \tag{65}$$

where $\{\mathbf{k}_s^v : v = i, r, t\}$ are defined as in (54), using the coordinate stretching variables $\{s_{1u}\}$ for $\mathbf{k}_s^i$ and $\mathbf{k}_s^r$; and $\{s_{2u}\}$ for $\mathbf{k}_s^t$.

A plane wave can be decomposed into a sum of TE^z and TM^z polarized components, for which either the electric (TE^z) or magnetic (TM^z) fields are transverse to the normal of the interface ($\mathbf{u}_z$). First, we will only consider the TE polarization.

Substitute (63) into (65), which gives

$$\left(\frac{\mathbf{k}_s^i}{\mu_1} \times \mathbf{E}^i + \frac{\mathbf{k}_s^r}{\mu_1} \times \mathbf{E}^r \right)_{\tan} = \left(\frac{\mathbf{k}_s^t}{\mu_2} \times (\mathbf{E}^i + \mathbf{E}^r) \right)_{\tan}. \tag{66}$$

As the electric field is transversal to z direction, rearranging terms, taking the tangential components and substituting (54) and (64) into the above equation gives

$$\left(\frac{k_{1z}}{\mu_1 s_{1z}} - \frac{k_{2z}}{\mu_2 s_{2z}}\right)(\mathbf{u}_z \times \mathbf{E}^i) = \left(\frac{k_{1z}}{\mu_1 s_{1z}} + \frac{k_{2z}}{\mu_2 s_{2z}}\right)(\mathbf{u}_z \times \mathbf{E}^r) \tag{67}$$

The reflection coefficient R^{TE} is thus

$$R^{\mathrm{TE}} = \frac{|\mathbf{E}^r|}{|\mathbf{E}^i|} = \frac{k_{1z}s_{2z}\mu_2 - k_{2z}s_{1z}\mu_1}{k_{1z}s_{2z}\mu_2 + k_{2z}s_{1z}\mu_1}. \tag{68}$$

For TM polarization, the reflection coefficient can be acquired similarly, and the result is

$$R^{\mathrm{TM}} = \frac{|\mathbf{H}^r|}{|\mathbf{H}^i|} = \frac{k_{1z}s_{2z}\epsilon_2 - k_{2z}s_{1z}\epsilon_1}{k_{1z}s_{2z}\epsilon_2 + k_{2z}s_{1z}\epsilon_1}. \tag{69}$$

Now choose the material parameters

$$\begin{aligned} \mu_1 &= \mu_2 = \mu \\ \epsilon_1 &= \epsilon_2 = \epsilon \\ s_{1x} &= s_{2x} = s_x \\ s_{1y} &= s_{2y} = s_y. \end{aligned} \tag{70}$$

From the dispersion relation (56) and Snell's Law (62), we get a relation for k_{1z} and k_{2z}

$$\frac{k_{1z}}{s_{1z}} = \sqrt{\omega^2\mu\epsilon - \frac{k_x^2}{s_x^2} - \frac{k_y^2}{s_y^2}} = \frac{k_{2z}}{s_{2z}} \tag{71}$$

Substituting (70) and (71) into the expressions for reflection coefficients (68) and (69), we obtain

$$R^{\mathrm{TE}} = R^{\mathrm{TM}} = 0.$$

This holds for all frequencies and angles of incidence of the plane wave. Here the incident plane wave was assumed to be homogeneous, but the above also holds for general nonhomogeneous plane waves [17].

The above holds for arbitrary s_{1z} and s_{2z}. For example, if region 1 is air ($s_{1z} = 1$), and we choose s_{2z} to be a complex number, it follows from (56) that the corresponding k_{2z} will also be complex, and the wave will attenuate in the direction of the z axis in region 2.

3.3 PML equations in time domain

$\hat{\nabla}_s$-operator inside the PML in the frequency domain was

$$\hat{\nabla}_s = \mathbf{u}_x \frac{1}{s_x}\frac{\partial}{\partial x} + \mathbf{u}_y \frac{1}{s_y}\frac{\partial}{\partial y} + \mathbf{u}_z \frac{1}{s_z}\frac{\partial}{\partial z}.$$

Stretching coefficients $\{s_u\}$ may depend on the frequency ω, so to express this operator in time domain, calculation of convolution is (generally) necessary. In time domain, ∇_s becomes

$$\nabla_s = \mathbf{u}_x \mathcal{F}^{-1}\left(\frac{1}{s_x}\right) * \frac{\partial}{\partial x} + \mathbf{u}_y \mathcal{F}^{-1}\left(\frac{1}{s_y}\right) * \frac{\partial}{\partial y} + \mathbf{u}_z \mathcal{F}^{-1}\left(\frac{1}{s_z}\right) * \frac{\partial}{\partial z}. \tag{72}$$

3.4 Complex frequency-shifted tensor

The so-called complex frequency-shifted tensor (CFS) coefficient has proven to be a "good" choice for the stretching coefficients $\{s_u\}$

$$s_u = \kappa_u + \frac{\sigma_u}{a_u + j\omega\epsilon_0}, \quad u \in \{x, y, z\}, \tag{73}$$

where σ_u and a_u are non-negative real numbers and $\kappa_u \geq 1$. This choice of coordinate stretching parameter holds Berenger's original PML as a special case ($\kappa_u = 1$, $a_u = 0$).

Performing an inverse Fourier transform to the CFS parameters $\{s_u\}$ gives

$$\mathcal{F}^{-1}\left(\frac{1}{s_u}\right)(t) = \mathcal{F}^{-1}\left(\frac{1}{\kappa_u + \frac{\sigma_u}{a_u + j\omega\epsilon_0}}\right)(t) = \frac{\delta(t)}{\kappa_u} - \frac{\sigma_u}{\epsilon\kappa_u^2} e^{-\left(\frac{\sigma_u}{\kappa} + a_u\right)\frac{t}{\epsilon}}\Theta(t) = \frac{\delta(t)}{\kappa_u} + \zeta_u(t), \tag{74}$$

where $\Theta(t)$ denotes the unit step function.

Substituting above to the ∇_s in (72) gives

$$\nabla_s = \nabla_\kappa + \nabla^* \tag{75}$$

where

$$\nabla_\kappa = \mathbf{u}_x \frac{1}{\kappa_x}\frac{\partial}{\partial x} + \mathbf{u}_y \frac{1}{\kappa_y}\frac{\partial}{\partial y} + \mathbf{u}_z \frac{1}{\kappa_z}\frac{\partial}{\partial z} \tag{76}$$

$$\nabla^* = \mathbf{u}_x \zeta_x * \frac{\partial}{\partial x} + \mathbf{u}_y \zeta_y * \frac{\partial}{\partial y} + \mathbf{u}_z \zeta_z * \frac{\partial}{\partial z}, \tag{77}$$

where

$$\zeta_u(t) = -\frac{\sigma_u}{\epsilon\kappa_u^2} e^{-\left(\frac{\sigma_u}{\kappa} + a_u\right)\frac{t}{\epsilon}}\Theta(t), \quad u \in \{x, y, z\} \tag{78}$$

3.5 Convolutional PML

Convolutional PML (CPML) is an efficient implementation of the CFS-PML presented in the previous section. CPML was introduced by Roden and Gedney in 2000 [15].

Whereas Bérenger's original split-field-PML and UPML implementations try to avoid calculating convolution, it is calculated in CPML. The convolution is calculated using the recursive-convolution (RC) technique [18].

Using the notation from the previous section, we can write the modified Maxwell's equations (48) and (49) in time domain in the form

$$\frac{\partial}{\partial t}\mathbf{H} = -\frac{1}{\mu}\left(\nabla_\kappa \times \mathbf{E} + \nabla^* \times \mathbf{E}\right) \tag{79}$$

$$\frac{\partial}{\partial t}\mathbf{E} = -\frac{\sigma}{\epsilon}\mathbf{E} + \frac{1}{\epsilon}\left(\nabla_\kappa \times \mathbf{H} + \nabla^* \times \mathbf{H}\right), \tag{80}$$

where ∇_κ and ∇^* are defined in (76) and (77).

We see that $\nabla_\kappa\times$ can be discretized similarly to the regular $\nabla\times$-operator (19): The cell widths $\{\Delta u\}$ in the denominators of the finite difference approximations (20)–(22) are multiplied by $\{\kappa_u\}$. Here $\{\kappa_u\}$-parameters can be interpreted to just stretch the cell sizes in spatial coordinates. We denote the discretized operator by $\nabla_\kappa\otimes$.

Discretizing $\nabla^*\times$ requires a little more work, as it is dependent on both time and spatial location. Let us notate the required convolutions with

$$\Psi_u X(t) = \left(\zeta_u * \frac{\partial}{\partial u} X\right)(t) = \int_0^t \zeta_u(\tau)\frac{\partial}{\partial u}X(t-\tau)d\tau, \quad u \in \{x,y,z\}, \tag{81}$$

where $X = X(t)$ may be any field component.

Now, if we assume that X is piecewise constant (in time), we can approximate the convolution at $t = n\Delta t$ by

$$\begin{aligned}\Psi_u X^n &= \int_0^{n\Delta t} \zeta_u(\tau)\frac{\partial}{\partial u}X(n\Delta t-\tau)d\tau \approx \sum_{m=0}^{n-1}\frac{\partial}{\partial u}X^{n-m}\int_{m\Delta t}^{(m+1)\Delta t}\zeta_u(\tau)d\tau \\ &= \sum_{m=0}^{n-1}\frac{\partial}{\partial u}X^{n-m}Z_u^m,\end{aligned} \tag{82}$$

where

$$\begin{aligned}Z_u^m &= \int_{m\Delta t}^{(m+1)\Delta t}\zeta_u(\tau)d\tau = -\frac{\sigma_u}{\epsilon\kappa_u^2}\int_{m\Delta t}^{(m+1)\Delta t} e^{-\left(\frac{\sigma_u}{\kappa}+a_u\right)\frac{\tau}{\epsilon}}d\tau \\ &= c_u(b_u)^m,\end{aligned} \tag{83}$$

where

$$c_u = \frac{\sigma_u}{\sigma_u\kappa_u + \kappa_u^2 a_u}\left(e^{-\left(\frac{\sigma_u}{\kappa}+a_u\right)\frac{\Delta t}{\epsilon}} - 1\right), \tag{84}$$

$$b_u = e^{-\left(\frac{\sigma_u}{\kappa}+a_u\right)\frac{\Delta t}{\epsilon}}. \tag{85}$$

Calculation of the sum in (82) can be done recursively. First, we rearrange the sum, and utilize $Z_u^{m+1} = b_u Z_u^m$ and $Z_u^0 = c_u$ from (83).

$$\Psi_u X^n = \sum_{m=1}^{n-1}\frac{\partial}{\partial u}X^{n-m}Z_u^m + \frac{\partial}{\partial u}X^n Z_u^0 = \underbrace{\sum_{m=0}^{n-2}\frac{\partial}{\partial u}X^{(n-1)-m}Z_u^{m+1}}_{b_u\Psi_u X^{n-1}} + \frac{\partial}{\partial u}X^n.\underbrace{Z_u^0}_{c_u}$$

We get

$$\Psi_u X^n = b_u\Psi_u X^{n-1} + c_u\frac{\partial}{\partial u}X^n. \tag{86}$$

Replacing the spatial derivates in (86) with their central difference approximations (20)–(22), we can write the discretized $\nabla^*\times$ operator as

$$\nabla^*\times \approx \nabla^*\otimes = \begin{bmatrix} 0 & -\Psi_z & \Psi_y \\ \Psi_z & 0 & -\Psi_x \\ -\Psi_y & \Psi_x & 0 \end{bmatrix}. \tag{87}$$

Now, we get the FDTD update equations inside the PML by replacing the operator $\nabla\otimes$ in the update equations (23) and (24) with $\nabla_\kappa \otimes + \nabla^*\otimes$. By defining $\kappa_u = 1$ outside the PML region, we can use the same $\nabla_\kappa\otimes$ in the entire calculation region, as $\nabla_\kappa\otimes \equiv \nabla\otimes$ outside the PML. Also, $\sigma_u \equiv 0$ and thus $\nabla^*\otimes \equiv \mathbf{0}$ outside the PML.

The outer PEC boundaries are covered with a PML material coating as shown in Figure 7. The motivation is that the fields penetrate into the PML without reflection, and inside the PML, they are essentially attenuated to zero. This simulates a free-space situation.

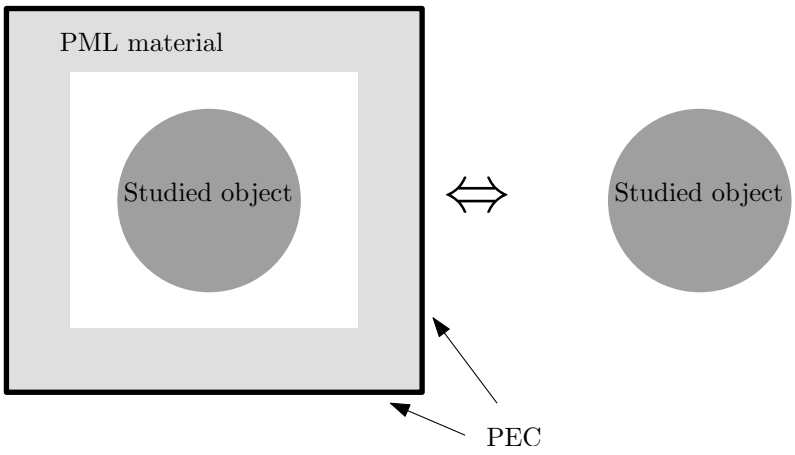

Figure 7: The principle of PML absorbing boundary conditions. The outer boundaries are coated with PML material which absorbs incoming waves without reflection, thus simulating a free-space case.

We need to store the quotients $\{\Psi_u X\}$, as their values at the previous time step are needed in updating. However, some of these are zeros: Along the sides parallel to x, y and z axes, only s_x, s_y or s_z is nonunity, respectively. Thus for example $\Psi_x = 0$ and $\Psi_y = 0$ along the z boundaries. In the edges or corners of the calculation region, two or three of the coefficients $\{s_u\}$ are nonunity.

A total of 12 quotients need to be stored near the boundaries, and updated at each time step using (86):

- $\Psi_x E_y$, $\Psi_x E_z$, $\Psi_x H_y$ and $\Psi_x H_z$ along the x boundary
- $\Psi_y E_x$, $\Psi_y E_z$, $\Psi_y H_x$ and $\Psi_y H_z$ along the y boundary
- $\Psi_z E_x$, $\Psi_z E_y$, $\Psi_z H_x$ and $\Psi_z H_y$ along the z boundary

In the latter sections, the performance of CPML will be tested in simulations, and its applicability in FDTD SAR calculations will be verified.

3.6 Scaling of the CFS parameters

While the reflection from PML was proven to be zero in a continuous space in Section 3.2, the discretization error of space causes reflection in practical simulations (see e.g. [1], [19]).

In order to make this reflection smaller, the contrast in air-PML and PML-PML interfaces needs to be made smaller. Thus we cannot set the PML conductivities $\{\sigma_u\}$ arbitrarily large, which would absorb the incident waves arbitrarily well, using only arbitrarily thin PML regions on the outer boundaries of the calculation domain.

In practice, PML regions will have to be thicker than 1 cell for them to be of any use. Thicker PML allows "smoother" transition of parameters, and also, the attenuation is increased.

Assume that the PML regions have a thickness d in E cells. Choose the coordinates for representing the scaling as shown in Figure 8.

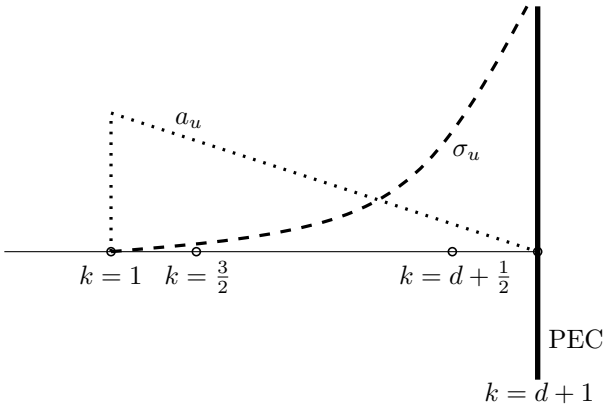

Figure 8: Scaling of the CFS parameters a_u and σ_u inside the PML.

Parameters $\{\sigma_u\}$ in (73) represent "conductivity" within the PML. They are scaled so that they are small near the air-to-PML boundary, and increase when closing in to the outer PEC boundaries. In this work, a polynomial grading is used. It has the form

$$\sigma_u(k) = \left(\frac{k-1}{d}\right)^m \sigma_{\max}, \quad k = 1, \frac{3}{2} \ldots, d, d + \frac{1}{2} \tag{88}$$

Here m is the order of the polynomial grading, k means the coordinate indices and $\sigma_{\max}$ is the maximum value. A good choice for $\sigma_{\max}$ has proven ([1],[15]) to be

$$\sigma_{\max} = \sigma_{\text{opt}}(m, \Delta) \approx \frac{m+1}{150\pi\sqrt{\epsilon_r}\Delta}. \tag{89}$$

$\{\kappa_u\}$ can be interpreted to stretch the cells in the PML, which can increase absorption. Usually, they use a similar scaling to $\{\sigma_u\}$

$$\kappa_u(k) = 1 + \left(\frac{k-1}{d}\right)^m (\kappa_{\max} - 1), \quad k = 1, \frac{3}{2} \ldots, d, d + \frac{1}{2} \tag{90}$$

Parameters $\{a_u\}$, the meaning of which is to prevent reflection of evanescent waves from the PML interfaces, are scaled contrary to the other parameters. In fact, they make the PML perform poorer by reducing the attenuation [19]. Otherwise, evanescent waves would attenuate too quickly inside the PML and cause numerical

reflection due to the discretization error [17]. $\{a_u\}$ should be large near the air-PML interface and reduce to zero at the outer boundaries

$$a_u(k) = \left(\frac{d-k+1}{d}\right)^{m_a} a_{\max}, \quad k = 1, \frac{3}{2} \ldots, d, d+\frac{1}{2}. \tag{91}$$

4 Sources and excitation signals

In the previous sections, we have described the actual FDTD algorithm, modeling materials in FDTD, and absorbing boundary conditions. The only piece missing is the modeling of sources which excite the fields.

In this section, we will cover discrete sources and the plane wave source, as well as different excitation signals: sinusoidal excitation and pulse (transient) excitation. Finally, some aspects of modeling base station antennas are presented.

4.1 Discrete sources

A discrete port is one of the simplest ways to excite the fields in a FDTD simulation. It is basically a voltage source V_g with an inner resistance R_g, as shown in Figure 9.

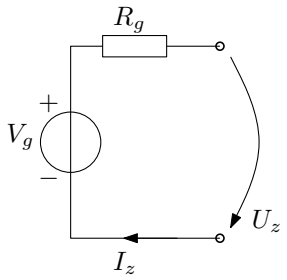

Figure 9: Voltage source V_g with an inner resistance R_g.

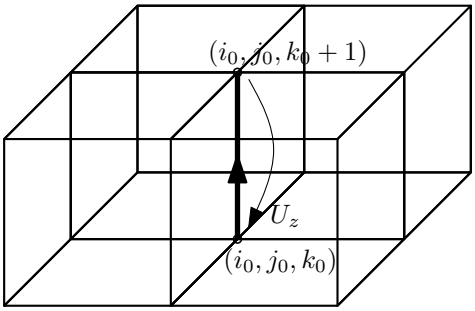

Figure 10: The voltage source in the FDTD lattice.

Assume the source is positioned in z direction at the marked edge in Figure 10. Thus the voltage U_z over the edge at $t = n\Delta t$ is given by

$$U_z^n \approx -E_z^n \Delta z, \tag{92}$$

where the spatial index of the electric field is $(i_0, j_0, k_0 + \frac{1}{2})$. The current I_z^n through the source is

$$I_z^n = \frac{-U_z^n + V_g^n}{R_g}. \tag{93}$$

Thus, the source current density $\mathbf{J}_s^n$ is given by

$$(\mathbf{J}_s^n)_z \approx \frac{I_z^n}{\Delta x \Delta y} \approx \frac{\Delta z}{R_g \Delta x \Delta y} E_z^n + \frac{V_g^n}{R_g \Delta x \Delta y}. \tag{94}$$

On the right hand side, the first term is the form conductivity times electric field.

Ampere's Law (5) in a domain which includes the source current density $\mathbf{J}_s$ is

$$\frac{\partial}{\partial t}\mathbf{E} = -\frac{\sigma}{\epsilon}\mathbf{E} + \frac{1}{\epsilon}\nabla \times \mathbf{H} - \frac{1}{\epsilon}\mathbf{J}_s. \tag{95}$$

Discretizing this yields a slightly different update equation for E_z at $(i_0, j_0, k_0 + \frac{1}{2})$.

To calculate the average net input power from the discrete source, one needs the amplitudes and phases of the (complex) current I_z and voltage U_z. The method for getting these from the time-dependent values is presented in the next section for the case of sinusoidal excitation. Then the net input power (rms) from the discrete source can be calculated by

$$P_{\text{net}}(\omega) = \frac{1}{2}\text{Re}\{U_z I_z^*\} \tag{96}$$

where $*$ means the complex conjugate. The net input power means the power which is fed into the simulation by the discrete source. It may either radiate away (absorb into the absorbing boundaries), or be absorbed in conducting media or other discrete sources.

The gross input power — the total power fed by the voltage source V_g, which includes the resistive loss in the inner resistance R_g — can be calculated by

$$P_{\text{gross}}(\omega) = -\frac{1}{2}\text{Re}\{V_g I_z^*\}. \tag{97}$$

4.2 Plane-wave source

A plane-wave source can be easily implemented in FDTD using the so-called total-field/scattered-field (TF/SF) technique (see e.g. [1]).

Assume the studied object is exposed to an arbitrary primary field $\mathbf{E}^p$ (here: plane wave). Then the total electric field $\mathbf{E}$ can be decomposed into the known primary field $\mathbf{E}^p$ and an unknown scattered field $\mathbf{E}^s$

$$\mathbf{E} = \mathbf{E}^s + \mathbf{E}^p, \tag{98}$$

where the primary field satisfies the homogeneous Maxwell's equations in free space[5]. The basic idea is to divide the calculation region into two regions as shown in Figure 11.

In the TF region, the total field is calculated, and in the SF region, only the scattered field is solved. Denote these fields in TF and SF regions by $\mathbf{E}_1$ and $\mathbf{E}_2$, respectively:

$$\mathbf{E}_1 = \mathbf{E}^s + \mathbf{E}^p \tag{99}$$

[5]We assume the absorbing boundaries are perfect, so the situation is essentially a free space case.

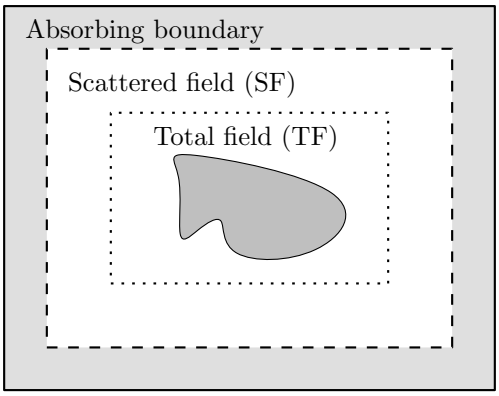

Figure 11: Total field-scattered field technique: the domain is divided into two regions. In reality, the TF/SF boundary would be closer to the absorbing boundary.

$$\mathbf{E}_2 = \mathbf{E}^s. \tag{100}$$

Thus, on the TF/SF-boundary

$$\mathbf{E}_1 = \mathbf{E}_2 + \mathbf{E}^p. \tag{101}$$

Both $\mathbf{E}_1$ and $\mathbf{E}_2$ satisfy the Maxwell's equations, and Yee's algorithm can be utilized to solve these separately in both regions. The update equations over the TF/SF boundary are altered according to (101). The details of this slight alteration are quite simple, and are not presented here. In the altered update equations, we need to know the values of the primary field on the boundary at each time step.

The case in which the primary field is a homogeneous plane wave (or a combination of those) is simple to implement. The values of the primary field on the TF/SF boundary can be computed by performing a 1D-FDTD simulation along with the actual simulation. The 1D simulation is excited by a "discrete source", the material parameters are constant (air), and the calculation domain is terminated with absorbing boundaries. The 1D solution is then easily extended to 3D because (by homogenity) the fields are constant on the planes perpendicular to the direction of propagation.

If the fields are sinusoidal with frequency ω_0, the electric field of a linearly polarized plane wave propagating in the $\mathbf{k}$ direction will be of the form

$$\mathbf{E}(\mathbf{r}; t) = \mathbf{u} E_0 \sin(\mathbf{k} \cdot \mathbf{r} - \omega_0 t),$$

where $\mathbf{u}$ is perpendicular to $\mathbf{k}$.

The (rms) power density S [W/m^2] of such a plane wave is

$$S = \frac{1}{2\eta} |E_0|^2, \tag{102}$$

where η is the wave impedance of the medium (in air $\eta = \eta_0 \approx 376.73$).

4.3 Sinusoidal excitation

Assume that all sources (plane wave, discrete sources) have a sinusoidal time dependence with the same frequency ω_0. For example, applying the sinusoidal excitation to a discrete source gives the time dependence for the voltage

$$V_g(t) = V_{g0} \sin(\omega_0 t + \varphi), \quad t \in \mathbb{R}.$$

When all the sources are sinusoidal and have the same frequency $\omega_0 = 2\pi f_0$, all field quantities X will also be sinusoidal for all $\mathbf{r} \in \mathcal{D}$

$$X(\mathbf{r}, t) = X_0(\mathbf{r}) \sin\left(\frac{2\pi}{T} t + \varphi(\mathbf{r})\right), \tag{103}$$

where $T = 1/f_0$ is the period. As can be easily verified, the amplitude $X_0(\mathbf{r})$ can be presented in the form

$$X_0(\mathbf{r}) = \sqrt{X(\mathbf{r}, t)^2 + X(\mathbf{r}, t - \frac{T}{4})^2}. \tag{104}$$

Equation (104) can be utilized to extract the amplitudes of the fields from FDTD simulations. Especially, for SAR calculation, this means the electric field amplitude.

The phase $\varphi(\mathbf{r})$ can be calculated

$$\varphi(\mathbf{r}) = -\tan^{-1}\left(\frac{X(\mathbf{r}, t)}{X(\mathbf{r}, t - \frac{T}{4})}\right), \tag{105}$$

where one must pay attention to the proper choice of the arcustangent branch.

When the fields are of the form (103), there is no need to model the frequency dependence of the materials, because the spectrum will only contain one frequency. The initial assumption of nondispersive material parameters in Section 2.1 was done with this in mind.

In FDTD simulations, the fields are initialized to zeros. That means, the sources are turned on at $t = 0$, and they are all zeros before that. Thus the sources are not strictly sinusoidal, and the fields will not generally be of the form (103). However, when the simulation has run long enough, the fields may (usually: will) eventually converge to (103). To determine a "long enough" simulation time, a *steady-state criterion*, which measures how well the solution has converged, is used.

Using (104) and (105) in FDTD requires the following two conditions to be met: Firstly, time steps per period must be an integer and divisible by four. Secondly, steady state must have been reached. Specifically, the time dependence of the fields has to be of the form (103). The first condition can be easily satisfied by choosing the time step length correctly before the simulation. The second condition will be satisfied when the simulation has run long enough, so that the steady-state criterion holds.

The convergence to the steady state can be made quicker by tapering the input sine signal, which means starting the input signal at zero amplitude and increasing the amplitude to its final value gradually over a few periods. This is discussed in Section 6.4.1.

4.4 Pulse excitation

The pulse excitation is an alternative for the sinusoidal excitation. The excitation signal is not an "infinite" sinusoidal signal but instead a pulse which has a finite duration.

Simplified, the approach can be written as follows:

1. Excite the sources using a pulse (usually a modulated Gauss pulse)
2. At $1/F$ intervals, record the desired quantities. F is the sampling frequency for the discrete Fourier transform, and is usually lower than $1/\Delta t$.
3. Repeat until energy has vanished from the system. This "energy criterion" is analogous to the steady-state criterion of the sinusoidal excitation.
4. Calculate a discrete Fourier transform for the desired quantities (in reality, this is done real time at step 2).

In theory, the results for a wide range of frequencies can be acquired by just one simulation. For large human-SAR computations, however, wide frequency range has limited practical benefits. Since the body's material parameters are frequency dependent (see Section 2.3.6), modeling them accurately would require calculating convolution and discrete Fourier transform, which would be a great computational burden. This was briefly discussed in Section 2.3.2.

If the frequency dependence of the materials is not taken into account, but the material parameters are fixed, as in (31) and (32), so that they are correct at a certain frequency, pulse excitation will only give the correct result at that single frequency. Other frequency components in the spectrum will be incorrect. In that sense, pulse excitation is not different from the sinusoidal excitation; both give the solution at a single frequency.

The pulse excitation is somewhat more complicated to implement than the sinusoidal excitation. Consequently, there seems to be little sense in using the pulse excitation instead of the sinusoidal excitation unless the frequency dependence of the materials is modeled.

4.5 Modeling base station antennas

Antenna structures consist of metal and possibly dielectric objects. The description of these can be found in Sections 2.3.1 and 2.3.3. Here, we assume the feed of the antennas are modeled as discrete sources, as described in Section 4.1.

Many base station antennas are array antennas[6] of several smaller array elements. The elements are similar in geometry, but their feeds may have different amplitudes and phases. A single element can be simple, because the radiating properties of the array are based more on the number, rather than the properties, of the elements.

[6]Not in the theoretical sense, because the array elements interact with each other.

The FDTD modeling of two common element antenna types, dipole and slot antennas, is described here. The whole base station antenna can be then modeled by replicating these and adding PEC reflector plates or other objects.

The total radiated power P_{rad} of an antenna with N discrete sources is given by

$$P_{\text{rad}} = \sum_{k=1}^{N} P_{k,\text{net}}, \tag{106}$$

where $\{P_{k,\text{net}}\}$ are the net input powers (96) of the sources. The amplitude distribution of an array antenna is the distribution of the square roots of the net input powers.

The SAR results are often normalized with respect to the total radiated power P_{rad}. The term "radiated power" is a little misleading, as this power includes the power which is absorbed in lossy materials (tissues), as well as *the* radiated power which actually is radiated away (absorbed in absorbing boundaries).

Directivity is a commonly used antenna parameter, which measures the antenna's ability to radiate power in a given direction. Directivity D in the direction $\mathbf{u}_r$ is defined as

$$D(\mathbf{u}_r) = \frac{W(\mathbf{u}_r)}{\frac{1}{4\pi} P_{\text{rad}}}, \tag{107}$$

where W is the radiated power per solid angle in the given direction, and 4π is the total solid angle. The radiated power per solid angle W can be calculated by performing a near-to-far-field transformation, see e.g. [1].

"Directivity" often means the maximum directivity

$$D_{\max} = \max_{\mathbf{u}_r} D(\mathbf{u}_r).$$

In this work, we assume a following definition for the *main lobe direction* of the antenna: A main lobe direction is a direction in which the directivity has a global maximum. This needs not be unique, but with practical base station antennas it is. Exceptions are the so-called omnidirectional antennas.

Far from the antenna, the radiated field of the antenna can be approximated by a spherical wave. The directivity is linked to the power density S (102) of the spherical wave by

$$S(\mathbf{r}) = D(\mathbf{u}_r) \frac{P_{\text{rad}}}{4\pi r^2}, \quad r \text{ large}. \tag{108}$$

Table 3 shows the wavelength in free space at the frequencies commonly used in mobile communications. The $\lambda/10$ rule requires resolutions finer than 14 mm, which is easily satisfied. All practical resolutions for the human body modeling, which are finer than 4 mm, should be sufficient for modeling antennas.

Naturally, finer details than the resolution cannot be modeled, but that is usually not necessary. Safety assessment of typical, generic base station antennas is often the main interest, so the fine geometric details of specific antennas do not matter.

Table 3: Wavelength in air

Frequency	Wavelength
900 MHz	33.3 cm
1800 MHz	16.7 cm
2140 MHz	14.0 cm

4.5.1 Antenna elements

A dipole antenna consists of two thin cylindrical conductors, in between which is the antenna feed. A sketch of a dipole antenna is shown in Figure 12.

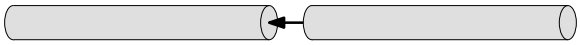

Figure 12: A sketch of a cylindrical dipole antenna

Figure 13 illustrates the FDTD implementation of the dipole using the staircase approximation. A discrete source (4.1) is placed at the center.

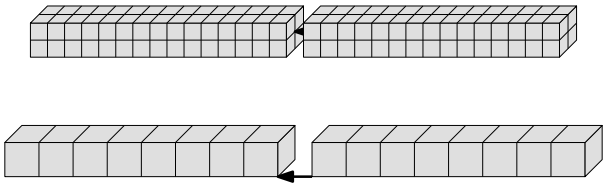

Figure 13: Staircase approximations of a dipole antenna

The most common dipole has a total length of half a wavelength. The directivity (maximum) of an ideal thin half-wavelength dipole is approximately $D = 1.64$, or 2.15 dB. There might be a reflector structure behind a dipole antenna, so that the dipole radiates in the desired direction, and thus the directivity is increased.

A dual case for the dipole antenna, a slot antenna, is a thin aperture on a metal surface. The radiating characteristics of a slot antenna closely resemble those of a dipole antenna of the same length. A sketch of a slot antenna is shown in Figure 14. The antenna is fed at the center of the slot. A slot antenna is seemingly easier to accurately implement in FDTD than the dipole antenna, because the slots are rectangular, and thus they fit into the FDTD lattice without changing their geometry.

4.5.2 Modeling the antenna feeds

It was assumed that the antenna feeds were simple discrete sources with inner resistances. In reality, the feeds would be more complex, which is illustrated in Figure 15. In the following, it is assumed that there is only a single discrete source per element, and sinusoidal excitation is used.

Most antennas are designed to work in environments where there are no objects in front of them hindering radiation. When a human body model is brought into

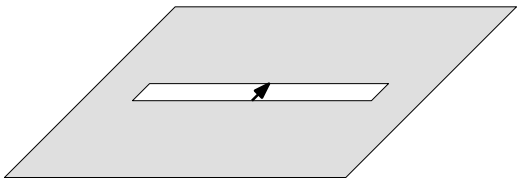

Figure 14: A sketch of a slot antenna

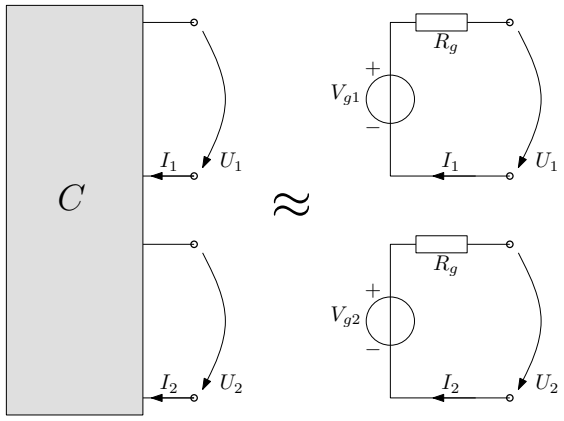

Figure 15: Modeling the feed of a two-element antenna; the voltage sources with inner resistances are an approximation of the circuit C.

the vicinity of an antenna, it is an unusual situation, and the antenna matching will change due to reflections. How much the matching will change, or how the change will affect SAR results, depends not only on the position of the body model, but also on the circuit model of the antenna. Regardless of the circuit model, the total radiated power is calculated using (106) and (96).

In the case of discrete sources, it feels natural that identical elements should have the same inner resistances R_g. Thus the possible amplitude (and phase) distribution should be taken into account in the voltage sources V_g. In free space, if there is little coupling between the elements, the amplitude of each source is directly proportional to the amplitude of the voltage source. If the net radiated powers (96) of the elements follow a given distribution in free space, the distribution of the net radiated powers will (generally) change in the vicinity of a human body model. How the final distribution will turn out depends on the values of R_g, or generally, the circuit model of the antenna.

In this work, most base station exposure results are given normalized with respect to a constant total radiated power P_{rad} (106). When examining these results, one should take into account that in reality the total radiated power will most likely be different at different body-antenna distances. If the antenna is matched to free space situation (as it should), the radiated power will become smaller near a body model. In such case, assuming the total radiated power to stay constant in all situations will very likely produce overestimation for the exposure. However, if the inner resistances of the sources are chosen incorrectly, the matching may actually become better near a human body model.

When a human body model is positioned near an antenna, the circuit model of the antenna does have an effect on the normalized (with respect to the total radiated power) SAR values (see the results in Section 6.4.4). Approximating the circuit model by simple discrete sources might cause some uncertainties in the results. Fortunately, the focus of the antenna modeling in this thesis is on the modeling of "typical" antennas, and the discrete source approximation is assumed to be sufficient. The choice of the inner resistances R_g is thus based on making an "educated guess", and hoping that the behavior of the antenna is somewhat realistic and fit for a typical antenna.

5 Specific absorption rate

Specific absorption rate (SAR) is the unit for energy absorption in human tissue. It has a dimension power per mass (W/kg). Local SAR is defined in [20] by

$$SAR = \frac{d}{dt}\left(\frac{dW}{dm}\right) = \frac{dP}{\rho dV} \tag{109}$$

which can be written in the form

$$SAR = \frac{s}{\rho}, \tag{110}$$

where s is the power loss density [W/m^3].

The power loss density s can be defined as

$$s(t) = \mathbf{J}(t) \cdot \mathbf{E}(t), \tag{111}$$

where $\mathbf{J}$ is the current density. If the fields are time harmonic with time-dependence $e^{j\omega_0 t}$, the rms-value (denoted without the time dependence) for the power loss density is

$$s = \frac{1}{2}\sigma|\mathbf{E}|^2, \tag{112}$$

where $\mathbf{E}$ (without the time dependence) is the amplitude of the electric field, and $\sigma = \sigma(\omega_0)$ is the conductivity. Pointwise SAR is thus relative to the square of the electric field amplitude by

$$SAR = \frac{1}{2}\frac{\sigma|\mathbf{E}|^2}{\rho}. \tag{113}$$

SAR is a power quantity, and in the case of base station antenna exposure, it is thus directly proportional to the total radiated power P_{rad} (106), which is the sum of the net input powers of all discrete sources of the antenna. In the plane wave case, SAR is directly proportional to the power density S of the plane wave. After calculating the SAR for one power, we thus get the SAR for an arbitrary power by just scaling, assuming the situation remains the same otherwise.

Additionally, assuming "ideal" nonthermodynamic circumstances [21], SAR is related to change of temperature at any point by formula

$$SAR = \frac{c\Delta T}{\Delta t} \tag{114}$$

where ΔT is the change of temperature [K] during an exposure of duration Δt [s] and c is the specific heat capacity of the tissue [Jkg^{-1}K^{-1}]. Generally, the actual heating caused by SAR is a separate, nontrivial problem.

5.1 Averaged SAR

Several international and European standards and recommendations limit the maximum local spatial-averaged SAR or the whole-body-averaged SAR. These include

the basic restriction limits by International Commission on Non-Ionizing Radiation Protection (ICNIRP, [22]) and Institute of Electrical and Electronic Engineers (IEEE, [20] and [21]). European Council recommendations [23] follow the ICNIRP guidelines [22].

The averaged SAR required by the limits can be calculated from the rms value of the local SAR (113). Averaging can be done in two ways, either by volume averaging, or by mass averaging. Volume averaging of SAR is done by

$$SAR_{\text{avg}} = \frac{\int_{\mathcal{V}} SAR dV'}{\int_{\mathcal{V}} dV'} = \frac{1}{V} \int_{\mathcal{V}} \frac{s}{\rho} dV', \tag{115}$$

where $\mathcal{V}$ is the averaging volume with volume V (this can be the whole body, for example).

Mass averaging is done by

$$SAR_{\text{avg}} = \frac{\int_{\mathcal{V}} s dV'}{\int_{\mathcal{V}} \rho dV'} = \frac{P}{m}, \tag{116}$$

where P is the total power absorbed in $\mathcal{V}$ and m is the total mass of $\mathcal{V}$. Notice that when the density ρ is constant, these two methods give the same results.

Both the standards by ICNIRP [22] and IEEE [21] require the volume-averaging method, if they are interpreted literally (e.g. [21]: "When averaging SAR over a 1 g volume of tissue..."). The averaging masses for spatial-averaged SAR are 10 g for [22] and [23], and 1 g (in the body) or 10 g (in the extremities) for [20].

According to [22], the averaging volume can be "any 10 g of contiguous tissue" with no defined shape, which leads to an infinite amount of possible averaging volumes. The SAR value used for exposure assessment should be the maximum of averaged SAR over these volumes. This kind of averaging is naturally extremely hard to implement in practical FDTD simulations. However, European Council [23] (provided the SAR values are conservative) and IEEE recommendations [21] allow cubical averaging volumes, which is easy to implement in FDTD grids. This approach is used in this study.

Despite that the standards can be interpreted to require the volume-averaging method (115), the mass-averaging method (116) will be used in this study. It is shown in [24] that the mass-averaging approach is a better representation of the effect of the fields on the tissue. This can be made clearer by simplified physical arguments: Average temperature in a volume is acquired by mass averaging; because the temperature rise is related to SAR by (114), mass averaging is the correct choice for the SAR.

The differences in the whole-body SAR calculated with the two averaging methods (mass/volume) are studied in Section 6.3.3.

5.2 Power loss density in FDTD

Determining the local power loss density from an FDTD solution can be trickier than one would think. In the following, all fields are amplitudes. In the case of

sinusoidal excitation, they can be extracted from the time-dependent values using (104).

From (112), the pointwise power loss density s in $\mathbf{r} \in \mathcal{D}$ can be written as

$$s(\mathbf{r}) = \frac{1}{2}\sigma(\mathbf{r})|\mathbf{E}(\mathbf{r})|^2 = \frac{1}{2}\sigma(\mathbf{r})\left(E_x(\mathbf{r})^2 + E_y(\mathbf{r})^2 + E_z(\mathbf{r})^2\right)$$

where the electric fields (without the time dependence) are amplitudes.

The total power loss density of a cell $\mathbf{p} \in \mathcal{I}_X$, $X \in \{E, H\}$ can be written as an integral

$$s(\mathbf{p}) = \frac{1}{2}\frac{\sigma(\mathbf{p})}{\mathrm{Vol}(\mathbf{p})}\int_{\mathcal{V}(\mathbf{p})} |\mathbf{E}|^2 dV' = \frac{1}{2}\frac{\sigma(\mathbf{p})}{\mathrm{Vol}(\mathbf{p})}\sum_{u=x,y,z}\left(\int_{\mathcal{V}(\mathbf{p})} E_u^2 dV'\right), \tag{117}$$

where $\mathbf{E}$ is the (continuous) electric field with components $\{E_u\}$, $\mathcal{V}(\mathbf{p}) \subset \mathcal{D}$ is the set

$$\mathcal{V}(\mathbf{p}) = [x(i-\frac{1}{2}), x(i+\frac{1}{2})] \times [y(j-\frac{1}{2}), y(j+\frac{1}{2})] \times [z(k-\frac{1}{2}), z(k+\frac{1}{2})], \tag{118}$$

where $\mathbf{p} = (i, j, k)$, and

$$\mathrm{Vol}(\mathbf{p}) = \int_{\mathcal{V}(\mathbf{p})} dV' = \Delta x(i)\Delta y(j)\Delta z(k). \tag{119}$$

There are several ways to approximate the integrals in the sum in (117). Here, we use the *trapezoid rule* and the *midpoint rule*. In one dimension, they can be written as follows. The trapezoid rule is

$$\frac{1}{\Delta}\int_0^\Delta f(x)dx = \frac{1}{2}\left(f(0) + f(\Delta)\right) + O(\Delta^2), \tag{120}$$

and the midpoint rule is

$$\frac{1}{\Delta}\int_0^\Delta f(x)dx = f\left(\frac{\Delta}{2}\right) + O(\Delta^2). \tag{121}$$

Both methods have an accuracy $O(\Delta^2)$, so, when the cell size Δ of the simulation is small enough, they will give similar results.

As discussed in Section 2.3.3, the material cells may be either E or H cells. In the E-cell case, we know twelve electric field tangential components on the cell edges, and in the case of H cells, we know six normal components on the cell sides. These situations are illustrated in Figures 16 and 17, respectively.

The E-cell case is illustrated in Figure 16. Assuming that the field components are constant in their parallel direction, using the trapezoid rule in two dimensions gives

$$\frac{1}{\mathrm{Vol}(\mathbf{p})}\int_{\mathcal{V}(\mathbf{p})} E_u^2 dV' \approx \frac{1}{4}\left(E_{u1}^2 + E_{u2}^2 + E_{u3}^2 + E_{u4}^2\right). \tag{122}$$

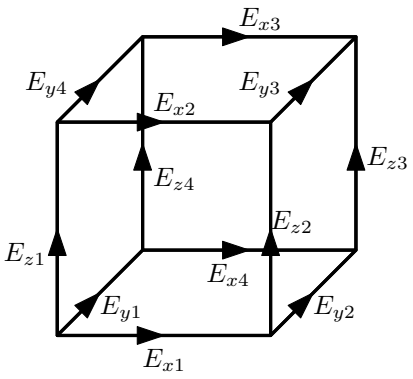

Figure 16: The locations of the electric field components in an E cell.

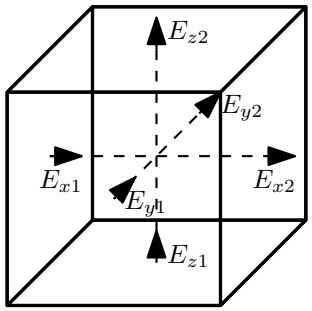

Figure 17: The locations of the electric field components in an H cell.

The power loss density is thus

$$s \approx \frac{\sigma}{8} \sum_{u=x,y,z} \left(E_{u1}^2 + E_{u2}^2 + E_{u3}^2 + E_{u4}^2 \right). \tag{123}$$

Utilizing the midpoint rule requires the value at the center point of the cell, but this is not readily available. If we assume the fields are linear (or bilinear) inside the cell, we may use a linear average of the fields on the cell edges/sides. In the E-cell case, if we assume the bilinearity of the electric field components, the midpoint rule gives:

$$s \approx \frac{\sigma}{32} \sum_{u=x,y,z} \left(E_{u1} + E_{u2} + E_{u3} + E_{u4} \right)^2. \tag{124}$$

If the materials are in H cells, we must take into account the effective nature of the electric field of the FDTD simulation, as discussed in Section 2.3.3. The physical electric field can be calculated from the FDTD electric field values using (40).

The H-cell situation is illustrated in Figure 17. If we assume the field is constant in transverse directions, the situation reduces to a one dimensional case, and the trapezoid rule gives

$$s \approx \frac{\sigma}{4} \sum_{u=x,y,z} \left((\frac{\epsilon_{u1}}{\epsilon} E_{u1})^2 + (\frac{\epsilon_{u2}}{\epsilon} E_{u2})^2 \right), \tag{125}$$

where $\{E_{u1}\}$ and $\{E_{u2}\}$ are the (effective) electric fields of the FDTD simulation, $\{\epsilon_{u1}\}$ and $\{\epsilon_{u2}\}$ are their respective effective permittivities, and ϵ is the permittivity of the cell.

Similarly, utilizing the midpoint rule and assuming linearity, we get

$$s \approx \frac{\sigma}{8} \sum_{u=x,y,z} \left(\frac{\epsilon_{u1}}{\epsilon} E_{u1} + \frac{\epsilon_{u2}}{\epsilon} E_{u2} \right)^2. \tag{126}$$

In the trapezoid case, the power loss density can thus be written (for both cell types) as

$$s = \frac{1}{2}\sigma(|\mathbf{E}|^2)_{\text{ave}} = \frac{1}{2}\sigma \sum_{u=x,y,z} (E_u^2)_{\text{ave}}, \tag{127}$$

where the subscript 'ave' means the linear average to the center point of the cell. In the H-cell case, this includes the transformation (40) from the effective electric field to the physical electric field.

The midpoint case can be summarized similarly

$$s = \frac{1}{2}\sigma|\mathbf{E}_{\text{ave}}|^2 = \frac{1}{2}\sigma \sum_{u=x,y,z} ((E_u)_{\text{ave}})^2. \tag{128}$$

The midpoint approach resembles the SAR calculation method presented in [25]. In the case of E cells, we take a linear average of the twelve electric field components on the cell edges, and take the square. This is exactly the same as the twelve-components approach in [25]. The H-cell case, in turn, resembles the six-components approach presented in that paper.

Of course, the above are based on the approximations of the integrals

$$\frac{1}{\text{Vol}(\mathbf{p})} \int_{\mathcal{V}(\mathbf{p})} E_u^2 dV'$$

in (117) by the two integration techniques. If the electric field is assumed to be (bi)linear inside the cell, this integral can also be calculated "accurately". In the E-cell case, such an integration gives, using the notation from Figure 16,

$$\frac{1}{\text{Vol}(\mathbf{p})} \int_{\mathcal{V}(\mathbf{p})} E_u^2 dV' = \frac{1}{18} \left(\begin{array}{l} 2E_{u1}^2 + 2E_{u2}^2 + 2E_{u3}^2 + 2E_{u4}^2 + 2E_{u1}E_{u2} + 2E_{u1}E_{u4} \ldots \\ +2E_{u2}E_{u3} + 2E_{u3}E_{u4} + E_{u1}E_{u3} + E_{u2}E_{u4} \end{array} \right). \tag{129}$$

Fortunately, this is approximately[7] the same as

$$\approx \frac{20}{27}((E_u)_{\text{ave}})^2 + \frac{7}{27}(E_u^2)_{\text{ave}}.$$

The H-cell case is simpler

$$\frac{1}{\text{Vol}(\mathbf{p})} \int_{\mathcal{V}(\mathbf{p})} E_u^2 dV' = \frac{1}{3}\left(\frac{\epsilon_{u1}}{\epsilon}E_{u1}\right)^2 + \frac{1}{3}\frac{\epsilon_{u1}}{\epsilon}E_{u1}\frac{\epsilon_{u2}}{\epsilon}E_{u2} + \frac{1}{3}\left(\frac{\epsilon_{u2}}{\epsilon}E_{u2}\right)^2, \tag{130}$$

[7] The cross terms are slightly different.

which equals

$$= \frac{2}{3}((E_u)_{\text{ave}})^2 + \frac{1}{3}(E_u^2)_{\text{ave}}.$$

So the "accurate" power loss density values can be received from the trapezoid and midpoint method values by simply taking a weighted average. Thus, only the trapezoid and midpoint methods are studied in this work.

In Section 6.3.1, several other methods for calculating the local power loss density will be presented. It will turn out that, for the E cells, the midpoint rule is the preferred method, and, for the H cells, the trapezoid rule is preferred. Thus, unless otherwise stated, the midpoint rule is used for the E cells (124), and the trapezoid rule for the H cells (125).

5.3 Calculation of averaged SAR in FDTD

In the discretized case, the total power loss over an arbitrary index set (volume) $\mathcal{V} \subset \mathcal{I}_X$, $X \in \{E, H\}$ is calculated

$$P(\mathcal{V}) = \sum_{\mathbf{p}\in\mathcal{V}} s(\mathbf{p})\text{Vol}(\mathbf{p}), \tag{131}$$

where s is the power loss density calculated as described in the previous section, and $\text{Vol}(\mathbf{p})$ is defined in (119). Applying (116) to the discretized case, the mass-averaged SAR is given by

$$SAR_{\text{avg}}(\mathcal{V}) = \frac{P(\mathcal{V})}{m(\mathcal{V})}, \tag{132}$$

where m is the mass of the averaging volume

$$m(\mathcal{V}) = \sum_{\mathbf{p}\in\mathcal{V}} \rho(\mathbf{p})\text{Vol}(\mathbf{p}). \tag{133}$$

The whole-body-averaged SAR is calculated using (132)

$$SAR_{\text{wb}} = SAR_{\text{avg}}(\mathcal{I}_{\text{body}}), \tag{134}$$

where $\mathcal{I}_{\text{body}} \subset \mathcal{I}_X$, $X \in \{E, H\}$, is the index set of the body.

Calculating the spatial-averaged SAR is a rather complex procedure. In this work, the spatial averaging is done by following the recommendations in IEEE Standard C95.3 [21] Annex E. Additionally, sizes of the averaging cubes are "fine tuned" using the methods presented in [25].

In the following, $\mathcal{I}_{\text{body}} \subset \mathcal{I}_E$ or $\mathcal{I}_H$ denotes the cells which contain tissue ($\rho > 0$). The voxels are assumed to be cubical so that $\Delta x = \Delta y = \Delta z$. The averaging mass (usually 10g or 1g) is denoted by m_{avg}.
For each cell $\mathbf{p} \in \mathcal{I}_{\text{body}}$

1. Build a sequence of cubes centered at $\mathbf{p}$, notated $\{\mathcal{C}_l(\mathbf{p})\}_l$, with sizes $(2l+1) \times (2l+1) \times (2l+1)$ voxels.

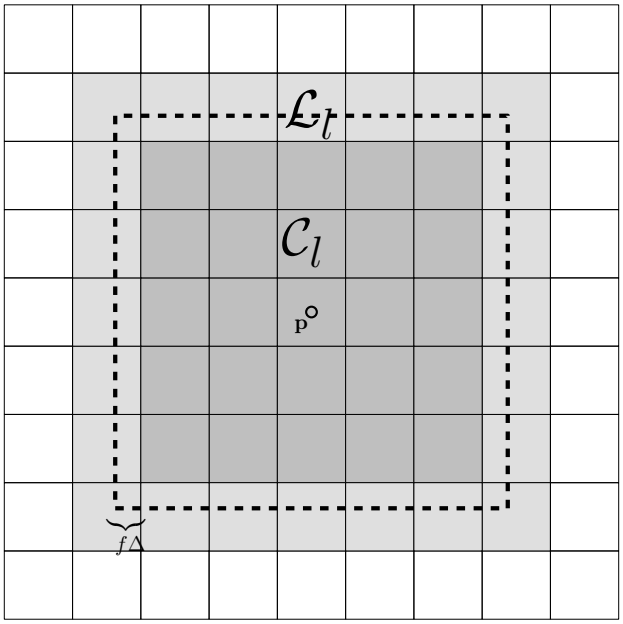

Figure 18: Determining the size of a SAR averaging cube in cell $\mathbf{p} \in \mathcal{I}_{\text{body}}$. The cube with the dashed contour should have a mass m_{avg}.

2. Search the largest l for which $m(\mathcal{C}_l) < m_{\text{avg}}$, thus $m(\mathcal{C}_{l+1}) \geq m_{\text{avg}}$.

   - If for any $n \in \{1, \ldots, l+1\}$, cube $\mathcal{C}_n$ has a face entirely in the air, mark the cell 'invalid', and take the next cell. Denote the index set of 'invalid' cells by $\mathcal{I}_{\text{invalid}} \subset \mathcal{I}_{\text{body}}$.
   - Otherwise, continue.

3. In order to get a cube with mass exactly m_{avg}, we need to add a fraction of the layer $\mathcal{L}_l = \mathcal{C}_{l+1} \backslash \mathcal{C}_l$, with a mass $m_{\text{avg}} - m(\mathcal{C}_l)$. The layer $\mathcal{L}_l$ has a mass $m(\mathcal{L}_l) = m(c_l) + m(e_l) + m(s_l)$, where c_l, e_l and s_l are the sets of 8 corners, 12 edges and 6 sides, respectively. We then get the required fraction $f \in (0, 1]$ by solving a cubical equation

$$m(c_l) f^3 + m(e_l) f^2 + m(s_l) f = m_{\text{avg}} - m(\mathcal{C}_l). \tag{135}$$

4. Now, calculate the mass-averaged SAR of the cell using (132)

$$SAR_{m_{\text{avg}}}(\mathbf{p}) = \frac{1}{m_{\text{avg}}} (P(\mathcal{C}_l) + f^3 P(c_l) + f^2 P(e_l) + f P(s_l)) \tag{136}$$

Next, define the SAR in the invalid cells $\mathcal{I}_{\text{invalid}}$.
For each invalid cell $\mathbf{p} \in \mathcal{I}_{\text{invalid}}$

1. Find the cells, the averaging cubes of which include the invalid cell $\mathbf{p}$. This neighborhood of the invalid cell is the index set

$$\mathcal{N}(\mathbf{p}) = \{\mathbf{q} \in \mathcal{I}_{\text{body}} \backslash \mathcal{I}_{\text{invalid}} : \mathbf{p} \in \mathcal{C}_{l+1}(\mathbf{q}),\ m(\mathcal{C}_l(\mathbf{q})) < m_{\text{avg}} \leq m(\mathcal{C}_{l+1}(\mathbf{q}))\}\,.$$

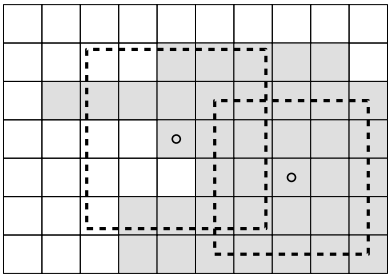

Figure 19: Examples of valid averaging cubes

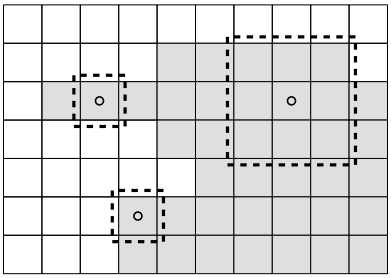

Figure 20: Some examples of invalid averaging cubes

2. If $\mathcal{N}(\mathbf{p}) = \emptyset$, i.e. the cell is not used in any valid averaging cube, mark the cell 'unused'. Denote the set of unused cells by $\mathcal{I}_{\text{unused}} \subset \mathcal{I}_{\text{invalid}}$. Otherwise, set

$$SAR_{m_{\text{avg}}}(\mathbf{p}) = \max_{\mathcal{N}(\mathbf{p})}\{SAR_{m_{\text{avg}}}\}.$$

SAR is now defined in all tissue cells, except in $\mathcal{I}_{\text{unused}}$. These cells are treated by the following:
For each unused cell $\mathbf{p} \in \mathcal{I}_{\text{unused}}$

1. Begin expanding six cubical volumes in six directions $(+x, -x, +y, -y, +z, -z)$, so that cell $\mathbf{p}$ is the center cell of one cube face. In building these cubes, follow the same kind of guidelines as presented above, but without the "face in the air"-criteria.

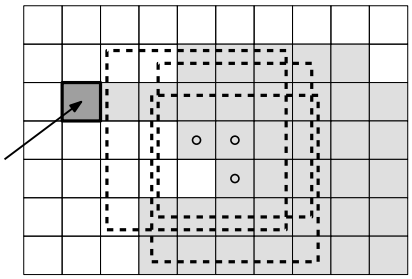

Figure 21: Example of an unused cell: The marked cell does not belong to any valid averaging cube

2. In the smallest of these cubes containing the desired mass, calculate the SAR using (132).

Now we have defined the spatial-averaged SAR for all cells $\mathbf{p} \in \mathcal{I}_{\text{body}}$. Notice that if we are only interested in the maximum value of mass-averaged SAR, we may omit the phase in which we determined $SAR_{m_{\text{avg}}}$ for the cells $\mathcal{I}_{\text{invalid}} \backslash \mathcal{I}_{\text{unused}}$.

5.4 Exposure recommendations and limits

ICNIRP [22] and IEEE [20] have issued basic restriction limits, below which there will be no adverse health effects.

At radio frequencies, the basic restrictions consist of limits for both whole-body and local spatial-averaged SAR, either of which must not be exceeded. The numerical values of the basic restriction limits are presented in Table 4. There are limits for both occupational and general public exposure, the latter of which includes children, sick and elderly and is thus more restrictive. The European Council recommendations [23] are the same as the ICNIRP limits for general public exposure.

Table 4: SAR basic restriction limits in the frequency range used by mobile communications

			Head/trunk		Limbs	
	Time of averaging [min]	Whole-body SAR [W/kg]	Averaging mass [g]	Localized SAR [W/kg]	Averaging mass [g]	Localized SAR [W/kg]
ICNIRP, General public	6	0.08	10	2	10	4
ICNIRP, Occupational	6	0.4	10	10	10	20
IEEE, General public	30	0.08	1	1.6	10	4
IEEE, Occupational	30	0.4	1	8	10	20

The magnitudes of the electromagnetic fields of an antenna decrease rapidly when the distance to the antenna increases. In the safety assessment of exposure to the fields of an antenna, it is thus useful to determine a volume around the antenna outside of which there is no risk of exceeding the basic restriction limits (Table 4). The boundary of such a volume is called the *compliance boundary*. In this work, we are mostly interested in the distance of the compliance boundary in the main lobe direction.

The *compliance distance* of an antenna is defined in the following way: it is the minimum distance of a human body from the antenna in the main lobe direction which guarantees the given restriction limits will not be exceeded. Naturally, the compliance distance depends on antenna input power. That is, larger input powers will produce shorter compliance distances, and vice versa.

6 Results

This section contains relevant numerical results related to the methods and models presented in the four preceding theory sections 2–5. This section is arranged so that each subsection is related to a corresponding theory section:

- Absorbing boundary conditions (Section 3): 6.1
- Results related to the accuracy of the FDTD method, material modeling and staircase approximation (Section 2): 6.2
- SAR calculation methods (Section 5): 6.3
- Modeling antennas and excitation signals (Section 4): 6.4
- Finally, SAR results involving realistic human body models (which are related to the all theory sections) are found in 6.5.

Calculations were performed with three different FDTD programs

- An own FDTD code written in Matlab using MEX functions, which allows quick and easy modifications for testing and validation purposes. This code was used in the "canonical" cases involving spheres and rectangles.
- A parallel-FDTD code written by Sami Ilvonen in the TKK Electromagnetics laboratory for the EMSOFT project. The code is written in Fortran95 and parallelized using MPI (Message passing interface) library, which allows solving of electrically huge problems in massively parallel supercomputers. This code is used for the results involving human body models. The principles, such as the FDTD update equations and CPML absorbing boundary conditions, were basically the same in this code and in the own code.
- *Microwave Studio*, a commercial software by CST. This program was used for antenna modeling and verification of the other codes. Unlike the other two codes (which use sinusoidal excitation and CPML), Microwave Studio uses pulse excitation and split-field PML. Strictly speaking, Microwave Studio does not use the FDTD method, but FIT (Finite integration technique) method, which is a close relative to FDTD.

6.1 Absorbing boundary conditions

Several recent papers have discussed the applicability of PML absorbing boundary conditions in FDTD SAR calculation. It was reported in [26] that uniaxial PML (UPML) absorbing boundary conditions may cause significant error in whole-body SAR values in a homogeneous muscle sphere. It was concluded that a thick free-space region between the numerical phantom and the UPML boundaries is required for accurate whole-body SAR results. In [27], Norman phantom and split-field PML was studied. There was little variation in whole-body-averaged SAR values when the distance between the voxel phantom and PML-ABC's was varied. Also, increasing the PML width above 6 cells was shown to have little effect on the SAR values.

In this work, convolutional PML absorbing boundary conditions (as described in Section 3) are employed for SAR calculation. The objective of this section is to verify the performance of CPML and also find good CPML parameters for SAR calculation.

The following method is utilized to test the performance of CPML:

- A phantom (sphere/box/human voxel model) is exposed to a plane wave. The incident wave is linearly polarized, with the polarization direction parallel to a coordinate axis.
- The distance from the phantom to CPML is varied, and SAR is calculated for each distance.
- If the ABC's were ideal, changing the distance would not affect the results. Thus, the smaller the variation in SAR, the better the ABC's.

The minimum possible phantom-CPML distance was 2 cells, as the total-field/scattered-field boundary was positioned one cell away from the CPML.

From a large number of various test simulations[8] the following parameters have proven to be effective:

- $\sigma_{\max} = \sigma_{\text{opt}}(m, \Delta)$ as in (89)
- $\kappa_{\max} = 5$ in (90)
- $a_{\max} = 0.05$ in (91)
- Polynomial grading of CPML parameters is used. Grading order is $m = 3$ for $\{\sigma_u\}$ and $\{\kappa_u\}$ in (88) and (90)
- The grading order $m_a = 1$ for $\{a_u\}$ in (91)

From now on, these are cited as the "good" CPML parameters. This good choice of parameters is verified in the following subsections. Further, unless otherwise stated, this set of parameters is used.

[8] The parameters $\sigma_{\max}$, $\kappa_{\max}$, $a_{\max}$, m, and m_a were swept, and the whole-body SAR in a small muscle sphere was calculated for ten sphere-CPML distances for each parameter combination.

6.1.1 Small muscle sphere

The studied situation consists of a 2/3-muscle sphere, with a radius of 2.5 cm, in free space, exposed to a plane wave with amplitude 1 V/m. The material parameters of the sphere can be found in Table 5. The mesh resolution is 2 mm, and the investigated frequencies are 1 GHz and 2 GHz.

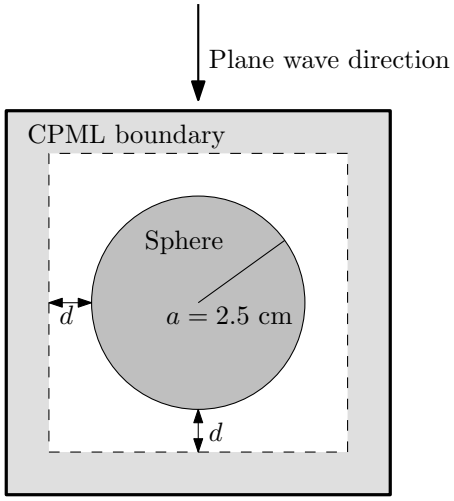

Figure 22: The CPML test setup for a small muscle sphere. The distance to the CPML boundary is d.

Table 5: Material parameters of the muscle sphere

Frequency	σ [S/m]	ϵ_r	ρ [kg/m^3]
1 GHz	0.65	36.5	1000
2 GHz	1.00	37.3	1000

Figures 23 and 24 show the relative error of whole-body-averaged SAR as a function of the distance from the CPML for four different parameter sets, at the investigated frequencies. The error is calculated relative to the situation where the CPML is thick and is located far (> 100 cells) from the sphere[9].

When the CFS functionality is disabled ($a = 0$, $\kappa = 1$), the error increases when the sphere-CPML distance decreases. This does not happen when the CFS is enabled ($a > 0$, $\kappa > 1$). Also, as can be seen in the figures, increasing the width of the CPML by just one layer reduces the error significantly. The variation of local SAR (not in the figures) followed the variation of whole-body SAR closely. The error seems to vary somewhat sinusoidally with the distance from the CPML, similarly to [26], but the error is much smaller.

The width of the CPML was relatively small in the above calculations, and it could be easily increased, which would make the error even smaller. It is quite

[9]The error is positive if the calculated SAR_{wb} is greater than the $SAR_{\mathrm{wb,far}}$. Otherwise, it is negative.

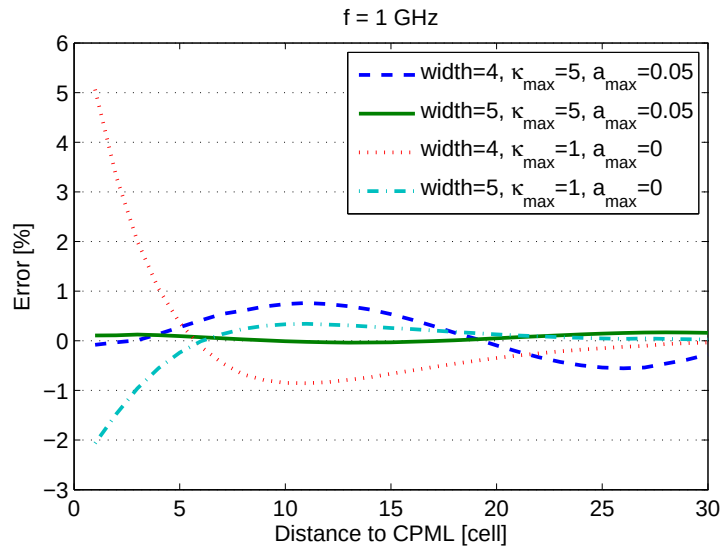

Figure 23: The relative error of whole-body-averaged SAR in a small muscle sphere at 1 GHz

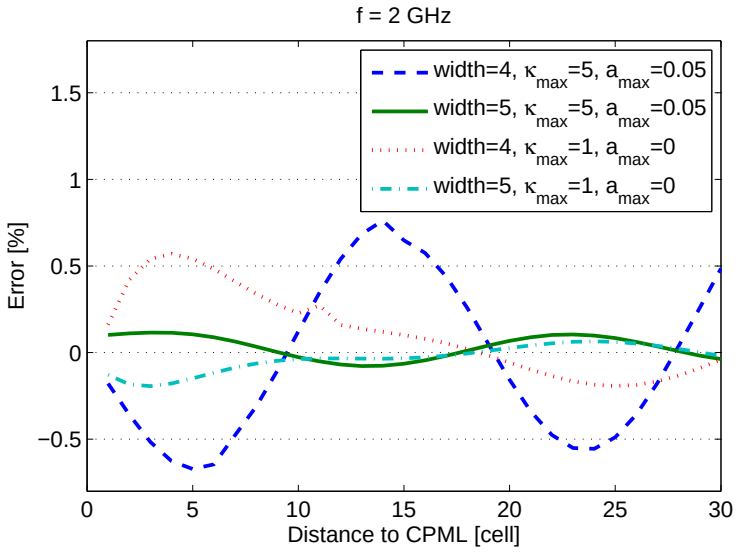

Figure 24: The relative error of whole-body-averaged SAR in a small muscle sphere at 2 GHz

obvious from the results that, when the CPML parameters are chosen correctly, the error caused by the ABC's is small. In many practical calculations, 4 or 5 cell thick CPML is sufficient.

As can be seen in Figure 23, the error caused by low-performance PML may cause both over- or underestimation in the evaluation of the whole-body SAR.

6.1.2 Box phantom

The performance of the CPML was further tested using a rectangular box phantom and various mesh resolutions. This time, the width of the CPML is 6 cells, the "good" CPML parameters were used, and the resolutions are 1 mm, 2 mm and 3 mm. The box dimensions are 6 cm × 12 cm × 12 cm, that is 60 × 120 × 120 cells when the resolution is 1 mm. The material of the box is 2/3 muscle, the details of which can be found in Table 5. The propagating direction of the incident plane wave is parallel to the short axis of the box, and the frequency is 2 GHz.

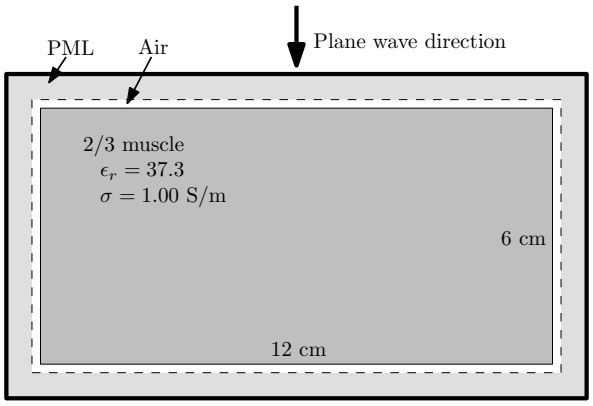

Figure 25: The CPML test setup for a muscle box.

The situation with the 1 mm resolution is illustrated in Figure 25. As can be seen in the figure, when the CPML-box distance is 2 cells, the box fills the calculation domain almost entirely. Still, as the results below show, the situation looks like the box was positioned in free space.

The difference in the maximum pointwise SAR as a function of the distance to CPML is shown in Figure 26. The difference is calculated relative to the furthest-distance SAR_{max} value (for each resolution separately). From the figure, it seems that the CPML performs "perfectly" with the 2 mm and 3 mm resolutions. With the 1 mm resolution, however, the performance is not as good. This happens because the CPML parameters are dependent on the mesh resolution, and apparently the parameters perform better with the lower resolutions. Additionally, the CPML-box distance is greater (in units of length) for the lower resolutions, but this cannot fully explain the poorer performance with the high resolution. On the other hand, the SAR_{max} calculated with the 1 mm resolution is ≈3.5 % and ≈8.8 % higher than the 2 mm and 3 mm resolution SAR_{max}, respectively. Compared to the error shown in the figure, this is much larger.

The difference in whole-body-averaged SAR was smaller than the difference in SAR_{max}; between the closest- and furthest-distance SAR_{wb}-values, it was less than 0.25% for the 1 mm resolution, and nonexistent for the other resolutions. The SAR_{wb} value calculated with the 1 mm resolution was ≈3.0 % and ≈8.7 % higher than with the 2 mm and 3 mm resolutions, respectively.

These results further verify the choice of "good" CPML parameters for SAR

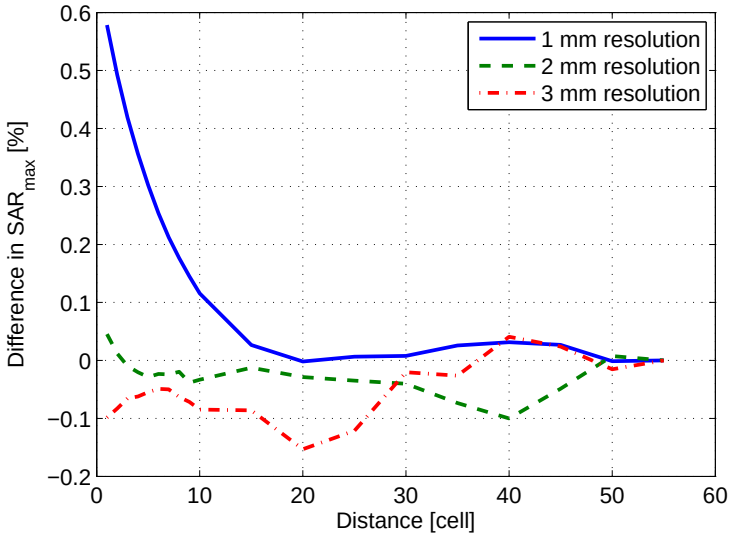

Figure 26: Difference in maximum pointwise SAR as a function of distance to CPML in the muscle box illustrated in Figure 25.

calculation. Even though the error became larger for small CPML-box distances with the 1 mm resolution, it was still extremely small.

6.1.3 Norman voxel phantom

Some test were carried out with the Norman phantom to verify the results presented in [27]. The resolution is 2 mm × 2 mm × 2 mm[10], and the width of the CPML is 6 cells. The frequency and power density of the incident vertically polarized plane wave are 2140 MHz and 1 W/m^2, respectively.

The results are presented in Tables 6 and 7. The variation in both the whole-body and the 10 g spatial-averaged SAR are very small. The nonperfect (see Section 6.1.1) CPML parameters give as accurate results as the "good" parameters. As said, the nonperfect parameters used here correspond to the standard split-field PML. These results are in line with [27].

Table 6: Whole-body-averaged SAR in Norman phantom for various CPML-phantom distances.

Distance	$a = 0.05$, $\kappa = 5$		$a = 0.00$, $\kappa = 1$	
[cell]	SAR_{wb} [mW/kg]	%	SAR_{wb} [mW/kg]	%
3	6.5041	99.99	6.5016	99.95
9	6.5015	99.95	6.5006	99.94
15	6.4972	99.89	6.4969	99.88
21	6.5047	100.00	6.5047	100.00

[10]In other simulations involving Norman, the resolution was 2.022 mm

Table 7: The maximum 10g-averaged SAR in Norman phantom for various CPML-phantom distances.

Distance	$a = 0.05$, $\kappa = 5$		$a = 0.00$, $\kappa = 1$	
[cell]	SAR_{10g} [mW/kg]	%	SAR_{10g} [mW/kg]	%
3	99.158	99.95	99.704	100.23
9	99.119	99.91	99.537	100.06
15	99.049	99.84	99.378	99.91
21	99.212	100.00	99.472	100.00

The conclusion of this section is that the error on the SAR results due to a properly implemented CPML absorbing boundary is very small. This error may be made even smaller by increasing the thickness of the CPML layer or tuning the CPML parameters. Additionally, it seems that the SAR values in human body models such as Norman are quite robust in the sense that using nonperfect CPML parameters does not change the results much.

6.2 Effects of material cells and staircase approximation

The discretization error (26), the size of which is affected by the choice of the material cell type (2.3.3), and the consistency error due to the staircase approximation (2.3.4) both have some effects on the results of a FDTD simulation. In this section, their effects on the SAR values in spheres are studied.

One important benefit of using spheres is that there is an analytical solution, the Mie theory solution, which can be used as a reference for the FDTD results. Thus, sphere simulations are often used in verification and testing of FDTD codes. The results in this section will help analyze several important factors affecting the accuracy of such tests.

Also, a small object in free space might not always be completely unrealistic. The material contrasts inside a human body may be as big as the contrast between air and a 2/3-muscle sphere. For example, at 1800 MHz, the permittivity and conductivity of the fat tissue are approximately $\epsilon_r = 5.3$ and $\sigma = 0.078$ S/m. On the other hand, the material parameters of muscle are approximately $\epsilon_r = 53.5$ and $\sigma = 1.34$ S/m, which is quite a contrast. And there are a lot of small (somewhat sphere-like) details which involve these materials in a human body.

The following methods are used in all the simulations of this section

- The situation consists of a homogeneous 2/3-muscle sphere in free space.
- The studied frequencies are 1 GHz and 2 GHz.
- The sphere is exposed to a sinusoidally excited linearly polarized plane wave with an amplitude (peak) of 1 V/m.
- The material parameters of the sphere at the studied frequencies can be found in Table 5. The density was assumed to be constant 1000 kg/m^3.
- The staircase approximation of the spheres is done as described in Section 2.3.4.
- Six cell thick CPML absorbing boundaries with the "good" CPML parameters, as described in Section 3 and 6.1, are used. The sphere-CPML distance is $\approx$ 3 cells.
- SAR calculation is done using the methods presented in Section 5. The mid-point rule is used for the E cells, and the trapezoid rule for the H cells.

The simulation setup is shown in Figure 27.

6.2.1 Effects of the material cell type on SAR

The effects of the material cell types and the staircase approximation on whole-body SAR were studied by staircase approximating muscle spheres of varying radii with a constant 2 mm mesh resolution. The error due to the staircasing should be larger for small spheres and smaller for large spheres. The Mie-theory solutions are used

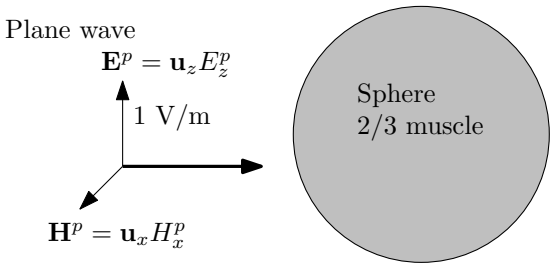

Figure 27: The simulation setup

as a reference. The simulations were done for the both material cell types: E and H cells.

Whole-body SAR in the sphere at 1 GHz is plotted as a function of the sphere radius in Figure 28. The hypothesis that increasing the ball size would reduce the difference to the Mie-theory solutions seems not to be quite correct: at certain ball sizes the error becomes larger with a certain cell type, while smaller radii may give more accurate results.

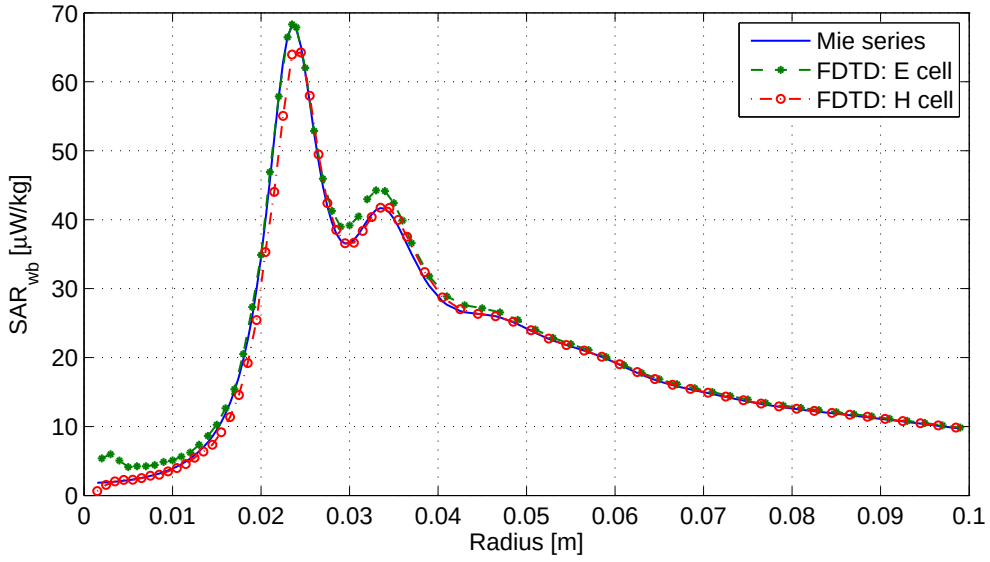

Figure 28: Whole-body SAR in a muscle sphere as a function of sphere radius at 1 GHz. The simulation setup is shown in Figure 27.

The two visible peaks in SAR correspond to the lowest TE^r and TM^r resonances of the sphere (see e.g. [28]). At these resonances, the radial component of either electric (TE^r) or magnetic (TM^r) field is zero.

Near the TE^r-resonance radius, the H-cell approach fails to give accurate results, whereas the E cells give an almost perfect match with the Mie-theory solution. On the contrary, the E cells fail near the TM^r resonance, and the H cells give very accurate results. For very small radii, the H cells seem to give quite good results, whereas the E-cell approach seems broken.

The second lowest TE^r resonance happens at $a \approx 4.9$ cm, and the TM^r at $a \approx 6.0$ cm. These are also visible in the figure, but there does not seem to be such a clear difference between the two material cell approaches.

The sphere radius looks slightly too large for the H cells: If we shift the H-cell curve 0.35 mm to the left, we get a better match with the Mie-theory solutions. However, this is not enough to explain the different magnitudes of SAR at the "resonant radii".

The situation is basically the same in the higher frequency case. This is seen in Figure 29, which shows the same curve as in Figure 28 at 2 GHz. The shape of the curve is the same as in the 1 GHz case, but the resonant radii are approximately halved. Again, the H-cell curve is shifted approximately 0.35 mm to the right.

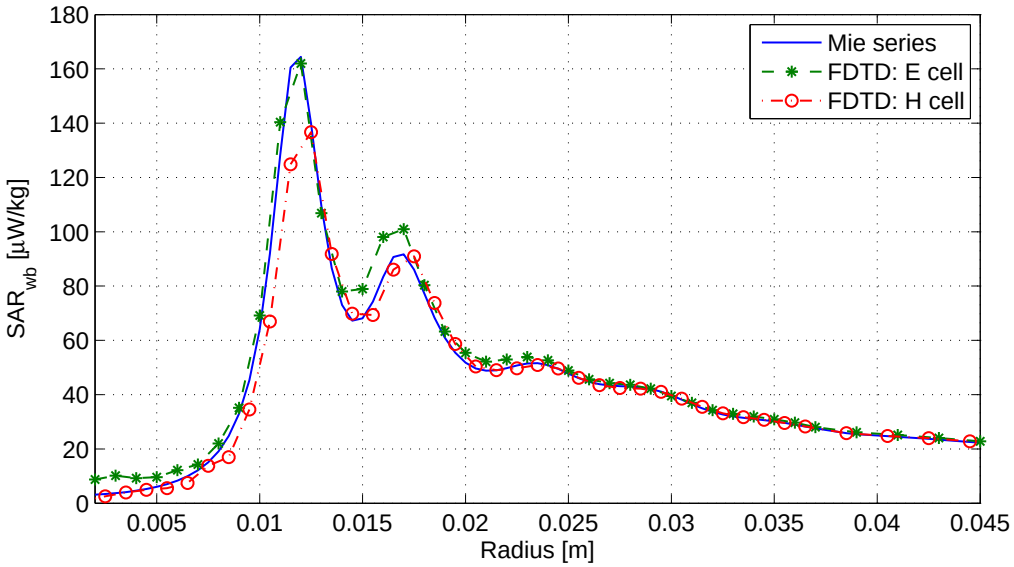

Figure 29: Whole-body SAR in a muscle sphere as a function of sphere radius at 2 GHz.

Based on these results only, it is hard to say which part of the error is due to the staircase approximation and which is due to the other factors, like the choice of the material cell. However, it seems the differences due to the different material cells are more significant than the error due to staircasing.

6.2.2 Error estimate of the staircase approximation

The staircasing algorithm presented in Section 2.3.4 produces slightly different spheres, depending on the location of the midpoint of the sphere in the FDTD grid. Figure 30 shows an example of this. In the figure, the midpoint of a sphere is slightly shifted from one location to another, which produces two clearly different staircase approximations of the same sphere.

Here, we will employ the following two options for the staircasing:

Corner: the midpoint of the sphere is located in a corner of a cell ("corner-centered").

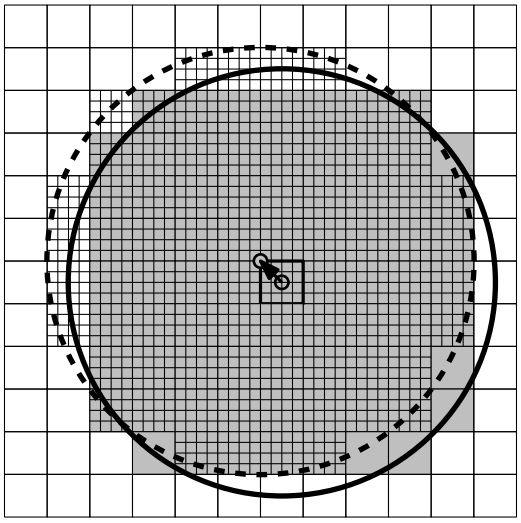

Figure 30: Alternative staircasings of a sphere. The sphere with the solid contour: grey. The sphere with the dashed contour: dense grid.

Center: the midpoint of the sphere is the center point of a cell ("center-centered").

If we compare the SAR_{wb} results in the same sphere staircased with the two different methods, we get a rough estimate of the magnitude of the error due to the staircase approximation:

$$\text{error} \approx 2 \max_{E,H} \left| \frac{SAR_{\mathrm{wb}}^{\mathrm{corner}} - SAR_{\mathrm{wb}}^{\mathrm{center}}}{SAR_{\mathrm{wb}}^{\mathrm{corner}} + SAR_{\mathrm{wb}}^{\mathrm{center}}} \right|, \tag{137}$$

where the maximum is taken over the two cell types. This formula will give quite reasonable values, as will be seen in the results. For an accurate staircase error, we would need to take the maximum difference in SAR values over all possible staircasings of the sphere.

In Figures 28 and 29 in the previous section, the location of the midpoint of the sphere was not constant. Instead, every second sphere was corner-centered, and every other center-centered. There seems to be no clear "zigzagging", so the difference between the two options apparently is not very large. Figure 31 shows the staircase error estimate (137) for the 1 GHz case in Figure 28. Clearly, the radius of the sphere has a large impact on the staircase error. It seems that a radius larger than 2.8 cm (14 cells) is almost (exclude the peak at $a = 3.7$ cm) sufficient to guarantee that the estimated staircase approximation error is smaller than 1 %.

There are several peaks and dips within the interval [2.0 cm , 4.0 cm] in the curve. The dips correspond to the local minima or maxima in Figure 28, and the peaks seem to correspond to the radii where the rate of change of SAR_{wb} is large. Thus the staircase error seems to be proportional to the derivate of SAR_{wb}. This observation feels quite natural: When the derivate is large, a small change in the sphere shape or size, which happens in the staircasing process, may cause a larger change in SAR_{wb}. And when the derivate is close to zero, a small change in radius will only cause small change in SAR_{wb}.

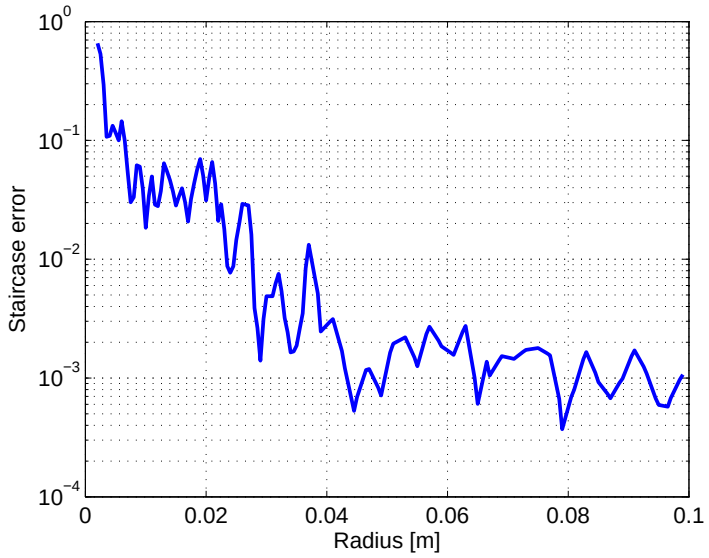

Figure 31: Estimate of the staircase approximation error. Small muscle spheres of varying radii are exposed to a plane wave at frequency 1 GHz. Mesh resolution is constant 2 mm.

In the next section, the estimates of staircase approximation errors are included in Tables 8–12 for different radii and various mesh resolutions. The SAR values in the tables are calculated with center-centered spheres.

6.2.3 Convergence test for small spheres

Looking at the Figures 28 and 29, one can find several interesting radii. For example, the following (frequency 1 GHz):

$a = 0.65$ cm, very small sphere: For very small spheres, the H cells seem to give fairly good results — taking into account how nonspherical the sphere actually is due to the staircasing. E cells, however, do not give reasonable results.

$a = 2.35$ cm, TE resonance: At this radius, the E-cell approach gives very accurate results, while the H-cell approach produces large error.

$a = 2.50$ cm, between the resonances: At this radius, the both cell types seem to give highly accurate results.

$a = 3.35$ cm, TM resonance: The dual case for the TE resonance.

$a = 2.50$ cm, after the resonances (frequency 2 GHz): After the two first resonance peaks, the E- and H-cell solutions begin to converge to the same solution when the radius becomes larger. Both methods seem to give quite accurate SAR values.

These cases are studied further by gradually increasing the resolution of the FDTD mesh in each of these cases. That should reduce the error due to the staircase approximation and discretization, and the results should converge to the Mie-theory solutions. The staircasing of the spheres was done using the center option, as described in the previous section.

The simulation results are presented in Tables 8–12. A more illustrative representation of the tables is shown in Section 6.3.1 in Figures 34–38. Several observations can be made based on the tables:

$a = 0.65$ cm, very small sphere: results are presented in Table 8. In this case, the E cells have poor accuracy for all resolutions. The H-cell SAR values are much better in line with the Mie theory, but they are not quite as accurate as the results of the other situations presented here.

At the lower mesh resolutions, a large part of this error is due to the staircase approximation, as the estimate for the staircase approximation error shows. For example, with the 4 mm resolution, the studied object hardly resembles a sphere. However, all of the error cannot be explained by the error due to the staircasing; the 0.5 mm and 0.25 mm resolutions should be sufficient for the staircase approximation. Still, the error with the E cells is more than 8 % at 0.25 mm.

$a = 2.35$ cm, TE resonance: Table 9. E-cell approach gives accurate SAR even at low resolution, and changing the resolution has little effect on SAR. In turn, H cells produce large error with the coarser resolutions, and increasing the resolution causes the H-cell results to slowly converge towards the Mie-theory result.

The staircase-error estimate seems to be relatively small, which implies that the difference in E- and H-cell results can not be fully explained by the staircase error.

This seems like the best case for the E cells, and at the same time, the worst case for the H cells.

$a = 2.50$ cm, between the resonances: Table 10. In this case, both cell types give quite accurate results. Only the 4 mm resolution seems insufficient. H-cell solution is slightly closer to the Mie theory than the E-cell solution.

It seems that the results of the both cell types converge to the same value, but this value seems to be very slightly (≈ 0.4 %) larger than the Mie-theory SAR.

The staircase-error estimate is larger than in the other cases (excluding the very small sphere case) presented here. Apparently, this has to do with the derivate of the whole-body SAR in Figure 28, which is large at radius $a = 2.50$.

$a = 3.35$ cm, TM resonance: Table 11. This case is very similar to the TE case. This is the worst case for the E cells (excluding the very small sphere case), and the best case for the H cells.

The staircase error is small for all the resolutions, because the sphere is relatively large, and the radius is near a local maximum of SAR, so the derivate of the SAR is near zero.

$a = 2.50$ cm, after the resonances (frequency 2 GHz): Table 12. With the higher frequency, the 4 mm resolution does not satisfy the "$\lambda/10$" criterion for the smallest mesh step. Thus, the SAR result is not very accurate with that resolution. Otherwise, both cell types give fairly accurate results, the H-cell solution being slightly closer to the Mie theory.

The staircase error is approximately only half of the error of the 1 GHz case. This might be due to the smaller derivate of the SAR.

Clearly, all the presented results seem to converge towards the Mie-theory reusult with the resolution. The material cell type, be it E cells or H cells, may have a large effect on the accuracy and the convergence speed, depending on the radius of the sphere. Both material cell approaches converge to the same solution when the resolution is increased. However, the convergence speed and the direction of convergence are different. For example, at the resonant radii, the convergence of one cell type solution is immediate, whereas the solution of the other cell type converges slowly.

This seems to implicate that the difference between the E-cell and H-cell values could be used as an error estimate for the SAR. In all results presented in this and in Section 6.2.5, excluding the 2.5 cm radius sphere with the 4 mm resolution, the difference between the E- and H-cell SAR values was a decreasing function of the resolution. An observation can be made based on the results: the smaller the difference between the two solutions, the more accurate the solution.

In the "good" cases presented here, changing the resolution had little effect on the whole-body SAR. On the other hand, in the "bad" cases, the resolution had a major impact on the SAR results. This implies: if the SAR results stay the same when the resolution is increased, they are accurate. This conclusion is quite natural when taking into account the estimate for the discretization error (26).

In most cases presented here, the E-cell solution approached the Mie theory from above, and the H-cell solution from below. This is not generally true, and both the E and H cells may produce either over- or underestimation for the SAR.

A radius of 13 cells produced a staircase error less than 1 % in all five cases presented here. This is in line with the estimate of 14 cells, which was based on Figure 31. Also, the observation that the staircase error is proportional to the derivate of the SAR_{wb} seems to hold.

In most cases, the material cell type seemed to have a bigger impact on the SAR values than the staircase approximation. Thus it is quite clear that the differences in the whole-body SAR values between the two material cell types cannot be explained by the staircase error.

Table 8: SAR in the muscle sphere. Very small sphere: $a = 0.65$ cm. The plot of these values is included in Figure 34.

	E cell		H cell		Staircase
Resolution	SAR_{wb} [μW/kg]	% Mie	SAR_{wb} [μW/kg]	% Mie	error [%]
4 mm	5.7084	224.57	1.6667	65.57	38.42
2 mm	4.2394	166.78	2.5222	99.23	11.65
1 mm	3.3194	130.59	2.5854	101.71	2.23
0.5 mm	2.9552	116.26	2.5974	102.18	0.39
0.25 mm	2.7525	108.29	2.5833	101.63	0.14
Mie-series	2.5419				

Table 9: SAR in the muscle sphere. The TE-resonance case: $a = 2.35$ cm. The plot of these values is included in Figure 35.

	E cell		H cell		Staircase
Resolution	SAR_{wb} [μW/kg]	% Mie	SAR_{wb} [μW/kg]	% Mie	error [%]
4 mm	67.310	98.78	55.862	81.98	4.69
2 mm	68.020	99.82	63.526	93.23	0.66
1 mm	68.040	99.85	65.959	96.80	0.12
0.5 mm	68.037	99.85	67.038	98.38	0.03
Mie-series	68.141				

Table 10: SAR in the muscle sphere. Between the resonances: $a = 2.50$ cm. The plot of these values is included in Figure 36.

	E cell		H cell		Staircase
Resolution	SAR_{wb} [μW/kg]	% Mie	SAR_{wb} [μW/kg]	% Mie	error [%]
4 mm	60.030	97.75	58.790	95.74	4.83
2 mm	62.600	101.94	61.938	100.86	0.94
1 mm	61.638	100.37	61.521	100.18	0.93
0.5 mm	61.667	100.42	61.628	100.36	0.15
Mie-series	61.409				

Table 11: SAR in the muscle sphere. The TM-resonance case: $a = 3.35$ cm. The plot of these values is included in Figure 37.

	E cell		H cell		Staircase
Resolution	SAR_{wb} [μW/kg]	% Mie	SAR_{wb} [μW/kg]	% Mie	error [%]
4 mm	46.288	111.04	41.308	99.09	0.90
2 mm	44.445	106.62	41.760	100.18	0.09
1 mm	43.076	103.33	41.721	100.08	0.20
0.5 mm	42.365	101.63	41.723	100.09	0.01
Mie-series	41.687				

Table 12: SAR in the muscle sphere. Frequency 2 GHz, $a = 2.5$ cm. The plot of these values is included in Figure 38.

	E cell		H cell		Staircase
Resolution	SAR_{wb} [μW/kg]	% Mie	SAR_{wb} [μW/kg]	% Mie	error [%]
4 mm	45.741	95.77	45.511	95.29	3.57
2 mm	49.168	102.94	48.053	100.61	0.56
1 mm	48.625	101.81	47.872	100.23	0.52
0.5 mm	48.285	101.09	47.857	100.20	0.09
Mie-series	47.762				

6.2.4 Convergence test for large spheres

This section is a continuation of the previous section, which studied the effects of resolution in small spheres. Here, the sphere radius $a = 10.00$ cm, which corresponds to a head size, and this situation seems thus somewhat more "realistic". However, a large homogeneous object such as this might not necessarily be any more realistic than a smaller sphere with a high contrast to the surrounding background material — human head is hardly homogeneous, but there are plenty of small high-contrast details in a human body.

The SAR in the sphere was studied for two frequencies: 1 GHz and 2 GHz. All assumptions are similar to the previous sections. The results are presented in Tables 13 and 14 for the 1 GHz and 2 GHz cases, respectively.

It seems clear that for large spheres, the staircase error estimate is small even at coarse resolutions. In both cases, the H cells seemed to give slightly more accurate results than the E cells, but this might be coincidence.

Unsurprisingly, the 8 mm resolution results at 2 GHz are very inaccurate, which is due to the fact that the 8 mm resolution corresponds to approximately 3.4 cells per wavelength. It seems that 4 mm is a sufficient resolution at 1 GHz, and 2 mm is sufficient when the frequency is 2 GHz, as both cell types give accurate results at these resolutions. At coarser resolutions, such as 8 mm resolution when the frequency is 1 GHz, and 4 mm resolution when the frequency is 2 GHz, H cells seem to give quite accurate results, unlike the E cells. This is likely only coincidence.

Table 13: SAR in the muscle sphere at 1 GHz. A "head-sized" sphere: $a = 10.0$ cm. The plot of these values is included in Figure 39.

	E cell		H cell		Staircase
Resolution	SAR_{wb} [μW/kg]	% Mie	SAR_{wb} [μW/kg]	% Mie	error [%]
8 mm	9.0631	94.81	9.4713	99.08	0.36
4 mm	9.6782	101.25	9.6292	100.73	0.47
2 mm	9.6928	101.40	9.6140	100.57	0.10
1 mm	9.6418	100.86	9.5897	100.32	0.02
Mie-series	9.5592				

Table 14: SAR in the muscle sphere at 2 GHz. A "head-sized" sphere: $a = 10.0$ cm. The plot of these values is included in Figure 40.

	E cell		H cell		Staircase
Resolution	SAR_{wb} [μW/kg]	% Mie	SAR_{wb} [μW/kg]	% Mie	error [%]
8 mm	4.0822	52.31	6.7449	86.42	1.76
4 mm	7.3310	93.93	7.8869	101.06	0.05
2 mm	7.8454	100.52	7.9028	101.26	0.02
1 mm	7.8831	101.01	7.8676	100.81	0.01
Mie-series	7.8045				

6.2.5 Muscle piece

The effects of mesh resolution were tested in the previous sections for spheres, the results of which verified the convergence to Mie-theory solutions. However, those simulations also included the error due to the staircasing in addition to the discretization error due to the mesh resolution. In this section, the effects of mesh resolution on SAR are studied further by exposing a rectangular muscle object, the geometry of which is independent of the resolution, to a plane wave.

The muscle piece illustrated in Figure 32 was exposed to a linearly polarized plane wave. The frequency and amplitude of the plane wave were 2 GHz and 1 V/m, and the direction of propagation was perpendicular to the skin. SAR was calculated for several mesh resolutions. The dimensions of the object were chosen in such a way that the resolution did not have any effect on the geometry.

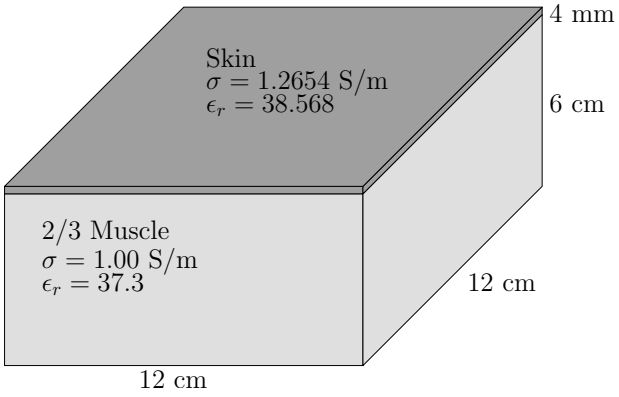

Figure 32: Muscle piece

Figure 33 shows the calculated power loss density in the E-cell case on a line parallel to the short axis of the piece, positioned in the middle of the piece. The 4 mm resolution is clearly insufficient, and the results of the 2 mm resolution are correct at least at a qualitative level. Increasing the resolution further makes the peaks in the local SAR higher.

Table 15 shows the calculated whole body and maximum local SAR's in the piece. In calculating these, we assumed a constant density of 1000 kg/m^3. Again, the 4 mm resolution seems insufficient.

Table 15: SAR in the muscle piece

	E cell [μW/kg]		H cell [μW/kg]	
Resolution	SAR_{wb}	SAR_{max}	SAR_{wb}	SAR_{max}
4 mm	16.79	184.37	17.76	223.33
2 mm	19.30	210.04	19.54	221.18
1 mm	19.97	220.08	20.01	222.80
0.5 mm	20.16	227.02	20.17	227.46

The wavelength at 2 GHz inside the muscle is $\lambda \approx 2.5$ cm. According to the results, the $\lambda/10$ rule seems to hold: 4 mm resolution — which doesn't satisfy

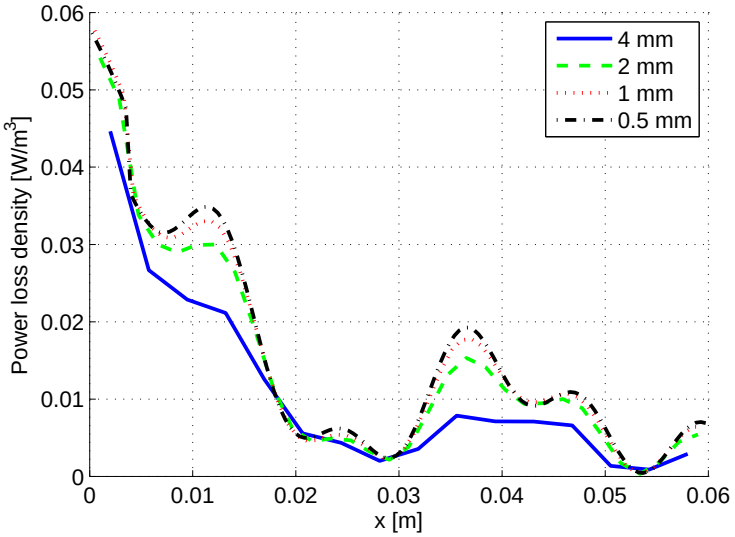

Figure 33: Local power loss density inside the muscle piece for various resolutions in the E-cell case.

the rule — fails to give good enough results, while higher resolutions seem to give reasonable results.

Comparing the results with the similar results for spheres (Sections 6.2.3 and 6.2.4), we see that the variation in SAR is of the same magnitude. The 2 mm resolution results seem to be slightly less accurate than the sphere results at 2 GHz in Tables 12 and 14. The results of the both cell types approach the correct(?) SAR from below, and the H cells seem to give slightly better SAR than the E cells. However, the difference between the convergence speeds and the accuracies of the SAR_{wb}'s of the two cell types is smaller than in the sphere cases.

When the E-cell approach is used with the sphere, increasing resolution reduced the calculated SAR, and in the present case, the SAR is increased when the resolution is increased. Thus we cannot generally say if insufficient resolution produces an over- or underestimation for the exposure.

6.3 SAR calculation methods

In the end, the SAR results naturally depend on how the SAR actually is calculated. This section deals with several methods which are utilized in determining SAR from the results of a FDTD simulation.

6.3.1 Power loss density calculation method

In Section 5.2, methods for determining the power loss density in FDTD grid were presented. They were based on simple numerical integration techniques, namely trapezoid and midpoint rules. Similarly to that section, all fields are amplitudes in the following. In the case of sinusoidal excitation, they can be calculated using (104).

Midpoint rule yielded

$$s = \frac{1}{2}\sigma|\mathbf{E}_{\text{ave}}|^2 = \frac{1}{2}\sigma \sum_{u=x,y,z} ((E_u)_{\text{ave}})^2. \tag{138}$$

The precise equations for the E-cell and H-cell cases are presented in Section 5.2. Let this method be called 'E_{ave}' method.

Another option in calculating the power loss density was the trapezoid rule, which gave

$$s = \frac{1}{2}\sigma(|\mathbf{E}|^2)_{\text{ave}} = \frac{1}{2}\sigma \sum_{u=x,y,z} (E_u^2)_{\text{ave}}. \tag{139}$$

Let's call this '$(E^2)_{\text{ave}}$' method.

When the material cells are H cells, one can derive an alternative method for calculating the local power loss density. This method employs the effective conductivities as described in Section 2.3.3. In the following, we assume the fields are amplitudes, and $\mathbf{J}$ denotes the amplitude of the conductivity current density, not the amplitude of the complex current density. Also, the (effective) electric field of the FDTD simulation is denoted by $\mathbf{E}_{\text{eff}}$, contrary to the notation used before in Sections 2.3.3 and 5.2 (in which it was simply $\mathbf{E}$).

Assume that the physical conductivity current density $\mathbf{J}$ can be calculated from the effective electric field $\mathbf{E}_{\text{eff}}$ by

$$\mathbf{J} = \sigma_{\text{eff}}\mathbf{E}_{\text{eff}}.$$

By (111), the rms value for the local power loss density is thus

$$s = \frac{1}{2}\mathbf{J} \cdot \mathbf{E}, \tag{140}$$

where $\mathbf{E}$ is the physical electric field, calculated from $\mathbf{E}_{\text{eff}}$ by (40).

Utilizing the midpoint rule, and assuming both $\mathbf{E}$ and $\mathbf{J}$ linear, the power loss in an FDTD cell $\mathbf{p} \in \mathcal{I}_H$ can be calculated by

$$s(\mathbf{p}) = \frac{1}{2}(\mathbf{J}_{\text{ave}} \cdot \mathbf{E}_{\text{ave}})(\mathbf{p}), \tag{141}$$

where 'ave' means taking average to the center point of the cell **p**. Let's call this approach the '$J_{\text{ave}}E_{\text{ave}}$' method.

Using the notation from Figure 17, this can be written

$$s = \frac{1}{2}\sum_{u=x,y,z}(J_u)_{\text{ave}}(E_u)_{\text{ave}} = \frac{1}{8}\sum_{u=x,y,z}(\sigma_{u1}E_{u1}+\sigma_{u2}E_{u2})(\frac{\epsilon_{u1}}{\epsilon}E_{u1}+\frac{\epsilon_{u2}}{\epsilon}E_{u2}), \quad (142)$$

where the notation is similar to (125), and $\{\sigma_{u1}\}$ and $\{\sigma_{u2}\}$ are the effective conductivities on the respective sides.

Another possibility is to utilize the trapezoid rule: calculate the power loss on each side, and take the average of these

$$s = \frac{1}{2}\sum_{u=x,y,z}(J_uE_u)_{\text{ave}} = \frac{1}{4}\sum_{u=x,y,z}(\sigma_{u1}\frac{\epsilon_{u1}}{\epsilon}E_{u1}^2+\sigma_{u2}\frac{\epsilon_{u2}}{\epsilon}E_{u2}^2). \quad (143)$$

Let this be called 's_{ave}' method.

In E cells, there is no point in using the above approaches, because the current density calculated using the effective conductivity is an effective field.

The following table summarizes the four power loss density calculation methods presented above.

Table 16: Power loss density calculation methods

Method	Equation	Summary	Integration method	Cell types
E_{ave}	(138)	$\frac{1}{2}\sigma\lvert\mathbf{E}_{\text{ave}}\rvert^2$	Midpoint	E and H
$(E^2)_{\text{ave}}$	(139)	$\frac{1}{2}\sigma(\lvert\mathbf{E}\rvert^2)_{\text{ave}}$	Trapezoid	E and H
$J_{\text{ave}}E_{\text{ave}}$	(142)	$\frac{1}{2}\mathbf{J}_{\text{ave}}\cdot\mathbf{E}_{\text{ave}}$	Midpoint	H
s_{ave}	(143)	$\frac{1}{2}(\mathbf{J}\cdot\mathbf{E})_{\text{ave}}$	Trapezoid	H

The methods presented in the Table 16 were then tested by applying them to the simulations presented in Sections 6.2.3 and 6.2.4. The whole-body SAR results are plotted in Figures 34–40. The values are given as percentages to the accurate Mie theory values.

Several observations can be made based on the figures: There are significant differences in the whole-body SAR values calculated with either trapezoid or midpoint rules. This difference was sometimes as big as the difference due to the material cell types, and it was especially large when the resolution was insufficient, not satisfying the $\lambda/10$ rule. Examples of this are seen in the last three figures. As the resolution was increased, both the trapezoid and midpoint results converged to the same value.

For the E-cell case, the method utilizing the midpoint rule always gave seemingly better results than the trapezoid-rule method. For example, in the TE-resonance case in Figure 35, the midpoint rule SAR_{wb} stays almost constant with the resolution. The trapezoid-method result is worse at a coarse resolution, and converges to the midpoint result when the resolution is increased. On the other hand, the trapezoid-rule methods seemed to give somewhat better results in the H-cell case. This can be seen particularly well in Figures 37–40.

Theoretically, there should be no fundamental reasons why one method would be worse or better than the other. Thus we can choose: in the E-cell case, the midpoint rule is used, and in the H-cell case, the trapezoid rule is used.

The $J_{\text{ave}}E_{\text{ave}}$ and s_{ave} methods always gave results very similar to the $(E^2)_{\text{ave}}$ and E_{ave} methods, respectively. This is natural when comparing the formulae of the methods. However, there are some facts that make the E_{ave} and $(E^2)_{\text{ave}}$ methods slightly preferred in SAR calculation.

In the cells that are surrounded by cells of higher conductivity, the $J_{\text{ave}}E_{\text{ave}}$ and s_{ave} methods will generally give higher power loss density than their E_{ave} and $(E^2)_{\text{ave}}$ counterparts. In the cells surrounded by smaller conductivity cells, they will give smaller power loss density. And in a homogeneous situation, the $J_{\text{ave}}E_{\text{ave}}$ and s_{ave} methods will give the same values as E_{ave} and $(E^2)_{\text{ave}}$ methods.

So, in a situation such as the sphere cases studied here, the E_{ave} and $(E^2)_{\text{ave}}$ methods will always give greater power loss values than their $J_{\text{ave}}E_{\text{ave}}$ and s_{ave} counterparts (There are more (non-air) cells whose neighbors have lesser conductivities than there are cells whose neighbors have higher conductivities). In a heterogeneous situation, such as a human body model, the situation is more complicated, as there are both kinds of cells. However, it can be assumed that most likely whole-body-averaged SAR will be higher using E_{ave} and $(E^2)_{\text{ave}}$ methods, because the body is surrounded by air. Slight overestimation such as this is not necessarily a bad thing in SAR assessment.

This — and slightly easier implementation — makes the E_{ave} and $(E^2)_{\text{ave}}$ methods preferred over the $J_{\text{ave}}E_{\text{ave}}$ and s_{ave} methods.

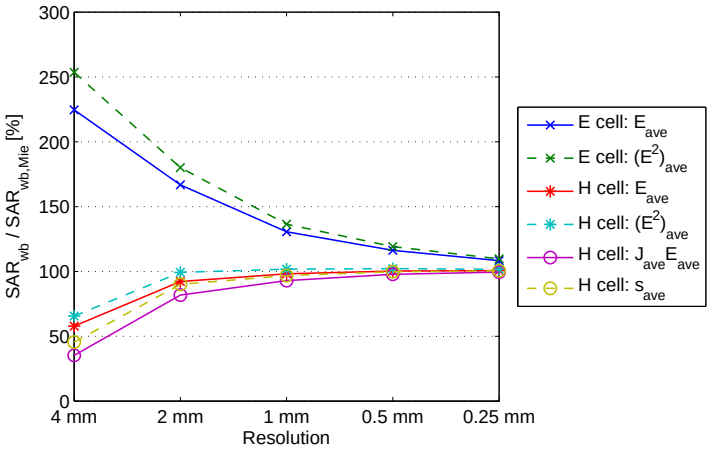

Figure 34: SAR_{wb} in a muscle sphere of radius $a = 0.65$ cm at 1 GHz.

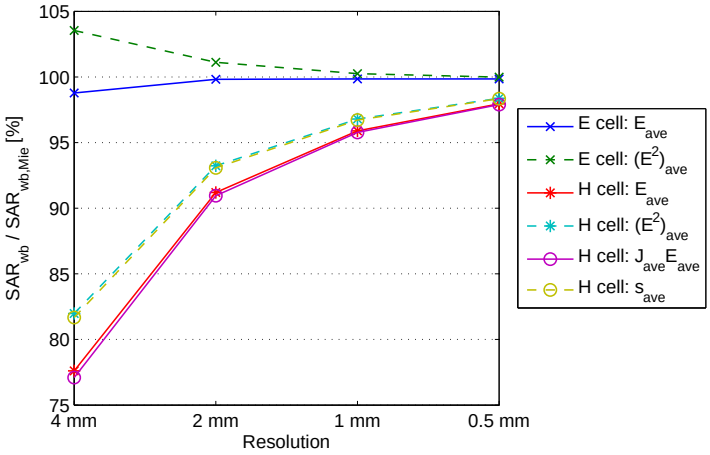

Figure 35: SAR_{wb} in the 1 GHz TE-resonance muscle sphere, $a = 2.35$ cm.

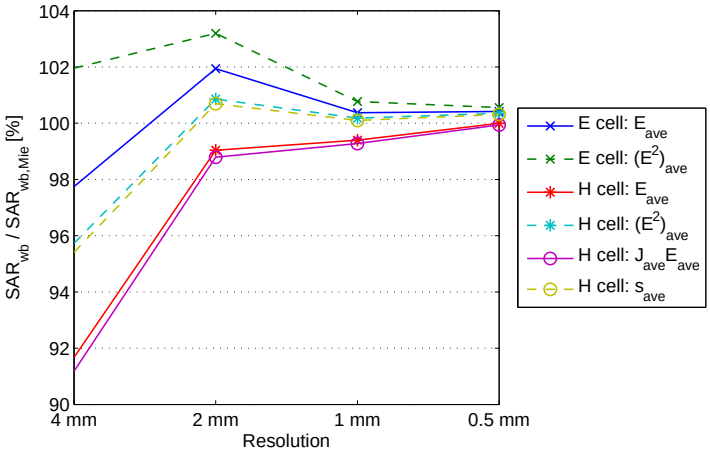

Figure 36: SAR_{wb} in a muscle sphere at 1 GHz, $a = 2.5$ cm

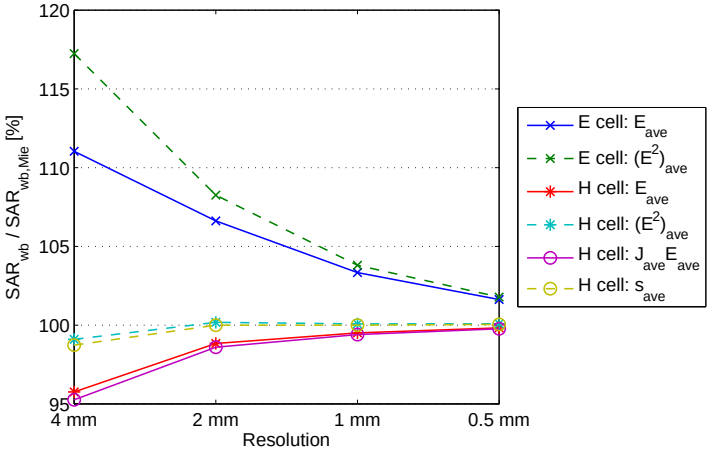

Figure 37: SAR_{wb} in the 1 GHz TM-resonance muscle sphere, $a = 3.35$ cm.

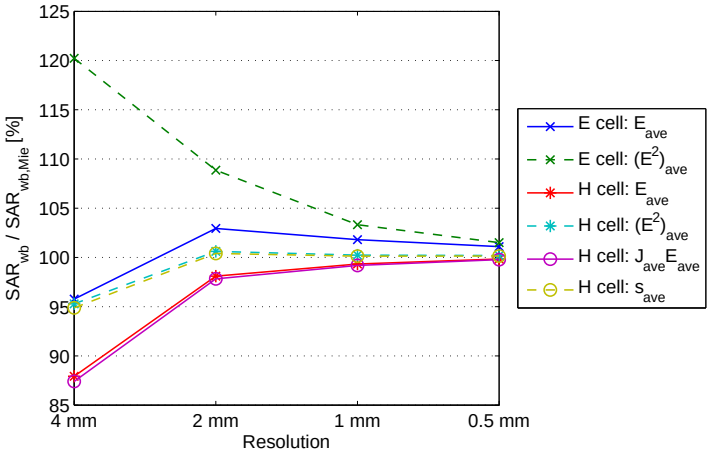

Figure 38: SAR_{wb} in a muscle sphere at 2 GHz, $a = 2.5$ cm

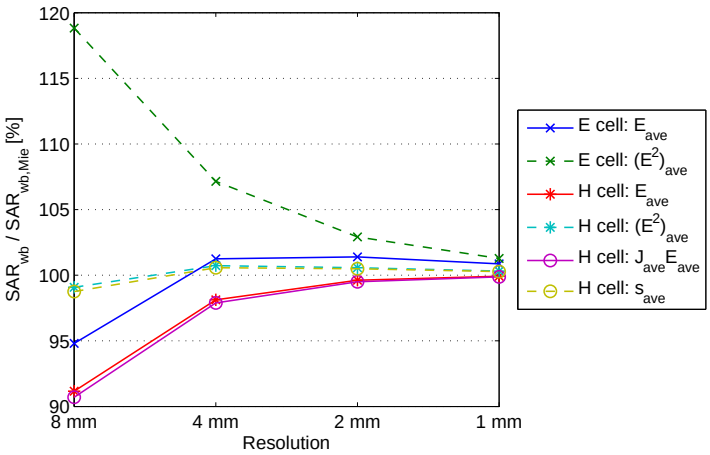

Figure 39: SAR_{wb} at 1 GHz in a large muscle sphere of radius $a = 10.0$ cm.

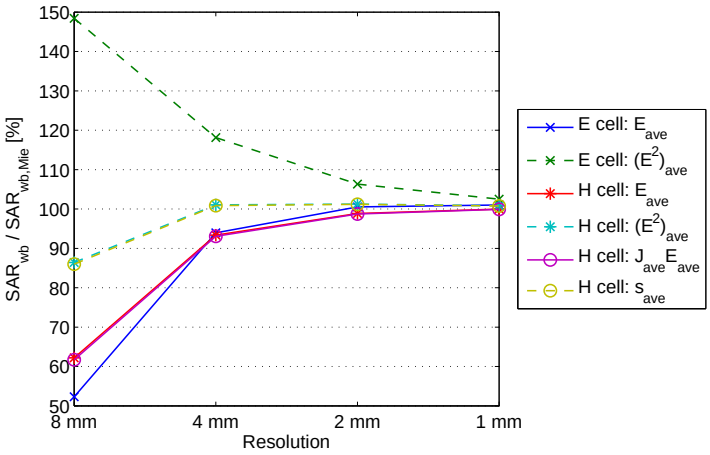

Figure 40: SAR_{wb} at 2 GHz in a large muscle sphere of radius $a = 10.0$ cm.

6.3.2 Simplified local spatial-averaged SAR calculation method

A simpler method of linear interpolation for the local spatial-averaged SAR calculation presented in Section 5.3 was proposed in [25].

Using the linear interpolation, the corresponding equations in steps 3 and 4 in the algorithm in page 40 are replaced with

$$f = \frac{m_{\text{avg}} - m(\mathcal{C}_l)}{m(\mathcal{L}_l)} \tag{144}$$

and

$$SAR_{\text{avg}}(\mathbf{p}) = \frac{P(\mathcal{C}_l) + fP(\mathcal{L}_l)}{m_{\text{avg}}}. \tag{145}$$

Table 17 shows the maximum difference in averaging cube masses calculated with (144) compared to the accurate method for the Norman phantom. IEEE recommendations [21] allow a 5 % variation in averaging cube masses, and the 10 g cubes calculated with (144) satisfy this.

Table 17: Maximum difference in the masses of the averaging cubes calculated with the linear method compared to the accurate method for Norman.

Averaging mass	Difference
10 g	4.58 %
1 g	19.2 %

The averaging cubes calculated above were used to evaluate the averaged SAR in an example simulation. Norman was placed 30 cm in front of a base station antenna at frequency 900 MHz. Table 18 shows the difference in calculated SAR for (145) and the accurate method. The local differences may be large for extremely small SAR values, as can be seen in the second column of the table. These are rarely of interest. More importantly, as the third column shows, the difference in the interesting maximum SAR values is small. Thus, the simpler method of linear interpolation may often be sufficient in practice.

Table 18: Differences in the spatial-averaged-SAR values between the linear and the accurate method for Norman.

Averaging mass	$\max(\Delta SAR_{\text{avg}})$	$\Delta \max(SAR_{\text{avg}})$
10g	23.4 %	0.30 %
1g	61.8 %	0.25 %

6.3.3 Whole-body SAR averaging method

Two SAR averaging methods were presented in Section 5.1, namely the volume-averaging (115) and the mass-averaging (116) methods. The standards by IEEE and ICNIRP can be interpreted to require the volume-averaging method, while

intuitively (and as shown in [24]) the mass-averaging method seems more reasonable. For homogeneous cases, these two methods will give the same values, but in a hetoregenous human body model, their results will generally be different.

Table 19 shows an example how the two averaging methods affect the whole-body-averaged SAR values. The simulation setup and notation is the same as in Table 23 in Section 6.5.1. The percentage values are the differences of the volume-averaged SAR relative to the mass-averaged SAR.

Table 19: The difference in the whole-body-averaged SAR calculated with mass and volume averaging.

	900 MHz		1800 MHz	
Resolution	E cell	H cell	E cell	H cell
3.6 mm	1.70 %	2.99 %	-1.23 %	0.65 %
1.8 mm	1.94 %	2.81 %	-0.81 %	0.63 %

It seems that the difference between the two methods may be at least up to 3 %, so it is not completely negligible. Also, both methods may produce higher or lower values than the other.

6.4 Modeling sources and base station antennas

Several relevant results associated with Section 4 are presented in this section.

6.4.1 Steady-state convergence

When the sinusoidal excitation is used, as described in Section 4.3, the simulation must be run long enough so that the steady state has been reached. The convergence to the steady state can be made quicker by tapering the input sine signal, which means starting the input signal at zero amplitude and increasing the amplitude to its final value gradually over a few periods.

Assume the time dependence of the electric field of the sources is of the form

$$E_{\text{source}}(t) = A(t)E_0 \sin(2\pi f t), \ t \in \mathbb{R}, \tag{146}$$

where $A(t)$ is the tapering function. In a continuous time-harmonic case, the tapering function would be constant $A(t) \equiv 1$. In an FDTD simulation, the fields are initialized to zeros, and the sources are turned on at $t = 0$, so the tapering function is zero for $t < 0$. The most simple $A(t)$ for FDTD is a unit step function, which in the following refers to "no tapering". Using a smoother tapering function may make the starting transients smaller and speed up the convergence to the steady-state, and thus decrease the CPU time needed for the simulation.

The effects of using a tapering function were tested in a simulation which consisted of the Visible man model in free space. The resolution of the model was 1 mm, and it was exposed to a vertically polarized plane wave, the frequency of which was 1.8 GHz. In this case, the tapering function $A(t)$ was a sigmoid function

$$A(t) = \frac{1}{1 + e^{\frac{t_0 - t}{\tau}}}, \tag{147}$$

where t_0 and τ are constants. The time signals of the incident plane wave are shown in Figure 41, with and without tapering.

The maximum of the electric field amplitude on a horizontal cross-section of the head (includes the surrounding air) is shown in Figure 42 as a function of time. Without tapering, the amplitude reaches the vicinity of its final value fast, but oscillates around it. The magnitude of the oscillation is initially approximately 2 % of the final value, and decays slowly. With tapering, the convergence to the final value is slower, but the oscillation is nearly nonexistent.

There is a "biological" explanation for the oscillation of the electric field amplitude. The slow variation of the amplitude of the electric field has a period of approximately 30 times the original period. Thus the frequency of the variation is ≈ 60 MHz. This is very close to the whole-body resonant frequency for vertically polarized fields: According to [29], the whole-body resonance happens when the body length is approximately 0.38λ–0.40λ, where λ is the wavelength in free space. At ≈ 60 MHz, this is $\approx$ 190–200 cm, which corresponds to the height of the Visible man.

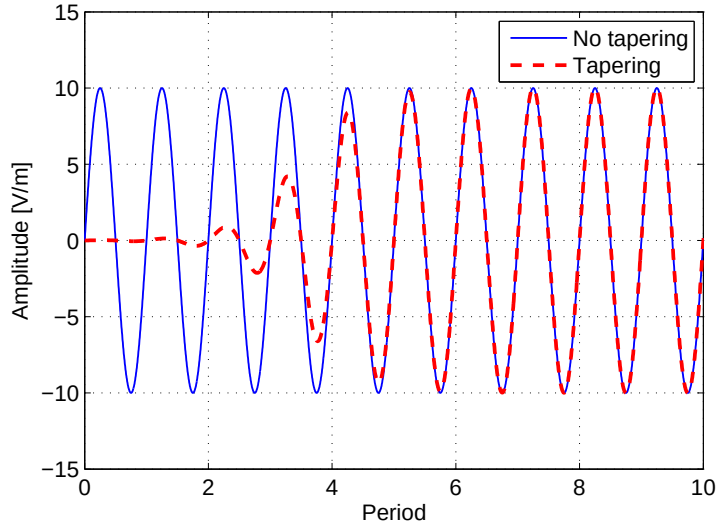

Figure 41: Incident plane wave amplitude

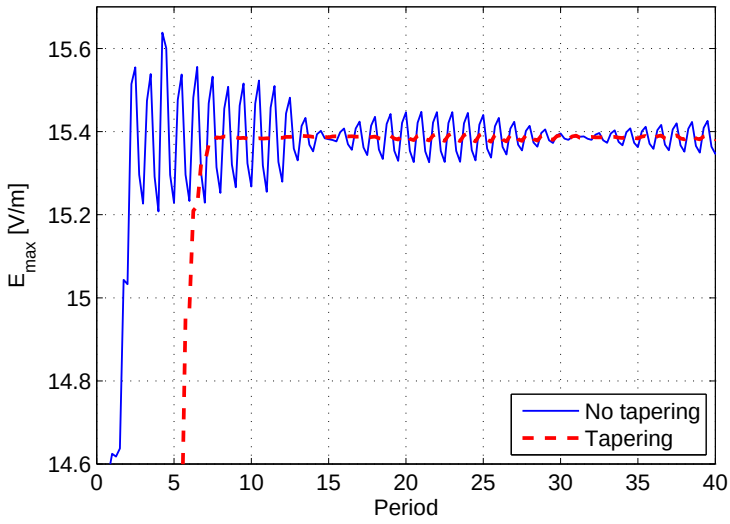

Figure 42: Maximum electric field amplitude on a horizontal cross-section of the head. The amplitude is calculated using (104).

In summary, it is useful to utilize tapering to reduce the magnitude of the slowly vanishing low-frequency whole-body resonances, i.e. to make the whole-body resonant frequency component in the excitation signal spectrum as small as possible.

6.4.2 Modeling dipole antennas

An important part of modeling base station antennas is the modeling of individual elements. This section describes and tests some possible ways to model dipole antennas.

Four different dipole models were studied. The sketches of the models are shown in Figure 43, which shows one half of the dipoles and the location of the discrete source. The length of the discrete source is 3 mm in all models, except in model

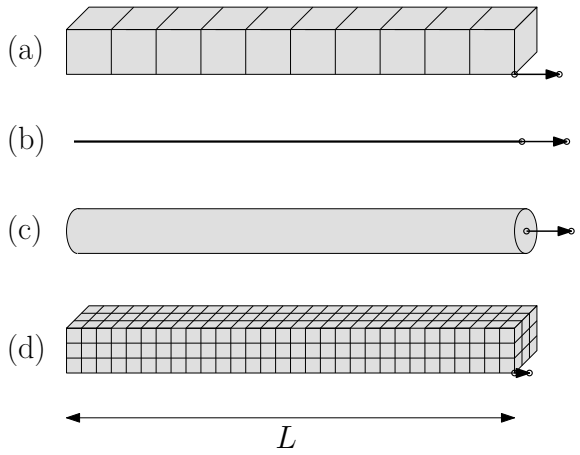

Figure 43: Modeling a dipole antenna in FDTD: (a) 3 mm resolution rectangular dipole, (b) 3 mm resolution thin wire dipole, (c) 3 mm diameter cylindrical dipole with non-uniform resolution and curved boundary approximation, and (d) 1 mm resolution rectangular dipole

(d), in which the length is 1 mm. The frequency is 2140 MHz, and the length of the dipole half L is 33 mm, which means the total length of the dipole including the source is 0.492λ in models (a)–(c), and 0.478λ in model (d). Notice the position of the discrete source in models (a) and (d).

Table 20 shows the calculated directivities in two directions at 2140 MHz. The "front" and "back" directions mean the front and back sides of the dipoles as they are shown in Figure 43, respectively.

The directivities match very well, which is natural, as the far fields of thin dipole antennas should not depend on the thickness or the shape of the cross-section of the wires.

Table 20: The calculated directivity at 2140 MHz for the different dipole antenna models

	Directivity (back)	Directivity (front)
Model (a)	1.671	1.683
Model (b)	1.668	1.668
Model (c)	1.666	1.666
Model (d)	1.651	1.657

Figure 44 shows the calculated electric field amplitude on a line in "front" of the dipole. The radiated power was the same for all dipoles. The difference in electric field amplitude is less than 1 % for distances larger than 30 mm.

From now on, models (a) and (d) are used in this work. The results presented here suggest that they are good enough approximations for dipole antennas, and

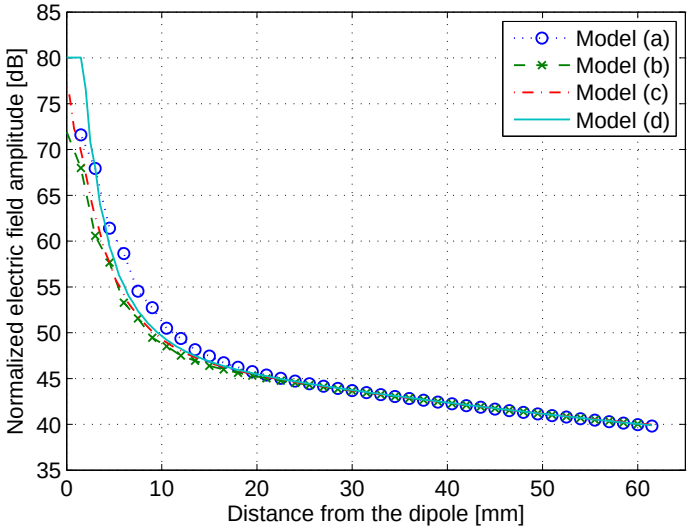

Figure 44: Normalized electric field amplitude in decibels ($20\log(|\mathbf{E}|)$ dB) at 2140 MHz

there seems to be no need to refine the mesh near the antennas. (a) and (d) gave similar results, so the antenna models should be sufficiently equivalent when comparing the BSA-body model results calculated with different resolutions.

6.4.3 Radiated power calculation method

The SAR results are often normalized with respect to the total radiated power[11] P_{rad} of the antenna. Consequently, the SAR results are affected by the calculation method of P_{rad}.

There are at least two ways to calculate the total radiated power:

Circuit-parameters method: Summing the net powers as in (106), where the net powers are calculated using the currents and voltages over the discrete sources by (96).

Huyghens-surface method: Recording Poynting vector normal component along a surface which encloses the sources and no lossy materials, and integrating to get the total power radiated through the surface.

In theory, these two methods should give the same radiated power. In practice, the circuit parameters method is preferred, as it is much simpler and cheaper to implement.

The radiated powers of the four dipole antenna models of the previous section were calculated with both methods. The results are presented in Table 21. They are normalized with respect to the circuit-parameters method radiated power (separately for each model). The radiated powers are very similar. With models (c)

[11] The net power which is fed into the FDTD-computation domain by the antenna.

and (d), the two methods match a little better than with the models (a) and (b). This might be related to the fact that models (c) and (d) had finer resolutions than (a) and (b), and thus the interpolation errors in the Huyghens-surface method are smaller. Based on these results, calculating the total radiated power with the circuit method (106) appears to be well justified.

Table 21: Radiated power calculated with the two methods for the dipole antennas of Section 6.4.2

	Circuit [W]	Huyghens [W]
Model (a)	1.0000	1.0147
Model (b)	1.0000	1.0167
Model (c)	1.0000	1.0020
Model (d)	1.0000	1.0042

6.4.4 Effects of antenna feed modeling on SAR

It was discussed in Section 4.5.2 that modeling the antenna feeds, i.e. the choice of the inner resistances of the discrete sources, has a variety of effects which may affect the calculated SAR values. The dependence of the radiated power and SAR values on the inner resistances is studied in this section by exposing a box phantom to a small base station antenna.

A two-element base station antenna was placed in front of a rectangular phantom the size of which was $36 \times 21 \times 6$ cm^3. The situation is illustrated in Figure 45. The material of the phantom was 2/3 muscle, with $\epsilon_r = 37.18$ and $\sigma = 1.056$ S/m. The studied frequency was 2140 MHz, and the dipole lengths were approximately $\lambda/2$. The mesh resolution was approximately 3 mm. The dipole feeds were discrete sources with inner resistances, as described in Section 4.1, and the values of the inner resistance R_g were the same for both discrete sources.

The phantom-antenna distance and the value of the inner resistance R_g were varied, and whole-body SAR and the maximum of the local power loss density were recorded for each distance-resistance combination. Two different amplitude distributions of the antenna were studied: Firstly, a uniform distribution, in which the amplitudes of the voltage sources of the both elements were the same. And secondly, a nonuniform distribution, in which only the upper dipole in Figure 45 is excited, and the amplitude of the lower element is set to zero.

It was observed in Section 4.5.2 that the total radiated power depends the distance to the phantom. Here, this dependence is studied for several values of the inner resistance R_g. For each value of R_g, the gross input power (97) is chosen so that the total (net) radiated power is 1 W in free space. The antenna-phantom distance is varied, keeping the gross power constant. This is done using five different values for the inner resistances of the antenna. Figure 46 shows the total (net) radiated power of the antenna as a function of distance from the phantom in the case of the uniform amplitude distribution. It seems that the inner resistance $R_g = 150\ \Omega$ is the most

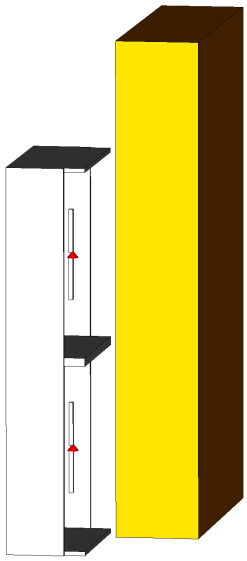

Figure 45: The two-element antenna and the rectangular phantom. The position of the phantom in the direction of the long axis of the antenna is shifted 6 cm upwards, so the situation is not symmetric.

realistic value, because the radiated power is an (almost) increasing function of the antenna-phantom distance.

Next, the effects of the inner resistance on the normalized (P_{rad} = const.) SAR values are studied. Figures 47 and 48 show the differences due to the inner resistances in the normalized whole-body SAR and local power loss density, respectively. At each distance, the differences are calculated with respect to the normalized SAR values when the inner resistance $R_g = 150\ \Omega$. Both the uniform and the nonuniform amplitude distributions are used.

With the uniform amplitude distribution, the differences due to the inner resistances were up to 1 % in whole-body SAR, and up to 2 % in the maximum local power loss density. Nonuniform amplitude distribution produced larger differences; up to 2.5 % in whole-body SAR and 6 % in the maximum local power loss density.

As a conclusion, it is clear that the choice of the inner resistances does have an effect on the normalized SAR values. However, the discrete sources are merely approximations, and in a realistic antenna the sources would be more complicated than just a resistance and a voltage source. Modeling the sources accurately would require an accurate circuit model of an antenna, which is out of scope of this work.

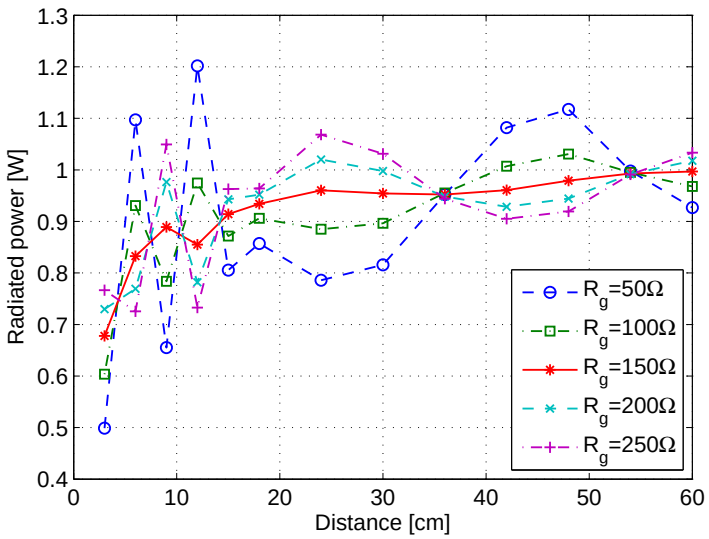

Figure 46: Normalized radiated power as a function of antenna-phantom distance. Gross input power (97) is constant, such that the radiated power is 1 W without the phantom.

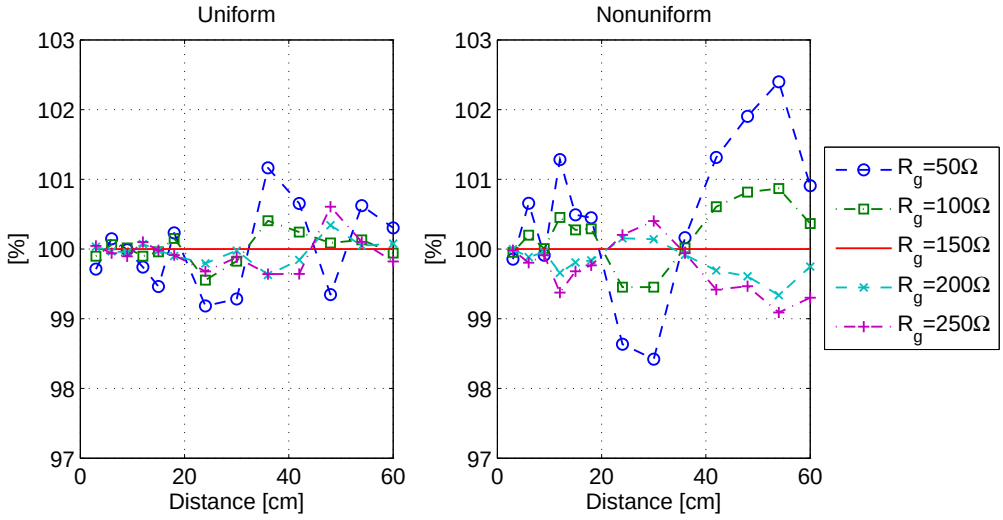

Figure 47: The difference in the normalized (P_{rad} = const.) whole-body-averaged SAR as a function of antenna-phantom distance for the uniform (left) and the nonuniform (right) amplitude distributions.

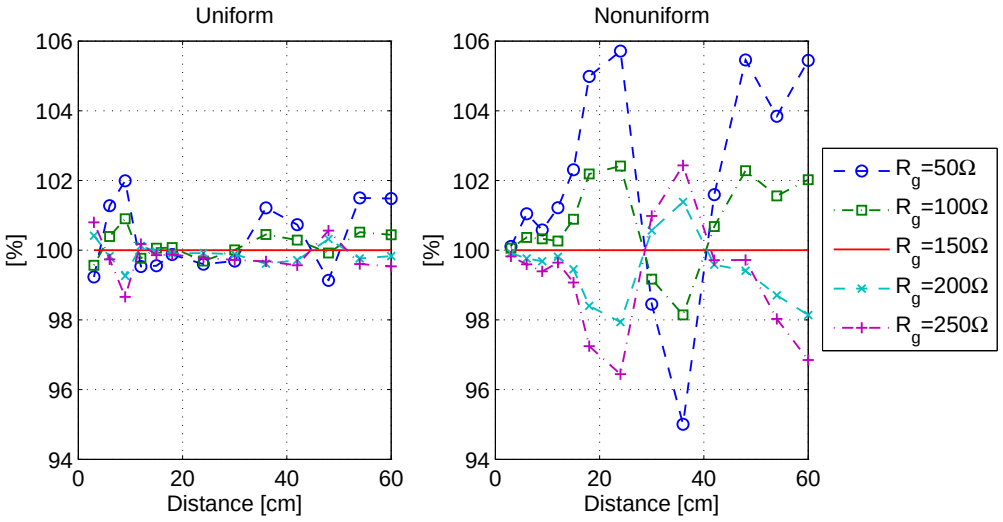

Figure 48: The difference in the normalized (P_{rad} = const.) maximum local power loss density as a function of antenna-phantom distance for the uniform (left) and the nonuniform (right) amplitude distributions.

6.5 SAR calculations in human body models

6.5.1 Effects of resolution in human body models

The accuracy of the FDTD method in SAR calculation was studied in Section 6.2 for canonical cases, such as spheres or rectangles. The objective of this section is to study if similar results can be obtained for human body models. They are large and heterogeneous — quite different from small homogeneous spheres or rectangles.

Even though the models are more complex, the algorithm stays the same — Yee's algorithm is second order accurate, and increasing the resolution will reduce the discretization error. In addition to this, the mesh resolution affects the accuracy of the anatomical modeling.

Several papers have discussed the effects of resolution in human-SAR calculations, for example the following. In [8], 3 mm and 5 mm Visible man models were exposed to a plane wave. It was concluded that the resolution had "very little" (up to 8 % at 2 GHz) influence on the whole-body SAR. Whole-body SAR in Norman exposed to a plane wave was studied in [29] at resolutions up to 2 mm. Conclusion was that the whole-body SAR is a robust quantity with respect to the model resolution (at frequencies up to 1 GHz).

The available body models in this work were Visible man with two resolutions, Zubal and Norman, as described in Section 2.3.6. In order to study the effects of resolution, higher-resolution models can be created by splitting each voxel into eight new voxels, which is illustrated in Figure 49. This kind of artificial increase in resolution does not improve the accuracy of anatomical modeling, but reduces the discretization error of the Yee algorithm. This method was utilized to create Norman

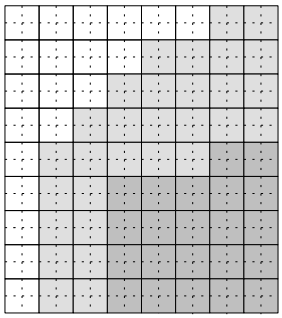

Figure 49: Increasing the resolution of a human voxel model by splitting each cell into eight (here: four) smaller cells.

model with a 1.011 mm resolution, and Zubal model with a 1.8 mm resolution. As a result, we have a total of six models. They are listed in Table 22.

The effects of resolution on the whole-body-averaged and localized SAR values were studied by exposing each phantom to a vertically polarized plane wave with power density 1 W/m^2. The propagation direction of the wave was towards the face of the phantom. The studied frequencies were 900 MHz, 1800 MHz and 2140 MHz, which correspond to frequencies commonly used in mobile communications.

Tables 23, 24 and 25 show the SAR results for the two resolutions of Zubal,

Table 22: The resolutions of the available human body models. # of cells denotes the size of the box including the model.

	Resolution		
Model	FDTD	Anatomical	# of cells
Zubal	3.6 mm	3.6 mm	$87 \times 147 \times 493$
Zubal	1.8 mm	3.6 mm	$174 \times 294 \times 986$
Norman	2.022 mm	2.022 mm	$148 \times 277 \times 871$
Norman	1.011 mm	2.022 mm	$296 \times 554 \times 1742$
Visible man	3 mm	3 mm	$109 \times 190 \times 625$
Visible man	1 mm	1 mm	$326 \times 568 \times 1877$

Norman and Visible man, respectively. The Zubal model was simulated for both the E-cell and H-cell cases, while Norman and Visible man models were always positioned in the E cells. The difference column tells the difference of the lower-resolution result with respect to the more accurate high-resolution result. Comparison of the Norman and Visible man results in these tables can be found in Table 30 in the next section.

Table 23: The whole-body and the maximum 10 g SAR values in Zubal at plane-wave exposure. The maximum of the 10 g SAR is located in the hands. The units are [mW/kg].

		900 MHz		1800 MHz	
Cell	Resolution	SAR_{wb}	$SAR_{10\mathrm{g}}$	SAR_{wb}	$SAR_{10\mathrm{g}}$
E	3.6 mm	6.418	97.57	4.510	81.47
E	1.8 mm	6.581	111.70	4.964	87.25
Difference [%]		-2.49	-12.65	-9.13	-6.62
H	3.6 mm	6.784	181.98	5.673	125.59
H	1.8 mm	6.787	163.58	5.639	123.99
Difference [%]		-0.05	11.25	0.59	1.29

Table 24: Whole-body and the maximum 10 g SAR in Norman at plane-wave exposure. The maximum of the 10 g SAR is located in the nose. The units are [mW/kg].

	900 MHz		2140 MHz	
Resolution	SAR_{wb}	$SAR_{10\mathrm{g}}$	SAR_{wb}	$SAR_{10\mathrm{g}}$
2.022 mm	6.810	84.75	6.720	99.64
1.011 mm	6.846	85.52	6.390	99.82
Difference [%]	-0.53	-0.91	5.16	-0.18

Table 23 shows the SAR values in Zubal phantom at both resolutions and frequencies 900 MHz and 1800 MHz. The simulations were performed both when the materials cells were E cells, and when the material cells were H cells. The difference

Table 25: Whole-body and the maximum 10 g SAR in Visible man at plane-wave exposure. The maximum of the 10 g SAR is located in the hands. The units are [mW/kg].

	900 MHz		2140 MHz	
Resolution	SAR_{wb}	SAR_{10g}	SAR_{wb}	SAR_{10g}
3 mm	5.819	97.37	4.355	93.09
1 mm	5.933	118.36	4.607	97.32
Difference [%]	-1.94	-17.74	-5.48	-4.34

in the E-cell and H-cell results is large, and the H cells always gave both higher whole-body and localized SAR. For the H cells, the whole-body SAR stayed almost constant with the resolution for both frequencies, and for the E cells, increasing the resolution changed the whole-body SAR more.

The difference in the maximum 10 g SAR was especially large, as the H cells typically produced approximately 50 % higher values than the E cells. The maximum was located in the hands for both cell types, which might explain some of the difference. Additionally, the maximum value was highly sensitive to the resolution, especially at 900 MHz, which implies that the geometry of the hands may be a particularly difficult case for the FDTD method.

The difference between the E-cell and the H-cell results is so large that it makes the validity of the H-cell approach somewhat suspected for highly heterogeneous cases such as this. On page 11, the approximations of the real and imaginary parts of the effective complex permittivity (39) by the simpler formulas should be reviewed. But then, the E-cell results do not seem so good either, as they are highly sensitive to the resolution.

The anatomical resolutions of the two resolutions of the Visible man model were different, and the results differ quite a lot. Especially, at 900 MHz, the maximum of the 10 g SAR is very sensitive to the resolution. However, it seems that most of this large difference is due to the other factors than the anatomical accuracy. Namely, the arms and hands of both Visible man and Zubal are based on the same data [9], and the peak 10 g averaged SAR results seem to match very well (Zubal in E cells). The sensitivity with the resolution is clear also in the SAR values of Zubal, even though the both resolutions of Zubal have the same anatomical resolution. Conclusion is that there were no differences which could not have been explained by the different FDTD resolutions, and the FDTD resolution seems more significant than the anatomical resolution.

Of the three models, the localized SAR values of Norman were the most robust with the resolution. This might have to do with the posture of the model and the position of the maximum SAR_{10g}, which were different in the other models. As a conclusion, it seems that the model and its posture may have a large effect on how sensitive to the mesh resolution the localized SAR values are.

The ICNIRP basic restriction limits for the general public exposure are 0.08 W/kg for whole-body SAR and 2 W/kg for the peak 10 g averaged SAR (Table 4), assum-

ing the 10 g SAR maximum is in the head or trunk of the phantom. Actually, this was not always the case, e.g. Visible man and Zubal had the maximum 10 g SAR in the hands. In all the results[12], the condition for the whole-body SAR is more restrictive than the condition for the localized SAR.

Plane wave can be used as an approximation of the farfield of a base station antenna by (108). However, based on the results, such an approximation has little use when assessing base station exposure in practice. This is best justified by an example.

For example, take Norman at 2140 MHz. The power density of the incident plane wave would have to be 12.5 W/m^2 in order to produce whole-body SAR values which exceed the basic restriction limits for general public exposure (Table 4). Assume an antenna-body distance of 5 m, which is probably too small for the plane-wave approximation to be reasonable. For an antenna with a (high) directivity of 10 (20 dBi), producing such a power density would require an antenna radiated power of about 400 W, which is very high. Thus it is unlikely that the basic restrictions will be exceeded far from the antenna, where the plane wave approximation is reasonable.

[12]except Zubal in the H cells at 900 MHz and 3.6 mm resolution

6.5.2 Human exposure to base station antennas

Several results involving human body model near a base station antenna are presented in this section.

A base station antenna consisting of four elements, the details of which are presented in Table 26, was placed in front of a human body model. The available human models were listed in Table 22. Of those, 1.011 mm Norman and 1 mm and 3 mm Visible man models are used in this section. The materials of the models are positioned in the E cells. The position of the base station antenna with respect to the human model was chosen such that whole-body SAR would be as large as possible, and it is shown in Figure 50.

Table 26: Antenna properties

Frequency	2140 MHz
Length of the dipoles	$\approx \lambda/2$
Number of elements	4
Directivity	15.6 dBi
Beam width (vertical)	13.4
Beam width (horizontal)	67.0
Inner resistances R_g	50 Ω

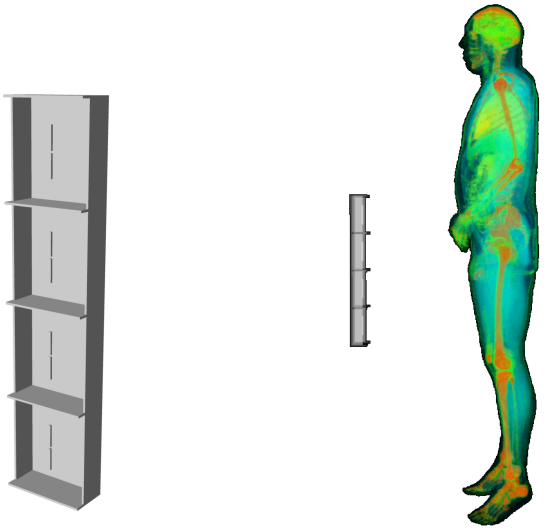

Figure 50: Base station antenna and its position with respect to the human model.

The SAR values as a function of body-antenna distance[13] using the Norman model are presented in Table 27, and the Visible man SAR results are found in Tables 28 and 29 for the 1 mm and 3 mm resolutions, respectively. The Visible man results have been previously presented in [30]. The SAR values are calculated assuming the total radiated power (106) is 1 W.

[13] Assuming the x axis is parallel to the main lobe direction, this distance is the difference in the x coordinates between the outermost point of the antenna and the outermost point of the body.

In the tables, the *threshold power* is calculated from the SAR results. It is defined so that the radiated powers greater than the threshold power cause the basic restriction limits to be exceeded. ICNIRP basic restrictions for the general public exposure (European council recommendations) are used. For occupational exposure, the threshold powers should be multiplied by five. The threshold power for the 10 g averaged SAR is calculated assuming the maximum is located in the head or trunk of the phantom (the basic restriction limits are stricter there). Actually, the maximum of the 10 g SAR in the Visible man phantom is located in the hands, so the threshold power should be a little higher.

Table 27: Whole-body and maximum 10 g SAR values in the 1.011 mm Norman phantom at different body-antenna distances.

Distance	SAR_{wb} [mW/kg]	Threshold [W]	$SAR_{10\mathrm{g}}$ [mW/kg]	Threshold [W]
5 cm	7.376	10.8	878.3	2.3
15 cm	6.603	12.1	516.0	3.9
30 cm	5.411	14.8	367.9	5.4
45 cm	4.595	17.4	351.5	5.7
70 cm	3.205	25.0	240.1	8.3

Table 28: Whole-body and maximum 10 g SAR values in the 1 mm Visible man phantom at different body-antenna distances.

Distance	SAR_{wb} [mW/kg]	Threshold [W]	$SAR_{10\mathrm{g}}$ [mW/kg]	Threshold [W]
15 cm	5.334	15.0	482.3	4.1
30 cm	4.080	19.6	369.7	5.4
45 cm	3.244	24.7	361.6	5.5
70 cm	2.185	36.6	272.8	7.3

Table 29: Whole-body and maximum 10 g SAR values in the 3 mm Visible man phantom at different body-antenna distances.

Distance	SAR_{wb} [mW/kg]	Threshold [W]	$SAR_{10\mathrm{g}}$ [mW/kg]	Threshold [W]
15 cm	4.833	16.6	540.1	3.7
30 cm	3.683	21.7	394.4	5.1
45 cm	2.903	27.6	321.6	6.2
70 cm	1.970	40.6	248.4	8.1

In all situations presented here, the threshold powers for the localized SAR are lower than the threshold powers for the whole-body SAR, which means the localized SAR limit is more restrictive than the limit due to the whole-body SAR. In the case of plane-wave exposure, the situation was the opposite.

The threshold powers are relatively low, under 10 W for all distances and all models. A realistic antenna might have a radiated power of 30 W, which exceeds

the calculated threshold powers by a large margin, and the compliance distance will most likely be well over 1 m.

The peak 10 g SAR seems to match quite well for both Norman and Visible man with both resolutions. This might just be coincidence, because the postures of Norman and Visible man are different, and the maxima are located in different body parts: in the hands for Visible man, and in the penis for Norman.

The difference in both localized and whole-body-averaged SAR for the two resolutions of the Visible man are approximately 10 %: The lower resolution always underestimated the whole-body SAR by 10 %, and the peak 10g SAR was underestimated by approximately 10 % at small distances, and overestimated equally at larger distances. Consequently, there is no clear "saddle point" in the peak 10 g averaged SAR at distances 30–45 cm, contrary to the 1 mm resolution. This saddle point is also present in the Norman results.

When the SAR results of two different phantoms are compared, it seems more reasonable to use total power loss $P_{\text{loss}} = m_{\text{body}} SAR_{\text{wb}}$, where m_{body} is the total body mass, instead of the whole-body SAR, because the whole-body SAR seems heavily affected by the total mass of the phantom. E.g. the whole-body SAR of Norman is always considerably higher than the whole-body SAR of the heavier Visible man. Table 30 shows the comparison of the SAR values between Norman and the two Visible man models. The farfield SAR values are calculated from the plane-wave results of the previous section.

When comparing the results for Norman and the 1 mm Visible man, several observations can be made. When the distance to the antenna is increased, the total power loss inside the Visible man decreases slower than the total power loss inside Norman. This might be related to the fact that Visible man is taller than Norman, and thus Visible man's absorption cross section is larger. The behavior of the 10 g averaged SAR as a function of the antenna distance was the opposite: Near the antenna, Visible man had higher 10 g SAR values, and far from the antenna, Norman's 10 g SAR was higher. This is might due to e.g. the different postures of the models.

Table 30: Visible man SAR values compared to the SAR values of Norman (Norman = 100 %) at different antenna-phantom distances.

	P_{loss} [% Norman]		$SAR_{10\text{g}}$ [% Norman]	
Distance	3 mm	1 mm	3 mm	1 mm
15 cm	104.7	93.5	105.7	116.5
30 cm	107.2	100.5	98.3	108.8
45 cm	91.5	102.9	91.2	101.8
70 cm	103.5	113.6	88.8	98.3
Farfield	98.4	104.0	93.3	97.5

Figure 51 shows the estimated compliance distances based on the ICNIRP limits for the general public exposure. In this case, all the estimated compliance distances

D satisfy

$$D \leq 0.1 \frac{\mathrm{m}}{\mathrm{W}} (P_{\mathrm{rad}} + 1 \ \mathrm{W}).$$

However, the amount of available results is very limited, so this formula is only suggestive.

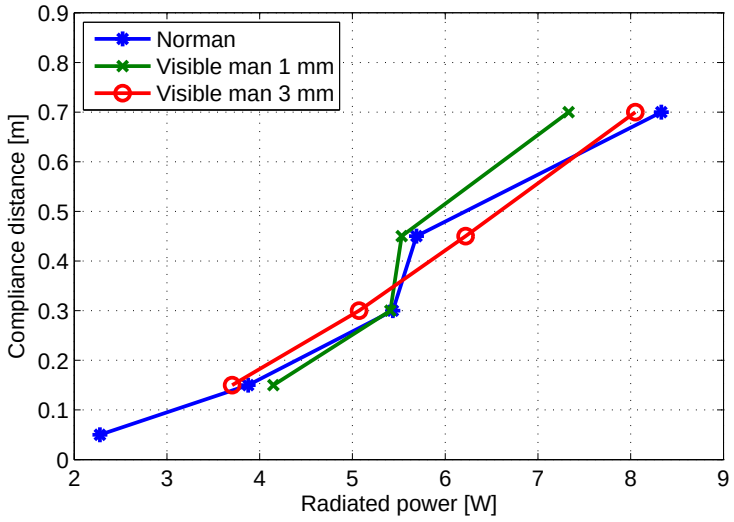

Figure 51: Estimate for the compliance distance as a function of antenna radiated power.

7 Discussion

7.1 Calculation errors

Based on the presented results, some sources of calculation error, which affect the accuracy of the resulting SAR values, can be itemized:

Discretization error: When the resolution satisfied $\Delta < \lambda/10$, the SAR results usually seemed to be correct at a qualitative level. The accuracy could be heavily affected by the material cell type (E/H), especially in the case of small spheres or heterogeneous human phantoms. The accuracy was naturally improved when the resolution was increased.

Absorbing boundary conditions: The error due to the approximation of free space by absorbing boundary conditions was shown to be negligible.

Floating-point accuracy: In all the results, single-precision (4 byte) floating-point arithmetic is used. Using double-precision (8 byte) numbers had extremely small effect on the results. This was studied by exposing a small muscle sphere to a plane wave, as was done in Section 6.2, using both single- and double-precision floating-point numbers. The difference in both whole-body and the peak local SAR was of the order thousandth of percent, and is thus truly negligible.

Staircase approximation: For large enough objects (in cells), the approximation of curved boundaries by a staircase model can be assumed small. The results suggest that the error in SAR values in a sphere is less than 1 % if the sphere radius is greater than 14 cells.

Anatomical accuracy: The accuracy of the anatomical modeling can be thought to have some effects on the SAR values. While there are still too few results to reliably distinguish this error from the other sources of error (especially the discretization error), it seems that, for reasonably fine mesh resolutions, this error is considerably smaller than the discretization error.

Local power loss density calculation method: When the resolution satisfied $\Delta < \lambda/10$, the difference between the two calculation methods could be up to 5 %. Increasing the resolution naturally reduced the difference.

Antenna circuit model: This may have an effect on the SAR results. In this work, the circuit model was approximated by discrete sources with inner resistances. Based on the results in Section 6.4.4, it seems that the magnitude of the error in SAR values due to the approximation of the antenna circuit model might be up to several percents.

Many of the most significant sources of error become smaller as the resolution is increased. Doubling the resolution increases the memory requirements eight-fold, and also halves the maximum stable time step. Thus in practice, the resolution cannot be increased very much, and we have to make do with some error.

7.2 Other uncertainties

In addition to the calculation errors, there are several other factors which cause uncertainty in the results. These include e.g. the choice of the human body model and the uncertainties in the material parameters.

There can be significant differences in the base station SAR results of two different body models — in the results presented in Section 6.5.2, the difference between the peak spatial-averaged SAR of Norman and Visible man phantoms was up to 20 %. Similar distinction was also found in the total power losses of the two models, producing possibly an even larger difference in the whole-body-averaged SAR values. Large differences in SAR values between different body models have also been reported in [31], where there were up to 40 % differences in the peak spatial-averaged SAR of Visible man and Zubal.

Using child models or changing the posture and the position of the body model will likely cause additional differences. Child models are special compared to the adult models, because, even near an antenna, whole-body-averaged SAR might be more restrictive than the localized SAR — in the adult models, the localized SAR was considerably more restrictive than the whole-body SAR. Naturally, the uncertainty in SAR values due to the choice of the body model should be taken into account when estimating the compliance distance of an antenna by introducing a sufficient safety margin, as it is important that the basic restriction limits are not exceeded for any individual or any posture.

One source of uncertainty is the choice of the material parameters. The effects of material parameters on the SAR values have been discussed in e.g. [32], [8] and [33]. It was shown in [33] that SAR values in a head may either decrease or increase when the permittivity and conductivity values are increased. The actual anatomy of the head model was concluded to play a key role in the SAR variation when the dielectric values are increased.

It is shown in [34] that radio-frequency permittivity and conductivity values in rat tissues decrease with age. The decrease in dielectric values from 30 to 70 days old rat could be as large as 10–40 % depending on the tissue. If similar results hold for humans, the choice of the material parameters is particularly important if SAR is studied in child or infant models.

Naturally, the differences in tissue densities cause equally large differences in the evaluated SAR values. For example, the material densities used in [35] are slightly different compared to the densities used in this work (Table 2).

The antenna type and model naturally have a large impact on the SAR results. The exposure analysis is always specific to the antenna used. Some effects of antenna models can be found in e.g. [36] and [35].

The spatial-averaging algorithm of SAR might also have some effects. In this work, the averaging method of [21], which used cubical averaging volumes, was used. Taking the maximum of the localized SAR averaged over "any 10 g of contiguous tissue", as in [22], would produce larger values. Also, mass- or volume-averaging methods for the SAR usually give slightly different results.

8 Conclusions

The FDTD method was applied to human-BSA exposure problems. This required knowledge about the method itself, modeling materials, human body models, absorbing boundary conditions, modeling antennas, and SAR calculation methods. A large number of numerical results was presented to illustrate the sources of error and uncertainties in FDTD SAR calculations.

Here is a summary of the conclusions that could be drawn based on the numerical results:

- The error due to the approximation of free space by properly implemented CPML absorbing boundary conditions is negligible. The SAR calculations in human body models seem to be quite "robust", so that even nonperfect ABC's may perform sufficiently well.
- Material cell type (E/H) may have significant effects on the SAR values especially in small spheres and heterogeneous human models. The effects of the material cell type in small spheres have a clear connection with the spherical TE^r and TM^r resonances.
- The error due to the staircase approximation is small for spheres with radii larger than 14 cells.
- Insufficient resolution or faulty absorbing boundary conditions may cause both over- or underestimation for the SAR.
- The $\lambda/10$ rule of thumb for the mesh resolution appears to hold well in the sense that the resolutions coarser than this usually failed to give good results.
- Local power loss density calculation methods may have a noticeable effect on the SAR values.
- Radiated power from an antenna can be reliably calculated from the currents and voltages over the discrete sources.
- The choice of the inner resistances of the discrete sources may have an effect on the SAR values.
- The choice of the body model and its posture may have a significant effect on the sensitivity of the localized SAR values with the resolution.
- Far from the antenna, where the plane-wave approximation can be used, the basic restriction limits for the whole-body-averaged SAR are more restrictive than the limits for the localized SAR. However, it is unlikely that the SAR limits would be exceeded in the far field.
- Near (≤ 0.7 m) the studied four-element base station antenna, the basic restriction limits for the local spatial-averaged SAR were considerably more restrictive than the limits for the whole-body-averaged SAR.

- Whole-body-averaged SAR is heavily affected by the total mass of the body. E.g. the mass of the Visible man phantom was 44 % higher than the mass of the Norman phantom. Consequently, the whole-body SAR values of Visible man were always significantly lower than those of Norman.

References

[1] A. Taflove and S. C. Hagness, *Computational Electrodynamics: The Finite-Difference Time-Domain Method*. Artech House, 3rd ed., 2005.

[2] K. S. Yee, "Numerical solution of initial boundary value problems involving Maxwell's equations in isotropic media," *IEEE Transactions on Antennas and Propagation*, vol. 14, pp. 302–307, 1966.

[3] P. Monk and E. Süli, "Error estimates for Yee's method on non-uniform grids," *IEEE Transactions on Magnetics*, vol. 30, pp. 3200–3203, 1994.

[4] C. Gabriel, S. Gabriel, and E. Corthout, "The dielectric properties of biological tissues: I. Literature survey," *Physics in Medicine and Biology*, vol. 41, pp. 2231–2249, 1996.

[5] S. Gabriel, R. Lau, and C. Gabriel, "The dielectric properties of biological tissues: II. Measurement in the frequency range 10 Hz to 20 GHz," *Physics in Medicine and Biology*, vol. 41, pp. 2251–2269, 1996.

[6] S. Gabriel, R. Lau, and C. Gabriel, "The dielectric properties of biological tissues: III. Parametric models for the dielectric spectrum of tissues," *Physics in Medicine and Biology*, vol. 41, pp. 2271–2293, 1996.

[7] IFAC-CNR, "An Internet resource for the calculation of the dielectric properties of body tissues in the frequency range 10 Hz – 100 GHz." Internet resource. http://niremf.ifac.cnr.it/tissprop/.

[8] P. A. Mason, W. D. Hurt, T. J. Walters, J. A. D'Andrea, P. Gajsek, K. L. Ryan, D. A. Nelson, K. I. Smith, and J. M. Ziriax, "Effects of frequency, permittivity, and voxel size on predicted specific absorption rate values in biological tissue during electromagnetic-field exposure," *IEEE Transactions on Microwave Theory and Techniques*, vol. 48, pp. 2050–2058, 2000.

[9] National Library of Medicine, Bethesda, MD, "Visible human project." Online. http://www.nlm.nih.gov/research/visible/index.html.

[10] P. J. Dimbylow, "FDTD calculations of the whole-body averaged SAR in an anatomically realistic voxel model of the human body from 1 MHz to 1 GHz," *Physics in Medicine and Biology*, vol. 42, pp. 479–490, 1997.

[11] I. Zubal, C. Harrell, E. Smith, Z. Rattner, G. Gindi, and P. Hoffer, "Computerized three-dimensional segmented human anatomy," *Medical Physics*, vol. 21(2), pp. 299–302, 1994.

[12] ICRP, "Basic anatomical and physiological data for use in radiological protection: reference values," *ICRP Publication 89*, 2002.

[13] J.-P. Bérenger, "A perfectly matched layer for the absorption of electromagnetic waves," *Journal of Computational Physics*, vol. 114, pp. 185–200, 1994.

[14] Z. S. Sacks, D. M. Kingsland, R. Lee, and J.-F. Lee, "A perfectly matched anisotropic absorber for use as an absorbing boundary condition," *IEEE Transactions on Antennas and Propagation*, vol. 43, pp. 1460–1463, 1995.

[15] J. A. Roden and S. D. Gedney, "Convolutional PML (CPML): An efficient FDTD implementation of the CFS-PML for arbitrary media," *Microwave and Optical Technology Letters*, vol. 27, pp. 334–339, 2000.

[16] W. C. Chew and W. H. Weedon, "A 3-D perfectly matched medium from modified Maxwells equation with stretched coordinates," *Microwave and Optical Technology Letters*, vol. 7, pp. 599–604, 1994.

[17] J.-P. Bérenger, "Evanescent waves in PML's: Origin of the numerical reflection in wave-structure interaction problems," *IEEE Transactions on Antennas and Propagation*, vol. 47, pp. 1497–1503, 1999.

[18] R. J. Luebbers and F. Hunsberger, "FDTD for Nth-order dispersive media," *IEEE Transactions on Antennas and Propagation*, vol. 40, pp. 1297–1301, 1992.

[19] J.-P. Bérenger, "Numerical reflection from FDTD-PMLs: A comparison of the split PML with the unsplit and CFS PMLs," *IEEE Transactions on Antennas and Propagation*, vol. 50, pp. 258–265, 2002.

[20] IEEE International Committee on Electromagnetic Safety, "IEEE standard for safety levels with respect to human exposure to radio frequency electromagnetic fields, 3 kHz to 300 GHz," *IEEE Std C95.1, 1999 Edition.*

[21] IEEE International Committee on Electromagnetic Safety, "IEEE recommended practice for measurements and computations of radio frequency electromagnetic fields with respect to human exposure to such fields, 100 kHz–300 GHz," *IEEE Std C95.3-2002.*

[22] ICNIRP (International Commission on Non-Ionizing Radiation Protection), "Guidelines for limiting exposure to time-varying electric, magnetic and electromagnetic fields (up to 300GHz)," *Health Physics*, vol. 74, pp. 492–522, 1998.

[23] The Council of the European Union, "Council recommendation of 12 July 1999 on the limitation of exposure of the general public to electromagnetic fields (0 Hz to 300 GHz)," 1999.

[24] G. Bit-Babik, A. Faraone, C.-K. Chou, M. Swicord, and V. Anderson, "Spatially averaged SAR relationship to thermal response due to RF energy deposition in lossy heterogeneous medium," Presentation at BEMS 2006.

[25] K. Caputa, M. Okoniewski, and M. A. Stuchly, "An algorithm for computations of the power deposition in human tissue," *IEEE Antennas and Propagation Magazine*, vol. 41, pp. 102–107, 1999.

[26] J. Wang, O. Fujiwara, S. Kodera, and S. Watanabe, "FDTD calculation of whole-body average SAR in adult and child models for frequencies from 30 MHz to 3 GHz," *Physics in Medicine and Biology*, vol. 51, pp. 4119–4127, 2006.

[27] R. P. Findlay and P. J. Dimbylow, "Variations in calculated SAR with distance to the perfectly matched layer boundary for a human voxel model," *Physics in Medicine and Biology*, vol. 51, pp. N411–N415, 2006.

[28] I. Lindell and K. Nikoskinen, *Sähkömagnetiikka*. 2003. (Lecture notes, in Finnish).

[29] P. J. Dimbylow, "Fine resolution calculations of SAR in the human body for frequencies up to 3 GHz," *Physics in Medicine and Biology*, vol. 47, pp. 2835–2846, 2002.

[30] S. Ilvonen, K. Kärkkäinen, T. Uusitupa, I. Laakso, and K. Nikoskinen, "Studying the accuracy of FDTD analysis for human exposure evaluations in the vicinity of a base station antenna," Presentation in Progress In Electromagnetics Research Symposium 2007, Beijing, China.

[31] L. Catarinucci, P. Palazzari, and L. Tarricone, "On the use of numerical phantoms in the study of the human-antenna interaction problem," *IEEE Antennas and Wireless Propagation Letters*, vol. 2, pp. 43–45, 2003.

[32] W. D. Hurt, J. M. Ziriax, and P. A. Mason, "Variability in EMF permittivity values: Implications for SAR calculations," *IEEE Transactions on Biomedical Engineering*, vol. 47, pp. 396–401, 2000.

[33] J. Keshvari, R. Keshvari, and S. Lang, "The effect of increase in dielectric values on specific absorption rate (SAR) in eye and head tissues following 900, 1800 and 2450 MHz radio frequency (RF) exposure," *Physics in Medicine and Biology*, vol. 51, pp. 1463–1477, 2006.

[34] A. Peyman, A. A. Rezazadeh, and C. Gabriel, "Changes in the dielectric properties of rat tissue as a function of age at microwave frequencies," *Physics in Medicine and Biology*, vol. 46, pp. 1617–1629, 2001.

[35] M. Martínez-Búrdalo, A. Martín, M. Anguiano, and R. Villar, "On the safety assessment of human exposure in the proximity of cellular communications base-station antennas at 900, 1800 and 2170 MHz," *Physics in Medicine and Biology*, vol. 50, pp. 4125–4137, 2005.

[36] E. Nordström, "Calculation of specific absorption rate (SAR) for typical WCDMA base station antennas at 2140 MHz," Master's thesis, Department of Physics and Measurement Technology, Biology and Chemistry, Linköping Institute of Technology, 2004.